The Impact of Internal Solitary Waves on the Nutrient Circulation System

by

Jason Olsthoorn

A thesis
presented to the University of Waterloo
in fulfillment of the
thesis requirement for the degree of
Master of Mathematics
in
Applied Mathematics

Waterloo, Ontario, Canada, 2013

Abstract

Internal waves in lakes and oceans are ubiquitous whenever a density stratification is present. These waves are relatively slow moving (compared to surface water waves), can be large in extent and have long time scales. As these waves are so common, it is known that they play a role in recirculating nutrients throughout the water column. The various factors contributing to this recirculation are commonly referred to as the nutrient circulation system. This thesis analyses three potential mechanisms of internal wave influence on the nutrient circulation system.

Surface water waves have been well known to influence the nutrient circulation system, especially in shallow regions where wave breaking occurs. However, internal water waves can affect the flow of lake nutrients in deeper water where surface waves will have a negligible effect. In this thesis, we use pseudospectral methods to analyze internal wave induced fluid flow within the water column of a lake or ocean, within the bottom boundary layer and within the sub-fluid porous layer. These three regimes represent significantly differing length scales within lake and ocean systems. In all cases presented, we assume that the water column is deep enough that we can neglect the effect of surface water waves.

Previous literature indicates that internal waves of sufficient size can induce the formation and bursting of separation bubbles near the bottom boundary layer. These bursting events have the potential to induce significant resuspension of sediment back into the water column. We explicitly model shear induced resuspension and demonstrate that only internal waves of sufficient magnitude can induce true resuspension. We present a parameterization of the non-dimensional parameter regime required for resuspension.

These bursting events are always associated with vortex production near the bottom boundary. Near the lake bottom, a layer of fluid mud is present which is known to be non-Newtonian in nature. The non-Newtonian properties of the fluid preserve the small scale features of the flow and locally change the Reynolds number and thereby facilitate more energetic flows on shorter length scales. We thus demonstrate that the vortices found within the fluid mud region have the potential to induce substantial subsequent resuspension. It is shown that the non-Newtonian effects are even substantive enough to overcome an increase in viscosity near the bottom layer.

Beneath the free flowing fluid in lakes and oceans, there often exists a porous layer composed of settled particulate matter. Darcy's law is an empirically determined relationship between the seepage rates found within such a porous layer and the pressure. Due to their large amplitude, internal waves can have produce a significant pressure signature on the bottom of the water column. We demonstrate that internal waves can induce significant seepage through the bottom porous layer. Bursting events near the lake bottom can further enhance the seepage rates, by changing the permeability of the porous medium.

We present three separate mechanisms by which internal waves influence the nutrient circulation system over a range of length scales. We believe that this demonstrates the significant effect that internal waves can have on distributing nutrients throughout the water column. Indeed, by these mechanisms internal waves have the potential to be the dominant source of nutrient circulation in certain regions of lakes and oceans.

Acknowledgements

I would like to thank the entire Environmental and Geophysical Fluid Group for all of their help with this thesis. In particular, I would like to thank Dr. Marek Stastna for his patience and humour.

Dedication

This thesis is dedicated to the Embassy for being there when I needed it.

Table of Contents

List of Tables

List of Figures

Chapter 1

Introduction

Internal waves are observed in lakes and oceans whenever a stratification is present [49, 41]. In lakes, these internal waves are often generated via the break down of lake-scale seiches. Internal waves can also be generated via topographic effects [10, 64]. There exists a massive amount of literature on the study of internal waves and their generation. These waves are typically large in both extent and amplitude, have a long timescale and can induce large fluid velocities [63]. This is in contrast to surface water waves which are relatively small, have short time-scales, and only generate velocities near the surface.

As internal waves are so ubiquitous, one would suspect that they might play a significant role in the nutrient circulation system. That is, they may help redistribute nutrients found within the water column. In fact, significant research has recently been done on this subject [52, 88]. Previous literature suggests that internal solitary waves can induce significant lake bed resuspension [97]. Hosegood and Van Haren [53] have shown that internal waves may even be the dominant resuspension mechanism in the ocean. We continue this work and present novel mechanisms by which internal waves may have significant impact on lake and ocean dynamics.

The work presented here details a systematic approach to the various ways by which internal solitary waves can affect the nutrient circulation system. We approach this problem from a reductionist point of view, and reduce the problem down into three distinct modules:

- The impact of internal waves on shear induced resuspension
- The impact of internal wave induced boundary layer instabilities in non-Newtonian muddy lake bottoms

- The impact of internal solitary waves seepage rates within the sediment on the lake bottom.

These three distinct problems are presented separately in chapters 4, 5, 6. Each chapter is self-contained with its own introduction, methodology and results. I have done this intentionally as the chapters focus on their own individual topics. However, the global theme is present throughout and we discuss the amalgamation of these topics in the conclusion.

Lake and ocean bottoms are not usually impermeable layers. They are typically composed of porous layers of detritus and settled bio-matter. If it is compact enough, it will form a solid porous matrix, above which a less dense fluid mud layer will form. For this present thesis we will look at a simplified layered model to look at three separate domains of interest. These three domains roughly correlate to the above defined chapter topics. We assume that the ocean or lake fluid overlays a solid porous matrix between which lies a non-Newtonian fluid mud layer. Figure 1 plots the simple model setup.

The remainder of this thesis is organized as follows. We present some basic mathematical and numerical techniques used throughout this thesis. We look at how internal solitary wave bottom shear can directly induce pickup. We then discuss how a non-Newtonian mud layer can affect the nutrient pickup rates within the water column. We then discuss the impact that internal waves have on lake bottom seepage rates. Finally, we conclude and provide direction for future research.

Note: Throughout the remainder of this thesis I will use the Einstein summation convention where possible to write out any vector equations. However, there are times when using vector notation is more convenient (i.e. $\mathbf{a}$ to denote vector a, as opposed to a_i.) I will use the two notations interchangeably.

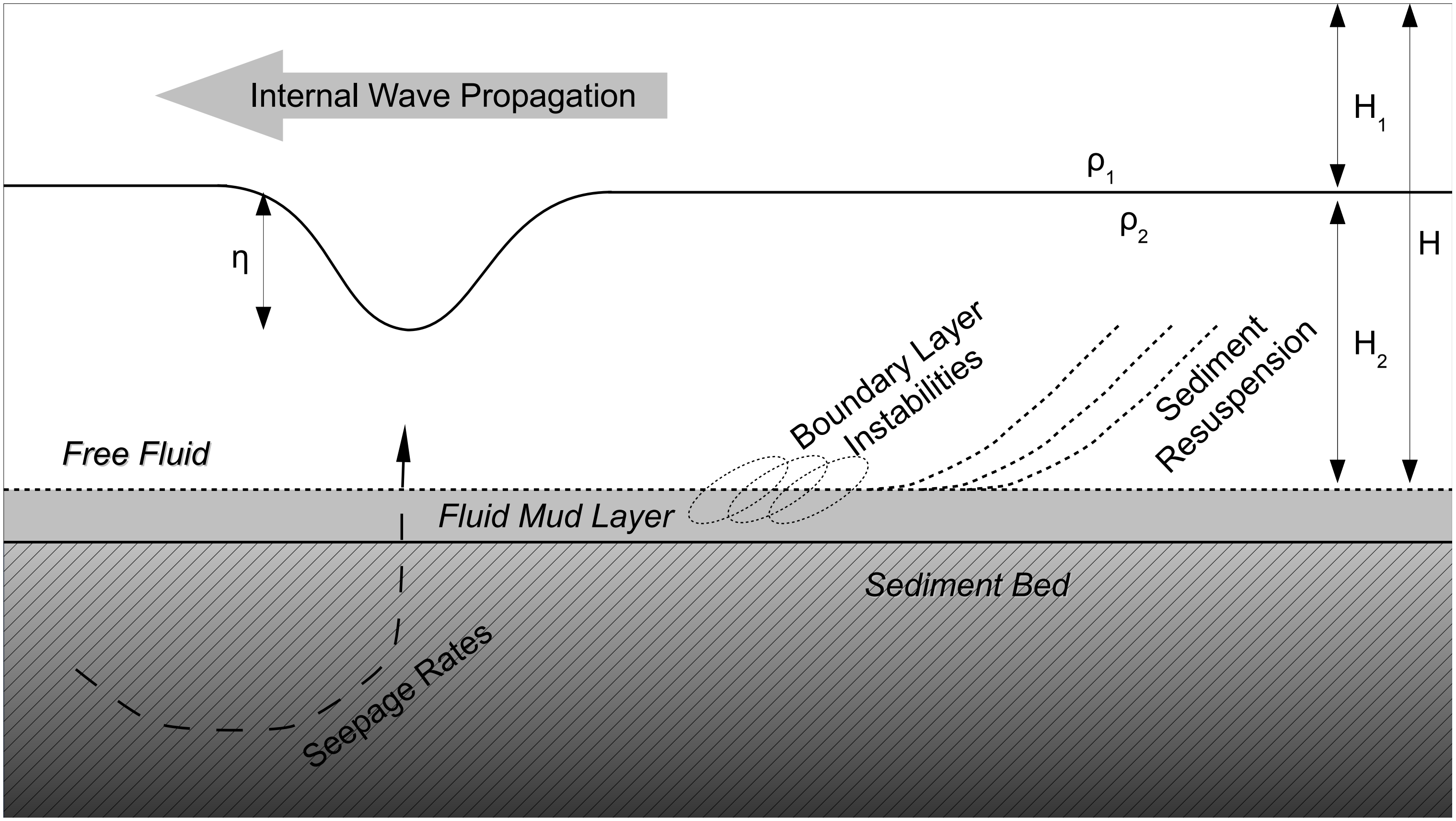

Figure 1.1: Diagram of the basic model layout. The internal wave will induce greater seepage through the bottom porous layer, will induce instabilities in the fluid mud layer and induce sediment resuspension back into the water column.

Chapter 2

Mathematical and Numerical Methods

2.1 Spectral Methods

The problems discussed within this thesis are colloquially described as process studies. What we mean by this that these problems are presented from a reductionist point of view which aims at uncovering the basic characteristic features of a specific process. The hope is that a more complete model would discover these same features compounded. Essentially, we are reducing the problem so as to distinguish the signal from the noise.

This reduction allows us to construct domains that, while not exact duplications of reality, are representative of reality. Similarly, all of the domains presented here are periodic in at least one dimension. This assumption affords us the ability to use Fourier-based methods which are efficient and spectrally accurate. While classical methods (i.e. finite differences) can be shown to have an error which decreases on a polynomial scale with the number of grid points(N) (error $\sim$ O($\frac{1}{N^p}$) for some integer p), spectral methods have an error which decreases exponentially (error $\sim$ O(e^{-cN}) for some constant c). As such, these methods are computationally preferable. Two examples of pseudospectral methods are Fourier Transform methods and Chebyshev Differentiation methods.

Note that spectral methods consider problems in spectral space, generally using a Galerkin scheme, while pseudospectral methods consider problems in physical space, generally using a collocation approach. For the purposes of this thesis, the two terms will be used interchangeably.

2.2 Fourier Series

The Fourier series has been used ubiquitously in applied mathematics and is essential to the understanding of many physical problems. Its usefulness comes from the fact that hard problems in "physical space" can turn out to be simple in "Fourier space." Transforming between Fourier space and physical space is the essential feature of Fourier-based methods.

Before we begin, I would like to mention that the majority of the information here and in the next section can be found in Trefethen's book [103] on spectral methods. For a more complete description, please see that text.

Consider a L_2-integrable function f(x), which is defined on the entire real line. Its Fourier transform is defined as

$$\hat{f}(k) = \int_{-\infty}^{\infty} f(x) \exp\left[ikx\right] dx, \;\; k \in \mathbb{R}$$

where $(\hat{\cdot})$ denotes a variable in Fourier space. We can define the inverse transform as

$$f(x) = \frac{1}{2\pi} \int_{-\infty}^{\infty} \hat{f}(k) \exp\left[-ikx\right] dk, \;\; x \in \mathbb{R}.$$

Thus, we see that we can easily transform a function from physical space to Fourier space and back again.

In practice, a numerical scheme will not have f(x) defined on the entire real line, but instead we will have some evenly spaced finite grid $(x_i \ , i \in [1, N])$ on which we are trying to find an approximate solution for $u_i = f(x_i)$. For the purposes of this discussion, we will, without loss of generality, restrict $x \in [0, 2\pi]$. If this is the case, we are restricted to a bounded and discrete Fourier space (see [103]) which provides a Fourier series of integer wavenumbers, $k \in [-\frac{N}{2} + 1, \frac{N}{2}]$. That is:

$$\hat{u}_k = \frac{2\pi}{N} \sum_{i=1}^{N} u_i \exp\left[ikx_i\right] \qquad u_i = \frac{1}{2\pi} \sum_{k=-\frac{N}{2}+1}^{\frac{N}{2}} \hat{u}_k \exp\left[-ikx_i\right].$$

In order to approximate the derivative of f(x) on the grid (x_i), we would need to define a band-limited interpolant v(x) for which we have $v(x_i) = u_i$. It turns out that, in this case, the interpolant function for v(x) is a sum of periodic sinc functions. In practice, a faster method is used, and hence we refer the reader to [103] for the theoretical details.

In practice, we are able to use the fast Fourier transform (FFT) to compute the derivatives. The basic procedure to computing the approximate derivative of $u_i = f(x_i)$ is as follows:

- Find the discrete Fourier transform of u_i, $\hat{u}_k$
- Define $\hat{w}_k = ik\hat{u}_k$, with wavenumbers k
- Find the inverse transform of $\hat{w}_k$, w_i

Here, w_i is an approximation to $f'(x_i)$.

2.2.1 Efficiency and Accuracy

In order to emphasize the usefulness of spectral methods, we quickly write down two theorems which we present without proof.

Theorem 2.2.1 ***Accuracy*** *Let $u \in L^2(\mathbb{R})$ with grid function w on $\Delta x\mathbb{Z}$ defined $w_j = u(x_j)$. If u has infinitely many continuous derivatives in $L^2(\mathbb{R})$, then for some wavenumber $k \in [-\pi/\Delta x, \pi/\Delta x]$*

$$|\hat{w}(k) - \hat{u}(k)| = O(\Delta x^p), \ \textit{as } \Delta x \to 0.$$

for every integer p.

taken from [103].

Theorem 2.2.2 ***Efficiency*** *If N is product of many small primes, the Fast Fourier Transform (FFT) of a vector with length N can be computed in $O(N \ln N)$ operations.*

2.3 Chebyshev Differentiation

While Fourier methods are ideal for periodic domains, there are many simple problems where a finite domain is preferable (especially in situations in which boundary conditions are vital to capture the relevant physics). In such cases, we can use Chebyshev differentiation matrices to help. We will use polynomials to act as our basis functions. Before we proceed, we must first deal with the particular problem of grid setup.

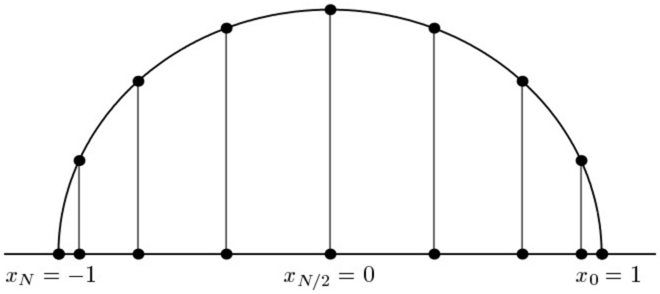

Figure 2.1: Chebyshev grid points as given by projections of of evenly spaced points on the unit circle. Picture taken from [103].

Chebyshev Grid

When using Fourier methods, we used an evenly spaced grid. This works well as Fourier methods use trigonometric functions with a specified wavelength, so it is very natural to use such a grid. However, it turns out that using an evenly spaced grid for polynomial interpolation results in a divergent method as $N \to \infty$.

The solution is rather simple: use a different grid. Such a grid, called a Chebyshev (Cheb) grid, is defined as

$$x_j = \cos\left(j\pi/N\right). \tag{2.1}$$

With reference to Figure 2.1, we see that the grid points are real line projections of evenly spaced points on the complex unit circle.

It turns out that on such a grid, the Chebyshev spectral derivative approximation of an analytic function u has an error which scales by $O(C^{-N})$, where C is some constant greater than one [103].

Differentiation Matrix

The basic idea of Chebyshev spectral methods is to approximate the derivative of a function u_j = f(x_j) by using a polynomial interpolant function on the Cheb grid. Let us call the interpolant function g(x). We can then differentiate the interpolant function and sample to approximate the derivative on the discrete grid as $w_j = \mathrm{g}'(x_j)$. Here, w_j is the approximation to the derivative of our function f(x) sampled on the Cheb grid. Recall that this methodology is very similar to that used in the Fourier case. The difference is that instead of using periodic sinc functions as our basis functions, we are using a polynomial basis (Chebyshev polynomials).

In practice, the differentiation can be carried out as a matrix multiplication acting on the vector of values at the grid points. The matrix used for this purpose is called the differentiation matrix. While Trefethen [103] writes out the complete form of the differentiation matrix, for brevity, I will not write out the complete matrix here. For the remainder of this thesis, whenever I refer to as Cheb differentiation matrix, I will simply refer to it as D.

Boundary Conditions

The most obvious advantage to using a Cheb differentiation matrix over FFT based method is that we can impose boundary conditions. In order to do this, we slightly modify our differentiation matrix D in order to impose the correct conditions.

Let us suppose that we want to solve the following simple equation

$$\frac{d^2}{dx^2} f = \exp[x], \tag{2.2}$$

$$f(1) = a, \tag{2.3}$$

$$f(-1) = b. \tag{2.4}$$

We will to solve this problem on a Cheb grid (x_i) of size N, such that x_N =-1, $x_0 = 1$. The goal is to find an approximate solution to this problem $u_i = f(x_i)$ and we will sample the forcing function as $p_i = \exp[x_i]$. We can rewrite this problem without the boundary conditions using our Cheb differentiation matrix D as

$$[D]\left([D]\begin{bmatrix} u_0 \\ u_j \\ u_N \end{bmatrix}\right) = \begin{bmatrix} p_0 \\ p_j \\ p_N \end{bmatrix} \qquad 1 \leq j \leq N. \tag{2.5}$$

$$\tag{2.6}$$

In order to incorporate the boundary conditions into our problem, we modify the first and last rows of the differentiation matrix, and the first and last entry of the right hand side vector. This gives

$$\begin{bmatrix} 1 & \cdots & 0 \\ \vdots & D^2_{N-2,N-2} & \vdots \\ 0 & \cdots & 1 \end{bmatrix} \begin{bmatrix} u_0 \\ u_j \\ u_N \end{bmatrix} = \begin{bmatrix} a \\ w_j \\ b \end{bmatrix} \qquad 1 \leq j \leq N-1 \tag{2.7}$$

and implicitly implies that $u_0 = a,\ u_N = b$. If one takes a second to think about this methodology, they will see that this is the simplest way of imposing the boundary conditions. From here one could use any of a number of matrix solvers to iteratively solve this linear algebra problem which has the standard form $Ax = b$.

Similarly, we find that

$$\begin{bmatrix} D(1,1) & D(1,2:N-1) & D(1,N) \\ D^2(2:N-1,1) & D^2_{N-2,N-2} & D^2(2:N-1,N) \\ D(N,1) & D(N,2:N-1) & D(N,N) \end{bmatrix} \begin{bmatrix} u_0 \\ u_j \\ u_N \end{bmatrix} = \begin{bmatrix} a \\ w_j \\ b \end{bmatrix} \quad 1 \leq j \leq N-1 \tag{2.8}$$

imposes $u'_0 = a,\ u'_N = b$.

2.4 Mixed Methods

Now that we are able to use two different spectral methods, we demonstrate how we can easily use a combination of the two methods to solve multi dimensional problems. We will describe how to use a combination of methods for problems in two dimensions but this can easily be extended to higher dimensions. It should be fairly clear how we can solve a doubly-periodic problem using a Fourier-Fourier method. Similarly, with a little thought, we can solve a two dimensional finite domain problem using a Cheb-Cheb method. However, a Cheb-Cheb method requires the construction of large dense matrices which are computationally expensive to solve. In order to avoid this problem, we will often solve channel flow-type problems which are periodic in one dimension and finite in another. An example of a problem of this type is written

$$\partial_{xx} f + \partial_{zz} f = 0 \tag{2.9}$$

$$f(-1,z) = f(1,z) \qquad f'(-1,z) = f'(1,z) \tag{2.10}$$

$$f(x,-1) = 0 \qquad f(x,1) = 0 \tag{2.11}$$

where $[x,z] \in [-1,1] \times [-1,1]$.

Using a Fourier transform, we can convert the above partial differential equation into a system of second order ordinary differential equations

$$\partial_{zz} \hat{f} - k_i^2 \hat{f} = 0 \tag{2.12}$$

$$\hat{f}(k_i,-1) = 0 \qquad \hat{f}(k_i,1) = 0 \tag{2.13}$$

with k_i, the i^{th} horizontal wavenumber. The solution for each wavenumber can be solved independently using Chebyshev differentiation matrices. The majority of the problems found within this thesis will be solved in such a domain.

Chapter 3

Incompressible Navier-Stokes Equations

The Navier-Stokes equations are the fundamental equations of motion for a fluid with finite viscosity (ν). While I assume in this thesis that the reader has some familiarity with the mathematics of fluid mechanics, I will discuss the essential components of the derivation of the Navier-Stokes equations. We will then discuss the basic simplifying assumptions of incompressibility and the Boussinesq approximation. We follow this with a brief discussion on internal waves and conclude with a discussion on the implications of viscosity and the associated boundary layer theory.

The work presented here can be found in the following referenced: [92, 63, 39].

3.1 Preliminary Notes

We briefly pause to consider a few notes which will aid in our future discussion. We begin by defining the material volume [63].

Definition 3.1.1 ***Material Volume*** *A material volume is a volume element which deforms with the motion of the fluid. All particles initially within a material volume, remain there. Thus there is no flux through the boundary of a material volume. This is in contrast to a fixed volume where fluid will flow in and out of the boundaries of the volume element.*

With this definition, we have:

Theorem 3.1.2 ***Reynolds Transport Theorem*** *Let V(t) be a material fluid volume element with corresponding C^1 velocity field* $\mathbf{u}$*. Given a C^1 function f, we have that*

$$\frac{d}{dt}\int_{V(t)} f dV = \int_{V(t)} \left[(\partial_t f + \mathbf{u}\cdot\nabla f) + (\nabla\cdot\mathbf{u})\, f\right] dV = \int_{V(t)} \left[\frac{Df}{Dt} + (\nabla\cdot\mathbf{u})\, f\right] dV$$

Reynolds transport theorem provides an essential tool for deriving the Navier-Stokes equations. For a proof of the Reynolds transport theorem, see [5]. Here, $\frac{D}{Dt} = \partial_t + \mathbf{u}\cdot\nabla$ is called the material derivative.

Lastly, before we continue, we state one last theorem which expresses the surface force, or the force unique to a continuum, in terms of the stress tensor.

Theorem 3.1.3 ***Cauchy's Theorem*** *Given a material volume with surface area A(t) and outward normal $\hat{n}_j$, any surface force (t_i) acting on A(t) is given*

$$t_i = \tau_{ij} n_j$$

τ_{ij} *is called the stress tensor.*

When angular momentum is conserved, the stress tensor τ_{ij} is symmetric, and hence has six, linearly independent components which completely describe all of the surface forces acting on a material volume. For a proof, see [39].

3.2 Navier-Stokes Equations

Newton's second law dictates that the sum of the forces on an object is equal to the rate of change of momentum. Here we can apply this law to a fluid element with volume V(t) and corresponding surface area A(t). Using Reynolds transport theorem (RTT), we can quickly see how the Navier-Stokes (N-S) equations are derived.

Integrating over a material volume of fluid, the two forces acting on the fluid are body forces which act on the whole fluid volume (gravity) and surface forces which only act on the surface of the volume element. Thus, we can write that

$$\frac{d}{dt}\{\text{Momentum}\} = \{\text{Body Forces}\} + \{\text{Surface Forces}\} \tag{3.1}$$

$$\frac{d}{dt}\int_{V(t)} (\rho u_i)\, dV = \int_{V(t)} (\rho g_i)\, dV + \int_{A(t)} (\tau_{ij} n_j)\, dA \tag{3.2}$$

$$\frac{d}{dt}\int_{V(t)} (\rho u_i)\, dV = \int_{V(t)} (\rho g_i + \nabla_j \tau_{ij})\, dV \qquad \text{(Gauss' Law)} \tag{3.3}$$

$$\int_{V(t)} \left(\frac{D\rho u_i}{Dt} + \rho u_i (\nabla_j u_j)\right) dV = \int_{V(t)} (\rho g_i + \nabla_j \tau_{ij})\, dV \qquad \text{(RTT)} \tag{3.4}$$

$$\frac{D\rho u_i}{Dt} + \rho u_i \partial_j u_j = (\rho g_i + \nabla_j \tau_{ij}) \qquad \text{(Equating Integrands)} \tag{3.5}$$

A similar derivation reveals the continuity equation

$$\frac{D\rho}{Dt} + \rho \nabla \cdot \mathbf{u} = 0$$

For a more detailed look at this work, see [63].

3.2.1 Constitutive Laws

The surfaces forces acting on a material volume of fluid are given via the relation

$$F_i^{\text{Surface}} = \int_{A(t)} t_i dA = \int_{A(t)} \tau_{ij} n_j dA = \int_{V(t)} \partial_j \tau_{ij} dV$$

where τ_{ij} is the stress tensor [92].

The first assumption we will make is that the stress tensor must be symmetric. This has been found to be reasonable for most conventional fluids (air, water, etc.). For historical reasons, the stress tensor is decomposed into an isotropic pressure (P) component and the remaining deviatoric stress tensor (σ)

$$\tau_{ij} = -P\delta_{ij} + \sigma_{ij}$$

Consider a material volume with initial position $x_{i,0}$ and velocity $u_{i,0}$. The material volume is then displaced a short distance away to position x_i. Using a Taylor series, we describe the velocity (u_i) at x_i expanded about $x_{i,0}$. To first order we can write out that

$$u_i - u_{i,0} \approx \nabla_j u_i \left(x_j - x_{j,0}\right).$$

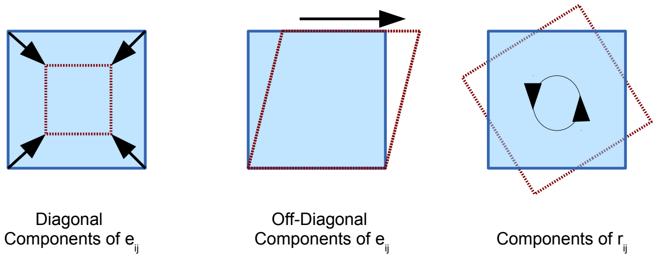

Figure 3.1: The physical meaning of the components of e_{ij} and r_{ij}. Notice that the components of r_{ij} do not cause any deformation to the body.

Thus, we see that the gradient gives us a measuring stick to approximate the change in velocity based upon the change in position. We can write the gradient in term of its symmetric and anti-symmetric components

$$\nabla_j u_i = \frac{1}{2}\left(\nabla_j u_i + \nabla_i u_j\right) + \frac{1}{2}\left(\nabla_j u_i - \nabla_i u_j\right) = e_{ij} + \frac{1}{2} r_{ij}.$$

for the strain rate tensor e_{ij} and the rotation rate tensor r_{ij}. The rotation rate tensor defines the instantaneous rotation of the fluid and the strain rate tensor defines the instantaneous deformation of the material volume. For a more detailed exposition, see [63, 92].

Figure 3.1 plots the physical components of the strain rate tensor e_{ij} and the rotation rate tensor r_{ij}. Notice that the rotation rate tensor does not cause a deformation to the material volume.

We impose one more condition, and that is that the deviatoric stress tensor (σ_{ij}) is proportional to the deformation of the material volume [63]. As such, we assume that σ_{ij} is a linear function of the strain rate tensor. Given that σ_{ij} is symmetric and is linearly dependent on the rate of strain tensor, it turns out that the most general linear tensor equation reads

$$\sigma_{ij} = 2\mu e_{ij} + \lambda e_{kk}\delta_{ij}. \tag{3.6}$$

See [92] for more details.

This equation (3.6) is referred to as the constitutive law for the fluid. Notice that for an incompressible fluid, $e_{kk} = 0$ and the much simpler equation

$$\sigma_{ij} = 2\mu e_{ij} \tag{3.7}$$

results.

A Newtonian fluid is one for which the dynamic viscosity μ is constant. For a non-Newtonian fluid, this condition is relaxed. We consider fluids wherein the dynamic viscosity (μ) is a function of the strain rate tensor (e_{ij}), with the shear determined experimentally to be more important than compression. Specifically, the viscosity is a function of the second invariant of e_{ij} (I_2), defined as

$$I_2 = \sqrt{\sum_i \sum_j 2\left(e_{ij}e_{ij} - (e_{ii})^2\right)}.$$

For a more complete description of constitutive laws, see [92].

3.2.2 Incompressibility Condition and Boussinesq Approximation

In practice we rarely solve the complete N-S equations because we can make clever simplifications to these equations to reduce their complexity. The two conventional approximations to make for lake and ocean flows are incompressibility and the Boussinesq approximation. See Batchelor [8]and Kundu [63] for more information.

Incompressibility

The incompressibility condition allows you to replace the conservation of mass equation with

$$\nabla \cdot \mathbf{u} = 0.$$

There are three criteria which must be met in order for this approximation to be valid. They are:

- The fluid speed (U) is much less than the speed of sound in the fluid (c)

$$U^2 \ll c^2.$$

- The time scale of interest (τ) is long compared to the period of the sound waves

  $$\frac{L^2}{c^2} \ll \tau^2.$$

  Here L is a characteristic length.

- Variations in the acceleration due to gravity (g) are negligible

  $$L \ll \frac{c^2}{g}$$

In this thesis, we are considering internal wave dynamics in water over lake and ocean scales. The speed of sound in water is approximately 343 m s^{-1} [63] which is orders of magnitude faster than the fluid velocities we consider. Similarly, the time scale of interest and length scales both satisfy the above criteria. Hence, we are well within the regime of incompressibility.

Boussinesq Approximation

The Boussinesq approximation can be colloquially said to "neglect the variations in density except in the buoyancy term." Suppose that we have some small variation in density from the constant background value (ρ_0) which can be written as

$$\rho = \rho_0 + \rho' \qquad \rho' \ll \rho_0$$

The above momentum equations (assuming incompressibility) are then given

$$(\rho_0 + \rho') \frac{D\left[u_i\right]}{Dt} = -\nabla_i P - (\rho_0 + \rho')\, g_i + \nabla_j \tau_{ij}.$$

Now, we can redefine pressure to absorb the first order buoyancy term ($P' = P + \rho_0 \phi$) for an appropriate gravitational potential function ϕ. Thus,

$$(\rho_0 + \rho') \frac{D\left[u_i\right]}{Dt} = -\nabla_i P' - \rho' g_i + \nabla_j \tau_{ij}$$

To leading order, we can simplify as

$$\rho_0 \frac{Du_i}{Dt} = -\nabla_i P' - \rho' g_i + \nabla_j \tau_{ij} \tag{3.8}$$

Why do we keep the buoyancy term ($\rho' g_i$)? In reference to the background density (ρ_0), ρ' is small while we know that g is big. Thus, we argue that the term $\rho' g$ is order one. The Boussinesq approximation is valid when $\rho' \ll \rho_0$.

Thus, the incompressible fluid equations under the Boussinesq approximation can be written

$$\frac{Du_i}{Dt} = -\frac{1}{\rho_0}\nabla_i P - \frac{\rho'}{\rho_0} g_i + \frac{1}{\rho_0}\nabla_j \tau_{ij} \tag{3.9}$$

$$\partial_i u_i = 0 \tag{3.10}$$

$$\frac{D\rho'}{Dt} = \kappa \nabla^2 \rho' \tag{3.11}$$

which are the fluid equations solved within this thesis. Equation 3.11 is derived from simplifications to the energy equation which we do not discuss here. See [63] for more information.

3.3 Internal Waves

In this thesis we are evaluating the effect that internal solitary waves have on the nutrient circulation system. Here we briefly describe some of the basic mathematical foundations to studying internal waves.

3.3.1 Continuously Stratified Internal Waves

Consider now an inviscid ($\mu = 0$), incompressible, statically stable, continuously stratified fluid under the Boussinesq approximation. If we write out the perturbation expansion of the density and velocity fields we get that

$$\begin{aligned} \rho &= \rho_0 + \bar{\rho}(z) + \epsilon \rho' + \dots \\ u &= 0 + \epsilon u' + \dots \\ u &= 0 + \epsilon w' + \dots \\ P &= P_0 + \epsilon P' + \dots \end{aligned}$$

The first order solution to such an expansion is hydrostatic balance. Looking at the $O(\epsilon)$ solutions [63] we get that

$$u'_t = -\frac{1}{\rho_0}\partial_x P', \tag{3.12}$$

$$w'_t = -\frac{1}{\rho_0}\partial_z P' - \frac{\rho'}{\rho_0}g, \tag{3.13}$$

$$\partial_t \rho' + w'\partial_z \bar{\rho} = 0, \tag{3.14}$$

$$\partial_x u' + \partial_z w' = 0. \tag{3.15}$$

We can cross differentiate equations 3.12 and 3.13 to give us

$$\partial_t \left(\partial_z u - \partial_x w\right) = -\frac{\partial_x \rho' g}{\rho_0}.$$

Note that this equation tells us that horizontal variations in density induce vorticity (often this is called baroclinic vorticity generation).

The incompressibility condition 3.15 allows us to construct a streamfunction (ψ) such that

$$\partial_z \psi = u \qquad \partial_x \psi = -w.$$

Finally, using equation 3.14, we can conclude that

$$\partial_{tt}\nabla^2\psi = -N^2(z)\partial_{xx}\psi \tag{3.16}$$

$$N^2(z) = \frac{g\partial_z \rho'}{\rho_0}. \tag{3.17}$$

The buoyancy frequency $N^2(z)$ is specified by the stratification of the underlying fluid problem. Assuming that the solution to these equations takes the form of a traveling wave, we have that

$$\psi = \phi(z)\exp\left[i\left(kx - \omega t\right)\right]$$

which reduces the above equation 3.16 to an ODE eigenvalue equation

$$\partial_{zz}\phi + k^2\left(\frac{N^2}{\omega^2} - 1\right)\phi = 0. \tag{3.18}$$

with appropriately defined boundary conditions. Here, we are implicitly assuming that only the real part of the solution has physical significance.

Thus we see that the structure of the internal waves reduces to an eigenfunction of a Sturm-Louisville problem [45]. In fact, no solutions for this equation are known in general with the exception of when the buoyancy frequency is constant (linear stratification) (and for two layer flow). Under such an assumption, we find that the solutions are

$$\phi = A\exp\left[ikz\sqrt{\frac{N^2}{\omega^2} - 1}\right] + B\exp\left[-ikz\sqrt{\frac{N^2}{\omega^2} - 1}\right].$$

Let us now assume that the fluid is constrained inside of a box of height H. The boundary conditions then become $\phi(0) = 0$ and $\phi(H) = 0$. In this case, we can solve to find that

$$\phi = \sin\left(\frac{n\pi}{H}z\right)$$

where

$$\frac{n\pi}{H} = k\sqrt{\frac{N^2}{\omega^2} - 1} \implies \omega = \frac{Nk}{\sqrt{k^2 + \left(\frac{n\pi}{H}\right)^2}}$$

with corresponding group velocity (c_g)

$$c_{\mathrm{g}} = \frac{\partial\omega}{\partial k} = \frac{N\left(\frac{n\pi}{H}\right)^2}{\left[k^2 + \left(\frac{n\pi}{H}\right)^2\right]^{\frac{3}{2}}}.$$

For more information, see [63].

If we include the first order non-linear and dispersive effects we arrive at the Korteweg-de Vries (KdV) equation used to describe the weakly nonlinear evolution of internal solitary waves. See [68] for more details.

$$\psi = B(x)\phi(z) \tag{3.19}$$

$$\partial_{zz}\phi + \frac{N^2(z)}{c^2}\phi = 0 \tag{3.20}$$

$$\partial_t B + c\partial_x B + \alpha B\partial_x B + \beta\partial_{xxx} B = 0 \tag{3.21}$$

For a two layer flow, we can write out the linear long wave speed as

$$c = \left(g\left(\frac{\rho_2 - \rho_1}{\rho_2}\right)\left(\frac{H_1 H_2}{H_1 + H_2}\right)\right)^{\frac{1}{2}}.$$

Here we have that ρ_1, H_1 and ρ_2, H_2 are the densities and heights of the upper and lower layers respectively. This is discussed later within the thesis.

3.3.2 Internal Solitary Wave Vorticity

In this thesis, we consider fluid domains which are vertically stratified, usually with a single pycnocline (region of rapid density change). In such domains, exact theory [49, 95],permits internal wave solutions of permanent form. These solutions will propagate along a pycnocline, preserving their structure. Depending on the location of the pycnocline, internal solitary waves of depression (if the pycnocline is above the mid-depth) or internal solitary waves of elevation (if the pycnocline is below the mid-depth) will form.

Since an internal solitary wave induces horizontal changes in density, it also generates vorticity. In a frame of reference moving with the wave, there exists a circulation region about the center of the internal wave. Figure 3.2 presents a diagram of the flow about an internal solitary wave of depression. Notice that near the bottom, there exists a convergence region near the back of the wave. A similar diagram could be drawn for a internal solitary wave of elevation where the location of the convergence region is in the front of the wave. For reasons explained in section 3.4, boundary layer instabilities and separation are prone to happen in the convergence region generated by the internal wave.

For a more complete description of these boundary layer instabilities, see [97, 2, 32].

3.4 Boundary Layer Theory

The presence of viscosity in the Navier-Stokes equations has a number of interesting mathematical implications which need to be addressed. Namely, the viscosity term $(\nu\nabla^2 u)$

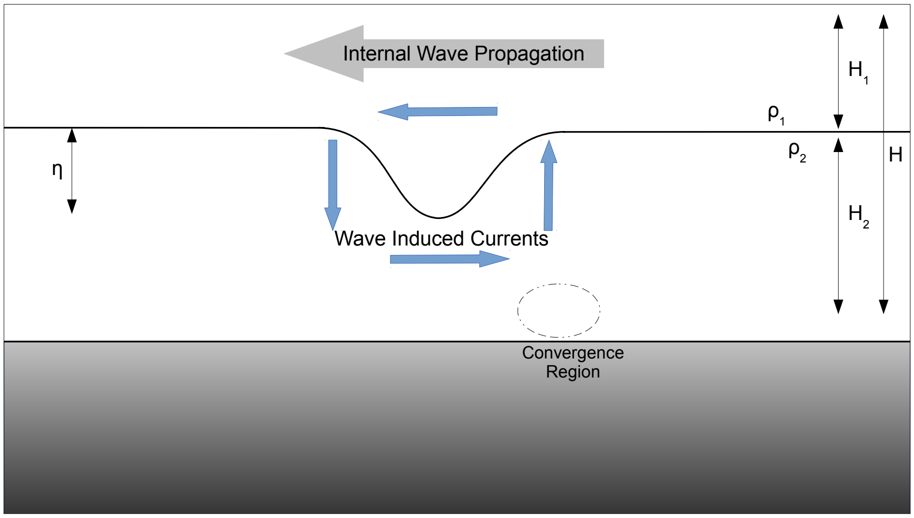

Figure 3.2: Diagram of an internal solitary wave of depression propagating to the left. The convergence region at the back of the internal wave is labeled along with the wave induced circulation.

changes the order to the partial differential equations from first order (i.e. the highest derivative in the equation is order 1) to second order. In the absence of viscosity, it is sufficient to make the no normal flow condition at a solid boundary ($\mathbf{u} \cdot \hat{n} = 0$). However, the presence of viscosity changes the order of the equations and requires us to impose additional conditions, which turn out to be the no-slip conditions at a solid wall [63, 92]. That is, a fluid element at the wall, stays at the wall. Mathematically, we write these conditions (in 2D) as,

$$u\Big|_{z=\text{Wall}} = 0 \qquad w\Big|_{z=\text{Wall}} = 0.$$

The boundary condition at a wall has been changed. In order to see the significance of this, we non dimensionalize the incompressible Navier-Stokes equations with constant density in two dimensions. For this, we write out that

$$P' = \rho_0 U^2 P \qquad u' = Uu \qquad w' = Ww \qquad z' = Hz \qquad x' = Lx \qquad t' = \frac{L}{U}t$$

where primes denote physical quantities. For reasons that will be explained later, assume $\frac{W}{U} \sim \frac{H}{L}$ in this fluid. The Navier-Stokes equations then become

$$\partial_t u + u\partial_x u + w\partial_z u = -\partial_x P + \frac{1}{\mathrm{Re}}\left(\partial_x^2 u + \frac{1}{\delta^2}\partial_z^2 u\right) \tag{3.22}$$

$$\partial_t w + u\partial_x w + w\partial_z w = -\frac{1}{\delta}\partial_z P + \frac{1}{\mathrm{Re}}\left(\partial_x^2 w + \frac{1}{\delta^2}\partial_z^2 w\right) \tag{3.23}$$

$$\partial_x u + \partial_z w = 0 \tag{3.24}$$

where we define the Reynolds number (Re= $\frac{UL}{\nu}$) and the aspect ratio $\delta = \frac{H}{L}$.

It turns out that a typical value of viscosity for water is $\nu = 1 \times 10^{-6}\mathrm{m}^2/\mathrm{s}$. In the middle of a lake where we would expect to find internal waves, let us pick rough characteristic values for the mean current and length scales to be $U = W \sim$1m/s and $H = L \sim$1m. Thus, the reciprocal of the Reynolds number is $\frac{1}{\mathrm{Re}} \sim 10^{-6}$. Clearly the effect of viscosity will be negligible for this domain [63]. Thus, we are justified in dropping the viscous terms and subsequently, justify the KdV theory in these domains.

However, near a horizontal boundary, the vertical scale will be much smaller than the horizontal scale. Here, if $\delta = \frac{H}{L} \sim \frac{1\mathrm{mm}}{1\mathrm{m}} = 10^{-3}$, then we find that $\frac{1}{\mathrm{Re}}\frac{1}{\delta^2} \sim 1$. We can no longer neglect the effect of viscosity near the wall! We see that there exist two very different domains of interest. Away from the wall, the effect of viscosity will be negligible, but near the wall, the effect of viscosity is paramount as the gradients near the wall are large [92].

If $\delta \ll 1$ ($\frac{1}{\delta} \gg 1$), then keeping only the first order terms we find that in the boundary layer, the equations of motion read

$$\partial_t u + u\partial_x u + w\partial_z u = -\partial_x P + \frac{1}{\mathrm{Re}'}\left(\partial_z^2 u\right), \tag{3.25}$$

$$0 = -\partial_z P, \tag{3.26}$$

$$\partial_x u + \partial_z w = 0 \tag{3.27}$$

where $\frac{1}{\mathrm{Re}'} = \frac{1}{\mathrm{Re}}\frac{1}{\delta^2}$. Equation 3.26 indicates that the pressure is essentially uniform through the vertical extent of the boundary layer. This approximation is valid for flow over a boundary with a sufficiently small curvature. Of course these equations need to be augmented with the appropriate boundary conditions:

$$u\Big|_{z=\text{Wall}} = w\Big|_{z=\text{Wall}} = 0 \qquad u\Big|_{z\to\infty} = U_{\text{ext}}$$

where U_{ext} the horizontal flow field found far from the wall, where viscosity is negligible. This indicates why solutions to the Euler equations (for which viscosity is zero) often provide such accurate predictions for flow far from a boundary.

3.4.1 Boundary Layer Separation

Consider a boundary layer over a plate of small curvature with an outer solution flowing from left to the right [63]. The no slip condition on the plate implies that the fluid velocity must increase from the bottom of the boundary layer to the top. Along the wall, the momentum equation 3.25 reads

$$\nu \partial_z^2 u\Big|_{z=\text{Wall}} = \partial_x P.$$

Now, as we approach the outer solution, it will be true that

$$\partial_z^2 u < 0 \quad \text{as } z \to \infty.$$

Bernoulli's equation tells us that along streamlines in a steady inviscid fluid,

$$P = C - \frac{1}{2}\rho u^2 \implies \partial_x P \propto -u\partial_x u.$$

Thus, if we have an accelerating fluid overlying the boundary layer ($\partial_x u > 0$) we will have a 'favourable' pressure gradient across the boundary layer. Here we have that

$$\partial_z^2 u\Big|_{z=\text{Wall}} < 0,$$

and hence the curvature of the horizontal velocity is positive throughout the boundary layer.

Notice now what happens when if the outer flow is decelerating over the boundary layer ($\partial_x u < 0$). This results in what is called an 'adverse' pressure gradient as it implies that

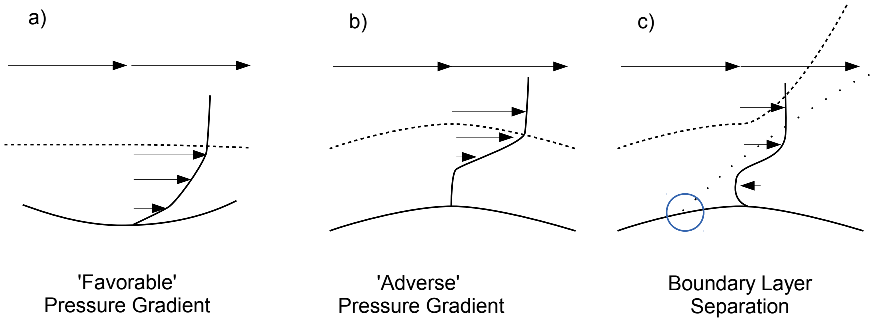

Figure 3.3: Diagram of an adverse pressure gradient inducing boundary layer separation. The separation point is circles on panel c).

$$\partial_z^2 u \bigg|_{z=\text{Wall}} > 0.$$

Thus at some point in the boundary layer there exists an inflection point in the velocity u. This inflection point can result in a separation of the boundary layer from the wall, that is, the outer solution no longer runs parallel to the wall. A separation point is the point where this occurs.

Figure 3.3 plots the boundary layer separation as a result of an adverse pressure gradient. The separation point is circled in panel c) and is identified as the intersection of the forward and reverse flow in the boundary layer, i.e. where

$$\partial_z u \bigg|_{z=\text{Wall}} = 0.$$

It is the focal point of a convergence zone where the boundary layer thickness will grow rapidly. The above boundary layer equations become invalid as the boundary layer is no longer confined to the surface. The rate and location of this separation depends on the geometry of the surface in question. Once boundary layer separation has occurred it is accompanied by vorticity transport into the fluid interior. For more details, see [**?**].

In the context of internal waves, the convergence region in the wake of the wave, possibly in combination with a sloping topography can result in boundary layer separation and resultant vortex generation. Depending on the strength of the internal wave, this instability may, or may not occur. For a more detailed description of this internal wave induced boundary layer instability, see [2, 97].

Chapter 4

Sediment Transport

4.1 Introduction

There has been significant recent interest in internal wave induced boundary layer instability [16, 97, 2, 23, 32, 24]. This work has particular importance to the resuspension of lake and ocean bottom particulate into the water column. While these papers discuss the implication of internal waves to this resuspension mechanism at length, none of them explicitly model the sediment transport. In this chapter, we present an explicit model for this resuspension under an internal wave propagating over topography. After a thorough literature survey, we believe that we are the first to have done so.

In this thesis, we consider internal waves of depression as they are more commonly observed for pynoclines found in the coastal ocean or in lakes due to near surface seasonal temperature variations. The flow induced by these internal waves will generate a convergence region in the wake of the wave. The convergence region can often lead to boundary layer separation and, as a result, sediment resuspension [2]. The effect of topography can amplify this effect. This mechanism has been thoroughly investigated in the literature [32, 16, 2].

Sediment resuspension has important implications for the nutrient circulation system [36]. Surface water waves are a common example of a driving mechanism for resuspension. However, internal waves have the potential to drive significant resuspension in regions where the effect of surface water waves will be negligible. Indeed, Hosegood and Van Haren [53] have suggested, based upon their measurements, that internal waves can be the dominant resuspension mechanism in the continental shelf region of the coastal ocean. We present a model for how internal waves can induce sediment resuspension.

This chapter presents two processes leading to sediment entrainment. The first is true internal wave shear induced resuspension. In this process, stationary sediment particles of the lake bottom are entrained into the main water column. The second process is wherein a boundary layer separation event occurs but the bottom shear is insufficient to induce pickup into the boundary layer. Here, any particulate already found in the boundary layer will be transported into the water column. For the purposes of this thesis, we will denote these processes as resuspension and boundary layer transport respectively. The process of inducing stationary sediment particles into the boundary layer (diffusive sublayer transport) will be denoted as pickup.

The scales found within the boundary layer are small compared to lake or ocean scales. No model we are aware of can resolve these severe differences in scale. As such, we implement a diffusive flux to account for the boundary layer pickup. This is a common approach employed in the literature, for example by [12].

The remainder of this chapter is organized as follows: following the work of Blanchette *et al.* [12], we provide the mathematical framework for modeling the sediment entrainment. Next, we present two simulations of internal waves flowing over a hill topography which exemplify true resuspension and boundary layer transport, respectively. We discuss several cases of internal waves interacting with a sloped lake bottom. We present a criterion for internal solitary wave shear induce sediment resuspension. Finally, we conclude and discuss possible directions for future research.

4.2 Model Equations

The fluid will evolve according to the incompressible Navier-Stokes equations under the Boussinesq approximation which can be written in non-dimensional form

$$\frac{D\mathbf{u}}{Dt} = -\nabla P - \mathrm{Ri}\rho\hat{k} + \frac{1}{\mathrm{Re}}\nabla^2\mathbf{u} \tag{4.1}$$

$$\nabla\cdot\mathbf{u} = 0 \tag{4.2}$$

$$\frac{D\rho}{Dt} = \frac{1}{\mathrm{Pe}_\rho}\nabla^2\rho \tag{4.3}$$

for non-dimensional fluid velocity (u), density (ρ) and pressure P. $\frac{D}{Dt} = \partial_t + \mathbf{u}\cdot\nabla$. The non-dimensional time(T), Richardson number (Ri), the Reynolds number (Re) and the Peclet number (Pe) can be written as:

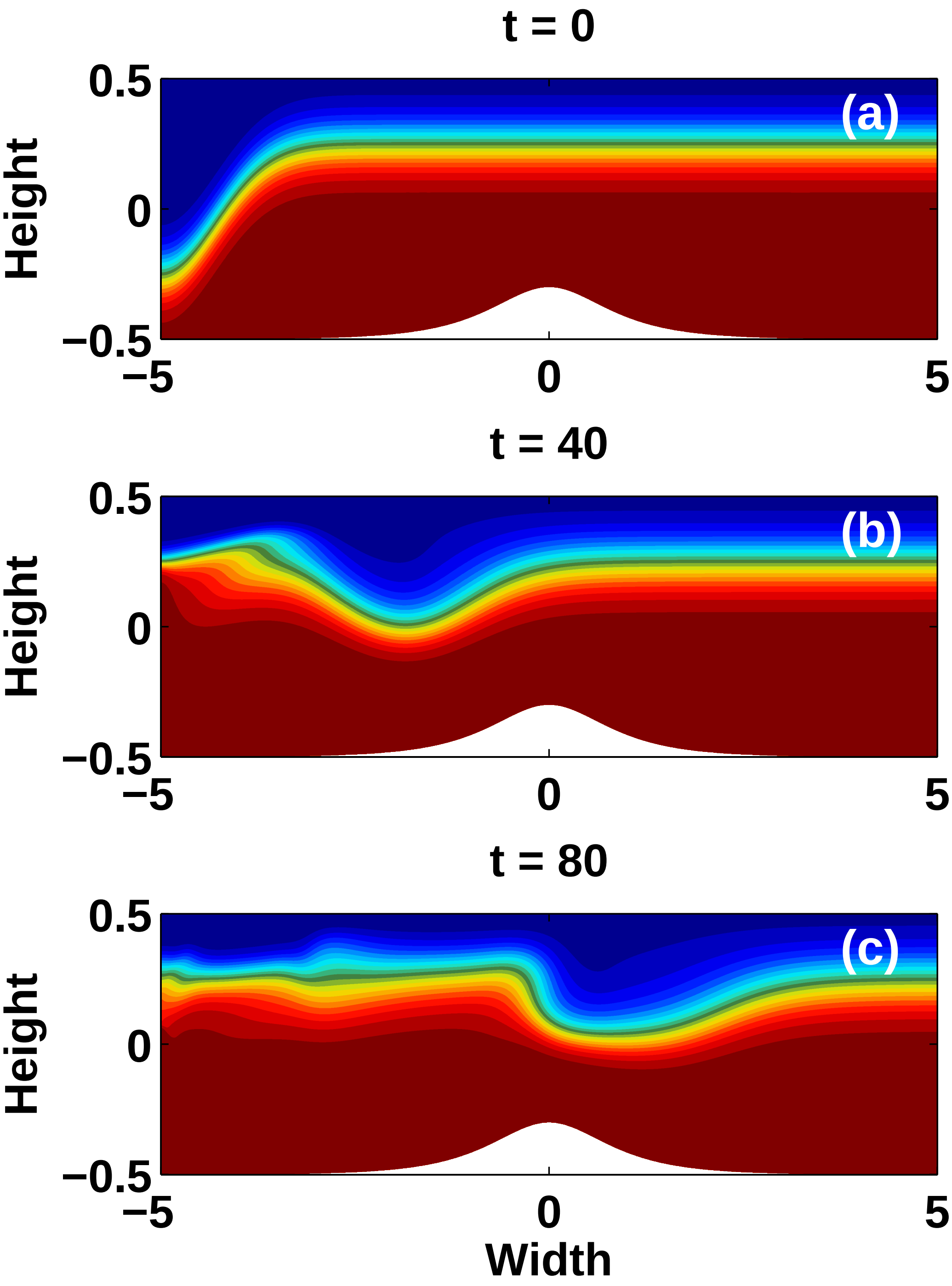

Figure 4.1: Plot of the evolution of the internal solitary wave over time. The density field has been plotted at t = $\{0, 40, 80\}$.

$$T = \frac{tLz}{c_0} \qquad \mathrm{Ri} = \frac{gLz}{c_0^2} \qquad \mathrm{Re} = \frac{c_0 L}{\nu} \qquad \mathrm{Pe} = \frac{c_0 L}{\kappa}$$

for the linear long wave speed (c_0) and height(Lz). ν and κ are the kinematic viscosity and molecular diffusivity.

Following the work of Blanchette [12], we explicitly model sediment pickup below an internal solitary wave. The sediment will similarly obey an advection diffusion equation with an additional forcing term to account for the settling of the particulate phase.

$$\frac{D}{Dt}C - U_s \partial_z C = \frac{1}{Pe}\nabla^2 C. \tag{4.4}$$

C is the relative concentration of sediment with reference value C_0. U_s is the non-dimensional settling velocity.

4.2.1 Density Change

We assume the simplest model to couple the density and the sediment concentration. Here, we use is a linear relation between the density of the sediment and the density of the water. That is,

$$\rho = (1 - C)\rho_f + C\rho_s$$

where ρ_f is the base density of water and ρ_s is the density of the sediment assumed constant.

4.2.2 Boundary Conditions

In order to compose a well-posed problem, we need to supplement the above evolution equations with boundary conditions for the characteristic variables. We assume a periodic domain in the horizontal with a rigid lid in the vertical which imposes a no-slip condition at the top (H) and bottom (h(x)) of the domain. We also impose no-flux conditions for fluid density.

$$\mathbf{u}\Big|_{z=H} = 0 \qquad \partial_z \rho\Big|_{z=H} = 0 \qquad \mathbf{u}\Big|_{z=h(x)} = 0 \qquad \partial_z \rho\Big|_{z=h(x)} = 0.$$

As explained above, we assume a diffusive flux to account for the pickup near the lake bottom. We are following a similar approach to that found in Blanchette *et al.* [12] and Garcia and Parker [40]. The top and bottom boundary conditions are written as

$$\nabla C \cdot \hat{n}\Big|_{z=H} = 0 \qquad \nabla C \cdot \hat{n}\Big|_{z=h(x)} = Pe_s\left(E_s - C\right) \tag{4.5}$$

where $\hat{n}$ is the unit normal. Pe_s is the settling Peclet number and E_S is the prescribed pickup function as defined by [40].

$$E_s = \frac{1}{C_0}\frac{\left(\lambda u^*\right)^5}{1+\frac{1}{0.3}\left(\lambda u^*\right)^5}. \tag{4.6}$$

where λ is empirically defined

$$\lambda = a^{\frac{1}{5}}\frac{U^*_{max}}{U_s}f(Re_p) \qquad f(Re_p) = \begin{cases} Re_p^{0.6} & Re_p > 2.36 \\ 0.586Re_p^{1.23} & Re_p \leq 2.36 \end{cases} \tag{4.7}$$

$$u^* = \left(\frac{\tau_{ij}n_j s_i}{\rho_0}\Big|_{z=h(x)}\right)^{\frac{1}{2}} \qquad Re_p = \frac{d\left(gdR\right)^{\frac{1}{2}}}{\nu}. \tag{4.8}$$

Re_p is the particle Reynolds number, d is the mean grain diameter, g is the acceleration due to gravity and R is the relative density of the sediment, $R = \left(\frac{\rho_s - \rho_f}{\rho_f}\right)$ [Blanchette defined R = 1.5]. The normalized shear velocity (u^*) (with maximum U^*_{max}) is given as the root of the tangential shear rate, calculated based upon the stress tensor τ_{ij}, with bottom unit normal n_j and unit tangent s_j. Finally, a is a fitting constant quoted to be $a = 1.3e\text{-}7$. See [40] for information on construction.

In the low shear limit, we can rewrite this equation to read

$$E_s \simeq \gamma\left(u^*\right)^5.$$

This identified two non-dimensional parameters which are significant for resuspension.

$$Pe_s = \frac{Lc_0U_s}{\kappa} \qquad \gamma = \frac{\lambda^5}{C_0}.$$

4.3 SPINS

SPINS (**SP**ectral **I**ncompressible **N**avier-Stokes **S**olver) solves the incompressible Navier-Stokes problem under the Boussinsq approximation as described in [101]. The code implements tracers (C) which obey a forced advection-diffusion equation

$$\frac{DC}{Dt} = \kappa \nabla^2 C + f$$

For our purposes, the sediment forcing can be written as $f = U_s \partial_z C$ in a Cartesian coordinate system. The boundary conditions are specified by

$$\alpha \partial_z C = \beta$$

where $\alpha = 1$ and

$$\beta \Big|_{z=H} = 0 \qquad \beta \Big|_{z=h(x)} = \frac{(U_s E_s - U_s C)}{\kappa} \tag{4.9}$$

Similarly, we initialize C by some initial value C_0.

4.3.1 Simulations

We consider a stable, continuously stratified two layer fluid with density jump ($\Delta\rho$) and a pycnocline located $0.25Lz$ below the top of the domain. The initial pynocline perturbation mimics a collapse experiment [24], with the initial perturbation in the form of a Gaussian function. This generate an internal wave train dominated by a leading mode-1 wave. Thus, we initialize our non-dimensional density as

$$\rho = 1 - \frac{\Delta\rho}{2} \tanh\left(\frac{z - 0.25 - \eta}{0.125}\right)$$

where here η is the pycnocline perturbation which is given as

$$\eta = \eta_0 \exp\left[-\left(\frac{x - \frac{\delta}{2}}{0.1\delta}\right)^2\right]$$

with $\eta_0 = 0.5\delta$. δ is the ratio of horizontal to vertical scale defined $\delta = \frac{L}{Lz}$.

The resultant internal waves propagate over the topography, which takes the form

$$\text{Hill} = 0.2\text{sech}\,(15\delta x)$$

for the two simulations used to demonstrate the classification into cases which yield transport only and those that yield true resuspension.

Figure 4.1 plots the initialization of the density field (a) and the evolution of the internal waves that develop. Notice that the hill does cause the primary internal wave to deform due to the decrease in water column height. Based upon the computed linear long wave speed, the maximum height of the domain, and viscosity, we estimate the Reynolds and Richardson numbers to be

$$Re \simeq 6.8 \times 10^4 \qquad Ri \simeq 136.$$

In a recent paper by Aghsaee *et al.* [2], a critical parameter curve was identified for internal wave induced boundary layer separation during shoaling. We have considered a similar suite of cases to investigate conditions for true resuspension to take place during shoaling over a linearly sloping bottom,

$$\text{Slope} = \frac{1}{2\delta}\left(x + \frac{\delta}{2}\right).$$

In our case, this constant slope has an angle of approximately six degrees, and hence is more representative of experimental, as opposed to field, situations.

We simulated 24 test cases for various parameters (γ, Pe_s). In some cases, we observed that the internal waves induced significant pickup from the lake bottom. In other cases, virtually none was observed. Table 4.1 organizes the various cases and indicates the value of the dimensionless parameters.

For the present simulations, we used a grid resolution of 2048x384 in all simulations presented here. Due to the natural clustering of points near the boundaries for Chebyshev grids and the spectral accuracy, in addition to grid halving studies, this resolution was deemed sufficient to properly resolve the dynamics of the fluid evolution. The test cases were resolved with a coarse resolution of $2048x128$ as we were not interested in the dynamics of the sediment are only interested in whether or not resuspension was observed.

Lastly, all times indicated are given in reference to output times which is approximately one output for every 0.009 non-dimensional time units.

Case	**d (μm**	U^*_{max} **(m/s)**	γC_0 (%)	Pe_s	**Resuspension**
1	50	0.022519	80.074	0.01054	No
2	50	0.023673	26.691	0.013534	No
3	50	0.022437	120.11	0.010351	No
4	50	0.022687	80.074	0.02188	No
5	50	0.02346	26.691	0.025872	No
6	50	0.023346	26.691	0.012624	No
7	50	0.025238	130.17	0.015796	No
8	50	0.023919	120.11	0.028502	Yes
9	50	0.024579	195.25	0.01384	Yes
10	50	0.022043	160.15	0.037893	Yes
11	50	0.022536	40.037	0.074062	Yes
12	50	0.024526	20.019	0.064618	Yes
13	100	0.022498	275.01	0.55071	Yes
14	100	0.021947	275.01	0.0024324	No
15	100	0.022177	91.669	0.0025626	No
16	100	0.023854	412.51	0.0036894	No
17	100	0.024082	137.5	0.19345	Yes
18	100	0.022942	55.002	0.030361	Yes
19	100	0.023651	275.01	0.017676	Yes
20	100	0.022391	432.21	0.0060342	No
21	100	0.022798	86.441	0.0099044	No
22	100	0.02215	343.76	0.028015	Yes
23	100	0.02268	183.34	0.0043001	No
24	100	0.02268	305.56	0.011467	Yes

Table 4.1: Table of the 24 test cases used to evaluate the conditions for resuspension over a linearly sloped topography. Here d is the mean grain size diameter, U^*_{max} is the maximum shear velocity, γ and Pe_s are the non-dimensional parameters defined in the text and C_0 is the reference concentration by volume (%).

4.4 Results

Propagating internal waves induce shear stress on the lake or ocean bottom. If the shear stress is sufficient to overcome the settling, it will induce pickup, through the pickup parametrization. However, this sediment is confined to the boundary layer near the topography. In fact, in cases where resuspension was observed, we found that the internal wave induced two regions of high sediment concentrations in the boundary layer, one in the acceleration region near the front of the wave, and one near the convergence region in the rear of the wave. In agreement with the literature [2, 16, 23], resuspension was only observed at convergence behind the wave. We observe that sediment ejection out of the boundary layer occurs with the formation and bursting of a separation bubble formed in the posterior side of the internal wave. (If we had simulated internal waves of elevation, the separation point would occur in the front of the wave [97].)

Figure 4.2 outputs the normalized horizontal velocity which clearly identities the separation bubble located in the boundary layer. Once this separation bubble bursts, the resulting velocity field entrains a portion of the sediment found within the boundary layer. For a more complete description of these bursting events, see [3, 46, 47].

Figure 4.3 plots the resultant resuspension associated with a separation bubble bursting event at t = {85,90,100}. This figure has been saturated to 2 times the background concentration (C_0). In this case, we have that $Pe_s = 100$, and γC_0=8.0e-2. Here we clearly observe that the sediment in the boundary layer begins to separate from the topography as a result of the separation bubble (a). This sediment is then resuspended into the water column (b) and is advected by the vortices associated with the busting event (c). This is in agreement with the commonly hypothesized process, though to the best of our knowledge we are the first to model it explicitly.

4.4.1 Effect of Density Coupling

The coupling of the sediment concentration to the density field does not substantially change the global dynamics of the resuspension events. If we turn off the density coupling (i.e. $\rho = \rho_f$), we can rerun the above simulation to see how the density coupling changes the nature of the flow. We will denote these simulations as 'passive' and denote 'active' those simulations where density is coupled to the sediment concentration.

Figure 4.4 outputs the sediment concentration at t = 105 for active (top) and passive (bottom) sediment concentration cases. We observe that the coupling of the sediment concentration to the density field delays the resuspension event. At t=105, the passive

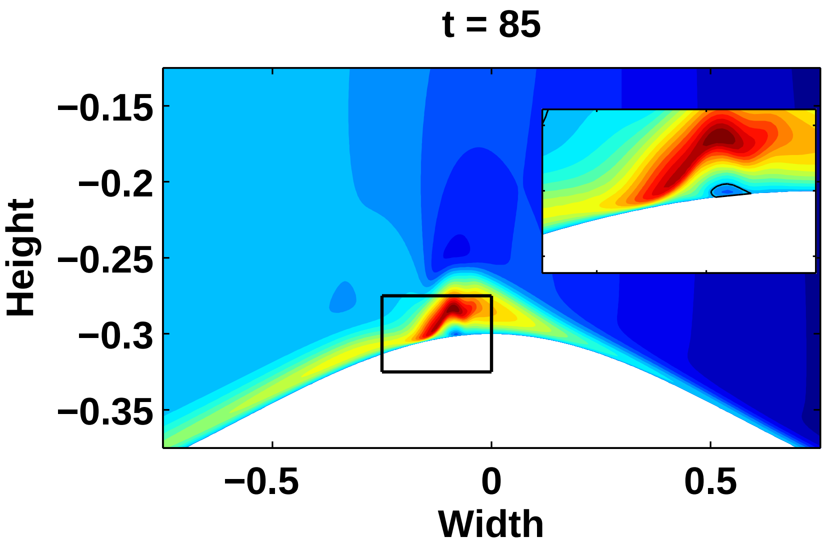

Figure 4.2: Plot of the instantaneous distribution of the normalized horizontal velocity field at t=85. A zoomed window highlighting the separation bubble (contoured in black) has also been provided. Here we notice that the separation of the boundary layer is what results in the ejection of particulate into the water column.

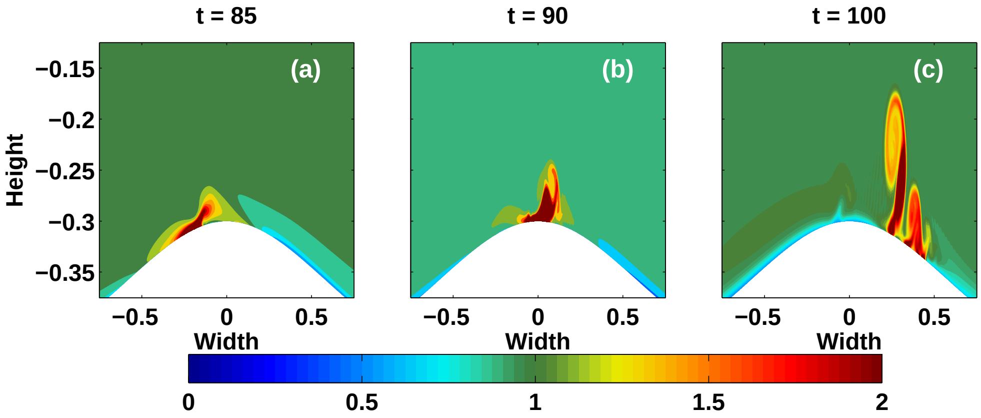

Figure 4.3: Plot of the tracer evolution as it is ejected from the boundary layer. Image has been saturated to a maximum value of C=2.5. Output times were selected to be t = $\{85, 90, 100\}$. $(Pe_s, \gamma C_0) = (100, 8.0e\text{-}2)$.

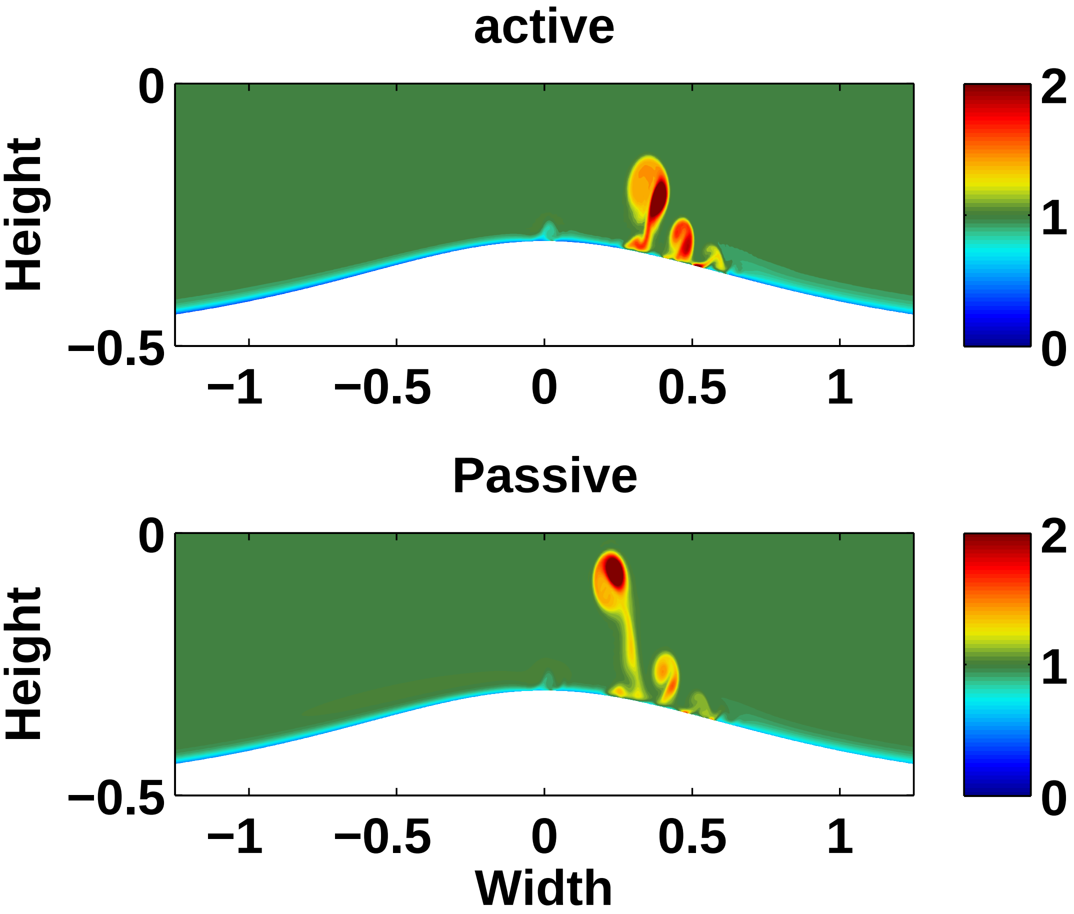

Figure 4.4: Plot of the sediment concentration at t = 105 for the active (top) and passive (bottom) concentration cases. Sediment concentration was saturated at C=2.

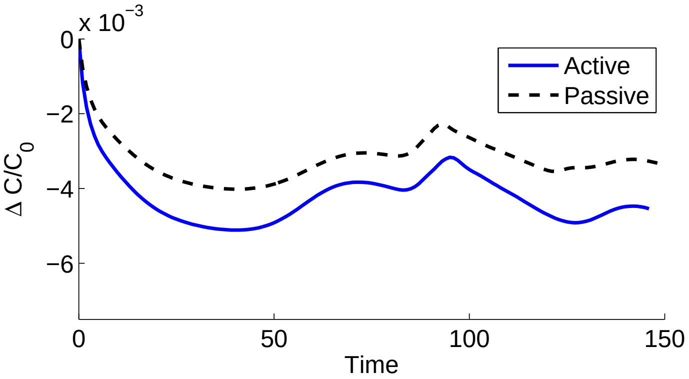

Figure 4.5: Plot of the relative concentration in reference to the initial volumetric concentration (C_0) throughout the simulations.

concentration has already been ejected from the topography, where the active tracer is in the process of ejection. However, the location of ejection was the same. Both cases demonstrate three locations of ejection located at approximately x={0.3,0.45,0.6}.

Looking at the water column as a whole, figure 4.5 plots the total concentration change relative to the initial concentration. We observe that there is a noticeable decrease in the total amount of sediment present in the water column from the passive case. While the global amount of sediment present within the water column is changed by the coupling of density, the large scale dynamics of the resuspension events appears to be almost identical, although delayed.

However, Figure 4.6 demonstrates how a passive concentration can lead to erroneous resuspension events. If we run the present simulation while varying the height of the hill, we can plot the maximum shear stress along topography. When the topography is too small, no separation bubble burst is induced, and hence, no significant shear event is observed. With reference to Fig.4.6, the active(top) and passive(bottom) concentrations induce nearly identical maximal shear stress rates along the lake bottom with the exception of a peak of maximum shear located at t≈120 for the passive Hill1. Thus we see that the passive cases can lead to non-physical bottom shear stress and subsequent pickup. [The cases are labeled according to their relative amplitude (i.e. Hill06 is a hill with height of 0.6 of the original hill)].

For the remainder of this discussion, we present the results for an active sediment concentration. The present subsection was included here in order to demonstrate that for the sediment concentrations found within this paper, the effect of density coupling is

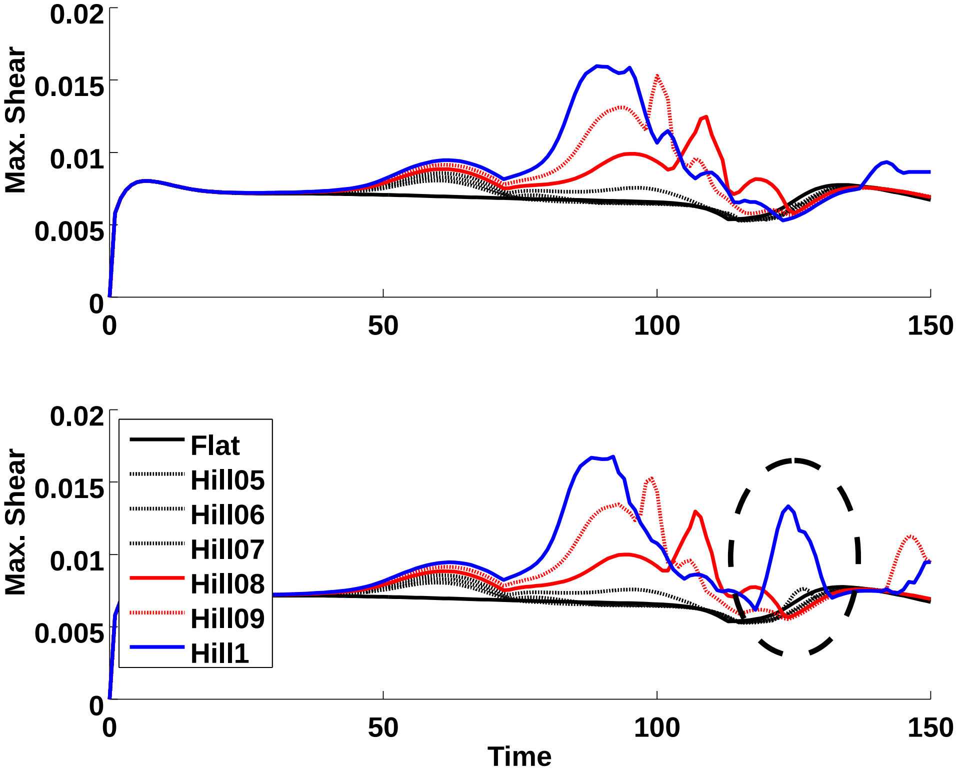

Figure 4.6: Plot of maximum shear for an active (top) and passive (bottom) sediment concentration. Location of erroneous shear peak has been circled.

not a dominant component of the initial bursting events, but does play a vital role in the efficiency of resuspension.

4.4.2 Three-Dimensional Simulation

In order to verify that the above discussion, based on two-dimensional simulations, is correct we ran a three-dimensional simulation to determine the dynamics of the ejection event. In order to accomplish this, we extended the flow at t=80 into the third dimension with a grid size 2048x32x192. A one percent velocity variation was introduced in order to trigger any potential three-dimensionalization.

Figure 4.7 outputs an isocontour of sediment concentration at t=90. Here the isosurface C=1.5 is coloured in green, and C=3 is coloured in yellow. We observe that spanwise motion only becomes significant after the initial ejection event has occurred. As we are primarily interested in the initial ejection event, we argue that the two dimensional approximation is adequate for the present work.

4.4.3 Transport without Resuspension

Not all separation events lead to resuspension. If the internal wave does not induce pickup in the boundary layer, a separation event is incapable of inducing true resuspension. We observed simulations wherein the internal wave was capable of inducing a separation bubble burst with no associated resuspension observed. Figure 4.8 outputs one such simulation at t = {85,90,90}. In this case, we have that $Pe_s = 275$, and γC_0=6.4e-4.

The wave induced bottom shear is insufficient to induce pickup into the boundary layer. However, the dynamics of the bottom layer in a physical lake or ocean are much more dynamic and complex than the simple shear induced pickup model presented here. We mention here that if pickup were induced by another means, a separation event would induce resuspension. Indeed, Hosegood and Van Haren [53] have argued that the sediment fluxes observed in oceans cannot be completely explained by bed shear stress induced pickup. We leave a discussion of the possible non-shear induced pickup mechanisms to a future study.

Thus, we argue here that there exists a parameter regime wherein boundary layer separation occurs with no associated resuspension. In order to determine a criteria for resuspension, we ran 24 test cases for internal waves shoaling on a sloped bottom. Table

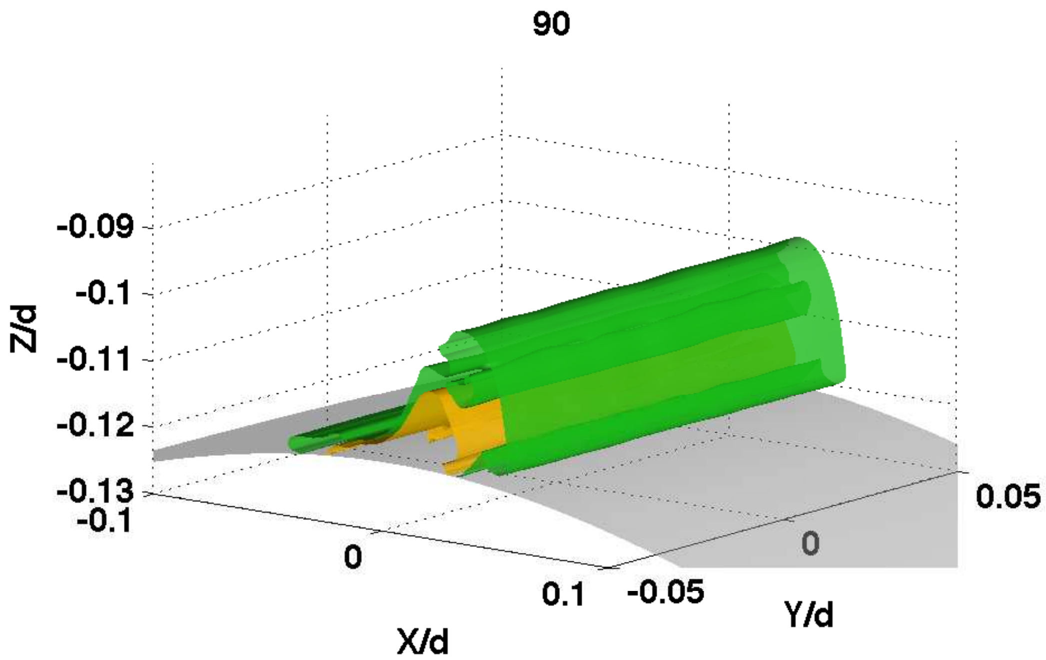

Figure 4.7: A 3D plot of the iso-surface of the sediment concentration at C=1.5 (green) and C=3 (yellow) at t = 90. The topography has been included in gray-scale.

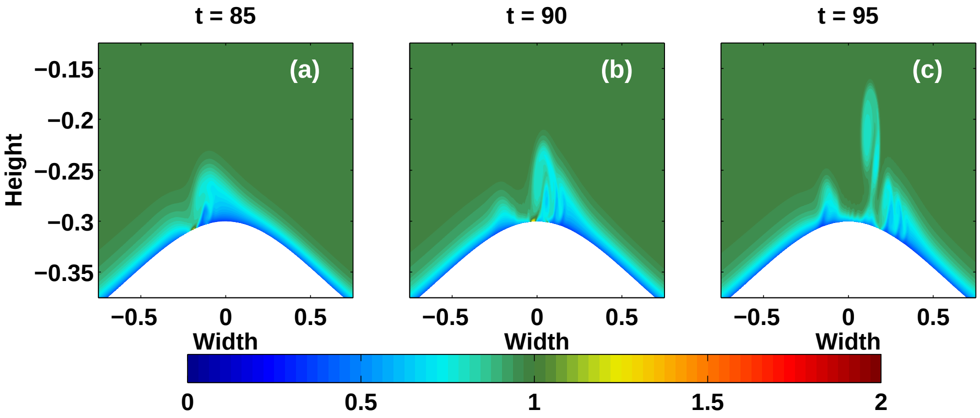

Figure 4.8: Plot of the sediment evolution as it is ejected from the boundary layer. Image has been saturated to a maximum value of C=2. Output times were selected to be t = $\{85, 90, 95\}$. $(Pe_s, \gamma C_0) = (275, 6.4e\text{-}4)$.

4.1 outputs the parameters of each case. Once again, all cases generate sufficiently large waves to induce boundary layer separation.

Figure 4.9 shows the modification of the wave shape during shoaling, and shows a resuspension event at t = 115. Again the image was saturated to a maximum value of C=2. Four isocontours of density have also been superimposed in white to identify the location of the internal wave. Notice here that, as before, we have vorticity roll-up and sediment resuspension behind the leading internal wave. As well, a careful inspection reveals a pickup region in the footprint of the wave. However, it is confined to the boundary layer (near x = 1.5) and hence sediment will not be resuspended.

Figure 4.10 is a scatter plot of the 24 test cases and identifies the cases which induce significant resuspension and those which do not. Here blue dots represent simulations where significant resuspension was observed, and red dots represent simulations which little to no resuspension was found. Circles are associated with a grain diameter of $d = 100\mu m$ and squares with a grain diameter of $d = 50\mu m$. X's mark the location of the two hill topography cases.

Fitting the above data with an exponential curve, we find that a criterion for true resuspension is given by

$$Pe_s \geq 1000 \exp\left[-118\gamma C_0\right].$$

4.5 Discussions and Conclusions

We observe that we can explicitly model sediment pickup and resuspension as a result of internal waves propagating over topography. Here, separation events can induce significant resuspension into the water column, provided that the internal wave is large enough to induce pickup within the bottom boundary layer. This work is presented in support of recent research indicating that internal wave induced boundary layer instabilities can induce resuspension [97, 16, 23]. However, in the absence of other mechanisms, it is observed that boundary layer separation is not always sufficient to induce resuspension. We present here a criterion for internal wave induced resuspension events.

This model for resuspension does not take into account any other mechanisms which can induce pickup. Hosegood and Van Haren [53] have argued that the bed shear stress mechanism does not fully explain the increase in bed flux rates under internal waves. Future work will present the explicit modeling of such effects. Our hope is that field observations and/or experiments will validate our findings.

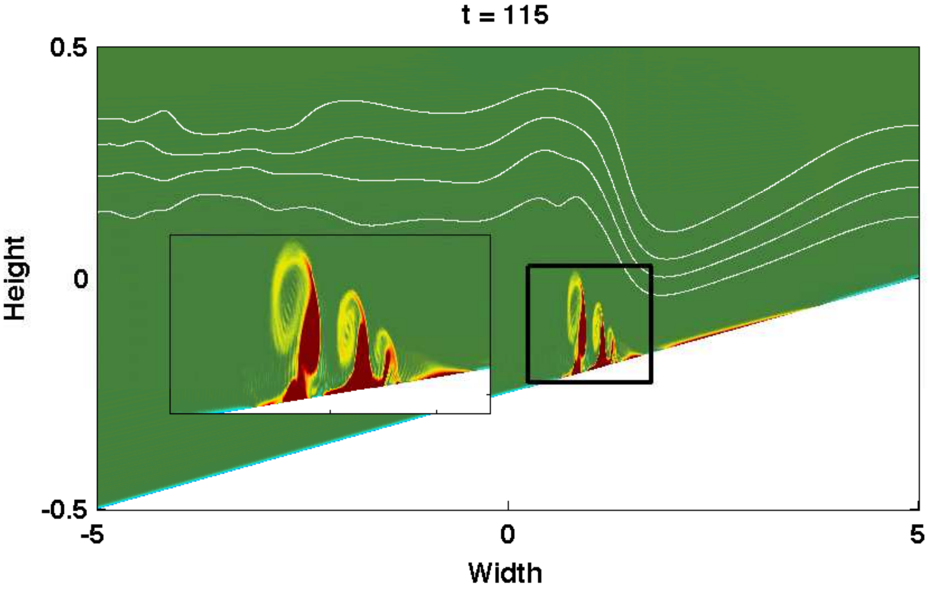

Figure 4.9: Plot of the concentration evolution as it is ejected from the boundary layer as a result of a shoaling internal wave. Image has been saturated to a maximum value of 2.5. Four isocontours of density have been plotted to identify the location of the internal wave. Output time was selected to be t = 115.

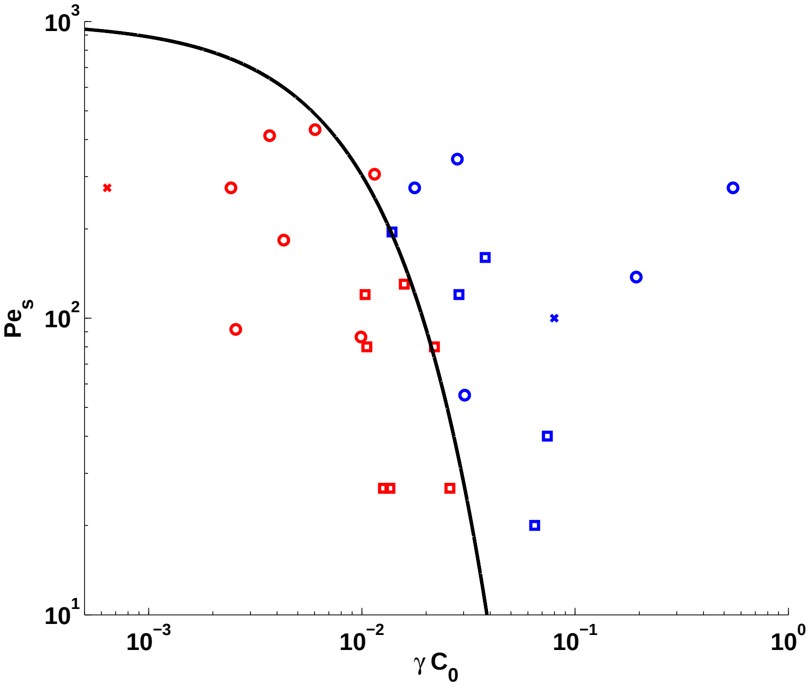

Figure 4.10: Stability plot for various values of γ and Pe_s on a linearly sloped topography. Blue dots corresponds to simulations where pickup occurred and red refer to plots where no significant pickup was observed. Squares correspond to grain sizes of $d = 50\mu m$ and circles to $d = 100\mu m$. Data was fit with an exponential curve, as explained in the text.

Chapter 5

Non-Newtonian Vortex Dynamics

Internal wave induced boundary layer instabilities can lead to the production of vortices near the bottom of lake and oceans. This chapter discusses vortices in non-Newtonian fluid mud and demonstrate that they may significantly contribute to the nutrient circulation system. We begin by briefly discuss previous work on non-Newtonian fluid mud. We describe the numerical method used to solve for the dynamics of vortices in such a fluid. We then discuss non-Newtonian boundary layer theory. Continuing, simulations of vortices in such a fluid are presented. We conclude by discussing the possible implications for lake and ocean dynamics.

I would like to thank Derek Steinmoeller for his contributions to the present work.

5.1 Introduction

The study of fluid mud has received significant attention in the literature [7, 28, 74, 75, 78]. These mud layers are observed to be non-Newtonian in nature, and are often modeled as a power-law fluid [7, 48, 57, 78, 28]. Mehta [74] discusses their formation and growth. However, as noted in a recent paper by Ruyer-Quil *et al.* [86], this model of a non-Newtonian fluid results in a divergence of viscosity at zero strain rate for a shear thinning fluid. In this paper we will thus assume a Carreau-type model[25, 35, 17] for fluid mud. A Carreau fluid has the property that it behaves as a power-law fluid in the high shear rate limit, but as shear rate decreases the viscosity tends to a specified finite, non-zero value. Alternate methods to compensate for the divergence in viscosity incorporate a Hershel-Buckley model [6]. The consideration of such a model will be left to another study.

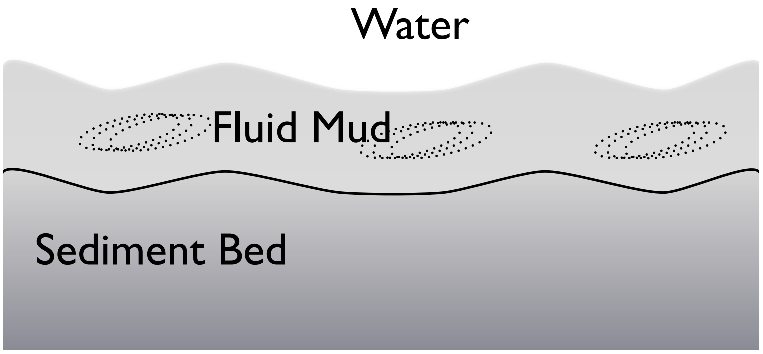

Figure 5.1: Diagram of the basic problem layout. Above the rigid sediment bed, there exists a layer of viscous fluid mud. We attempt to model vortices found within this layer (dotted lines).

Significant interest has recently developed in the impact of vortex rings on sediment beds [11, 77]. These vortices are of critical importance, especially near the bottom boundary layer [71], in driving significant resuspension back into the water column. It is near this bottom boundary layer that we expect to observe fluid mud. Previous studies have attempted to model different characteristics of vortices within such a Carreau-type fluid [35, 17] with Bohme *et al.* [17] considering the breakdown of a vortex in a fluid with a viscosity profile which is qualitatively similar to a Carreau fluid. In this present paper, we attempt to predict the effect that these non-Newtonian vortices have on the resuspension of sediment using a novel pseudospectral method. Based upon a thorough literature search, we believe we are the first to do so.

In order to model the effect that non-Newtonian vortices will have on resuspension, we will assume that there exists a fixed region of fluid mud at the lake bottom, above an impermeable sediment bed. A diagram of this model setup is presented in figure 5.1. Within this mud layer, we look at the effect that the non-Newtonian nature of the flow will have on the boundary layer between the mud and the solid sediment wall. In addition, vortices found within the mud layer (dotted lines in the figure) will propagate and develop in a manner dependent on the rheology of the fluid. As the resuspension of sediment is largely dependent upon the bottom shear rate [11], we look at the shear rate along the bottom solid boundary.

The remainder of this chapter is organized as follows. We begin by discussing the methods used within this chapter including the governing equations, the basic problem layout and the numerical scheme. We then discuss the effect of a non-Newtonian fluid on the boundary layer developing above a solid wall. We proceed to discuss the dynamics of a single elliptical vortex and shielded dipole found within a non-Newtonian layer. We then allow the shielded dipole to impact a solid wall and observe the resultant flow, with a focus on secondary vortex production and repeated collisions in the shear thinning case. We also demonstrate that in a situation with an increase in viscosity and the non-Newtonian nature of the fluid with depth, shear thinning behaviour can counteract the increase in viscosity and yield behaviour typically of much higher Reynolds numbers. Finally, we provide a discussion and conclusion indicating avenues for future research.

5.2 Methods

We consider a two-dimensional, incompressible, non-Newtonian fluid of constant density where the gravity term is absorbed into a modified pressure term. This fluid will obey the Navier-Stokes equations augmented with a non-Newtonian constitutive law

$$\frac{D\mathbf{u}}{Dt} = -\frac{1}{\rho_0}\nabla P + \frac{1}{\rho_0}\nabla \cdot \tau \tag{5.1}$$

$$\nabla \cdot \mathbf{u} = 0 \tag{5.2}$$

The constitutive law for a Newtonian fluid is given as

$$\frac{1}{\rho_0}\tau = 2\nu e_{ij} \qquad e_{ij} = \frac{1}{2}\left(\nabla_i u_j + \nabla_j u_i\right) \tag{5.3}$$

where e_{ij} is the rate of strain tensor and where the kinematic viscosity (ν) is not flow dependent. Any departure of the viscosity from constant that depends on fluid motion indicates a non-Newtonian fluid. Two well known empirical models of the non-Newtonian viscosity are the power law fluid

$$\nu = K\left(\left(I_2\right)^2\right)^{\frac{n}{2}}, \tag{5.4}$$

for which K provides the typical "scale" of the viscosity, and the Carreau fluid, which can be written as

$$\nu = \nu_0\left(1 + \left(\lambda I_2\right)^2\right)^{\frac{n-1}{2}}. \tag{5.5}$$

Here, λ is the relaxation time parameter in seconds. I_2 is the root of the second invariant of the rate of strain tensor

$$I_2 = \sqrt{2\left(e_{ij}e_{ij} - (e_{ii})^2\right)}. \tag{5.6}$$

The second invariant is the sum of the principle minors of e_{ij}. Using the incompressibility condition, we can simplify the second invariant as

$$I_2 = \sqrt{2e_{ij}e_{ij}}. \tag{5.7}$$

As mentioned in the introduction, the Carreau fluid model has some advantages over the typical power law model, since viscosity tends to a finite reference value as the shear rate tends to zero. Shear thinning fluids (n<1) are those whose viscosity decreases as a function of shear rate. Shear thickening (n>1) fluids have a viscosity which increases as a function of shear rate. Figure 5.2 plots representative viscosity curves based on shear rate.

We can then rewrite equation (5.1) in dimensionless form, with primes denoting dimensionless variables, as

$$\frac{D\mathbf{u}'}{Dt'} = -\nabla P' + \frac{1}{\mathrm{Re}}\nabla \cdot \left[\left(1 + \gamma^2 I_2'^2\right)^{\frac{n-1}{2}} \nabla' \mathbf{u}'\right] \tag{5.8}$$

where the primes are dropped for the remainder of this paper for simplicity and we define

$$\mathrm{Re} = \frac{UL}{\nu_0} \qquad \gamma = \frac{\lambda U}{L} \tag{5.9}$$

for typical values of velocity (U), length (L) and constant reference viscosity (ν_0). We similarly non-dimensionalize both the horizontal and vertical length scales by L.

For the purposes of this present paper we will consider three cases for $n = \{0.5, 1, 1.5\}$ being shear thinning, Newtonian, and shear thickening, respectively. As cited by Balmforth [7], typical non-Newtonian parameter values for mud are n$\approx$ 0.3. Uddin [105] and Ruyer-Quil [86] both consider other shear thinning fluids with values of $n \approx 0.3 - 0.6$. As a conservative estimate for the parameter n, we consider shear thinning parameter n = 0.5.

5.2.1 Numerical Method

The Navier-Stokes equations are solved with a standard pressure projection method (henceforth PP). The various flavours of PP for Newtonian fluids have been thoroughly explained

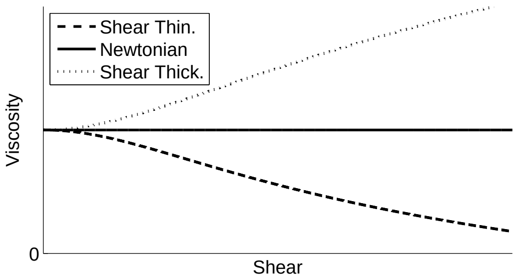

Figure 5.2: A representative plot of the change in viscosity as a function of shear rate for a Carreau fluid. Examples of shear thinning and shear thickening fluids are illustrated.

in the literature[4]. A very popular approach in the method-of-lines framework[103] is the high-order stiffly-stable splitting algorithm detailed by Karniadakis *et al.* [62]. The method first forms a predicted velocity $\hat{\mathbf{u}}$ by explicitly evolving the advection terms with a linear multi-step method. The projection step involves solving the following Poisson equation, along with suitable boundary conditions [62], for the pressure p at time $t_{k+1} = t_k + \Delta t$:

$$\frac{1}{\Delta t}\left[\nabla \cdot \hat{\hat{\mathbf{u}}} - \nabla \cdot \hat{\mathbf{u}}\right] = -\nabla^2 p^{k+1} \,, \tag{5.10}$$

an equation that can be obtained by taking the divergence of the semi-discrete form of the momentum equation after the advective terms have been evolved but before consideration of the viscous terms. $\hat{\hat{\mathbf{u}}}$ is the predicted velocity field after the projection step. The divergence free constraint is subsequently enforced by removing the $\nabla \cdot \hat{\hat{\mathbf{u}}}$ term in (5.10). This is equivalent to projecting the approximate solution onto the space of approximately non-divergent velocity fields. Once p^{k+1} has been computed, the pressure gradient is evolved in the semi-discrete form of Navier-Stokes momentum equations to recover the corrected velocity field,

$$\hat{\hat{\mathbf{u}}} = \hat{\mathbf{u}} - \Delta t \nabla p^{k+1} \,. \tag{5.11}$$

The viscous terms can subsequently be evolved to recover $\mathbf{u}^{k+1}$ using implicit time-stepping from the backward differentiation formula (BDF) family of time integrators. In the case of a shear rate dependent viscosity the problem becomes strongly nonlinear, though by evaluating the viscosity at the intermediate stage following (5.11), the problem is linearized, and following a suitable application of the product rule, a robust algorithm results. The resulting semi-discrete Helmholtz-type equation is

$$\mathbf{u}^{k+1} - \beta_0 \Delta t \hat{\hat{\nu}}' \nabla^2 \mathbf{u}^{k+1} = \beta_0 \Delta t \nabla \hat{\hat{\mathbf{u}}}^k \cdot \nabla \hat{\hat{\nu}}' + \hat{\hat{\mathbf{u}}} \,, \tag{5.12}$$

where $\nu' = Re^{-1}\left(1+\gamma^2 I_2'^2\right)^{\frac{n-1}{2}}$, and $0 < \beta_0 \leq 1$ depends on which BDF method is used. Here, we use $\beta_0 = 1$, corresponding to Euler's method. This is a semi-implicit equation for velocity $\mathbf{u}^{k+1}$ which we solve via an iterative scheme.

The spatial discretization techniques adopted are highly accurate pseudospectral methods [19]. In doubly-periodic domains, Fourier grids are used in each direction. In the periodic channel geometry, a Chebyshev grid is used in the vertical coordinate to impose the no-slip boundary condition at the top and bottom of the channel. In all cases, differential operators can be defined using a matrix-free FFT-based formulation (to avoid the large, dense matrices that are produced by pseudospectral methods). The pressure Poisson problem is solved by first taking the Fourier transform of equation (5.10) along any periodic dimension. In doubly periodic domains, the 2D problem is reduced to a simple algebraic relation that must be inverted for each two-dimensional Fourier mode. In the finite channel case, the problem is transformed to a collection of decoupled 1D linear systems that can be directly solved in Matlab with relative ease. Since the viscosity operator contains a spatially-varying coefficient, the Fourier modes become coupled and the transform techniques used for the pressure problem cannot be applied to the viscous problem. Instead, the viscous problem is solved iteratively with Matlab's built-in generalized minimum residual (GMRES) iterative solver together with suitable pre-conditioning.

5.2.2 Problem Layout

In order to provide a complete picture of the non-Newtonian effect acting within the fluid mud layer near the rigid sediment bed, we consider three distinct physical setups. First, we consider a non-Newtonian boundary layer. Second, we examine both a single vortex and a shielded dipole in a doubly periodic domain. Finally, we consider a shielded dipole impacting a solid wall. Table 5.2.2 organizes the various cases along with their respective parameter values.

The first case is that of a boundary layer near the solid sediment layer. On short time-scales, the effect of viscosity will be negligible within the main water column but will be dominant near the solid boundaries, where the shear rate is high. For this reason, non-Newtonian effects will be especially pronounced close to the wall. We derive a non-Newtonian boundary layer equation and solve the non-linear problem for the velocity profiles using an iterative scheme.

For the second case, we assume a doubly periodic domain. Here, we study the effect of the non-Newtonian viscosity on vorticity and its implications in fluid mud. We consider both a single elliptical vortex as well as a shielded dipole.

The single vortex is initialized using a Gaussian function for vorticity:

$$\frac{\omega}{\omega_0} = \exp\left[-\left(\left(\frac{x}{3}\right)^2 + z^2\right)\right] \ . \tag{5.13}$$

Using the RMS-velocity as the characteristic velocity scale and the domain length for the characteristic length, Re $\approx 20,000\pi$. The self-induced currents of the vorticity will cause the vortex to spiral and form of an axisymmetric distribution of vorticity, that is, the elliptical vortex will transition to a circular vortex, possibly with tendrils that extend out from the main vortex body. For simplicity we set $\lambda = 1$ ($\gamma \approx 1.4$).

Previous work on vortex interaction with a solid wall has been performed using a shielded dipole [26, 27]. Following these articles, we initialize a shielded dipole by specifying the velocity profile:

$$\begin{aligned}\frac{u}{u_0} = z\Bigg(& \exp\left[-\frac{x_1^2+z^2}{\sigma}\right] \\ & - \exp\left[-\frac{x_2^2+z^2}{\sigma}\right]\Bigg) \ , \end{aligned} \tag{5.14}$$

$$\begin{aligned}\frac{w}{u_0} = \Bigg(& - x_1 \exp\left[-\frac{x_1^2+z^2}{\sigma}\right] \\ & + x_2 \exp\left[-\frac{x_2^2+z^2}{\sigma}\right]\Bigg) \ , \end{aligned} \tag{5.15}$$

where

$$x_1 = x + \frac{1}{10}, \qquad x_2 = x - \frac{1}{2}, \qquad \sigma = \frac{1}{100}. \tag{5.16}$$

If we once again use the RMS-velocity as the characteristic velocity, we find that Re $\approx 26,000$. Here, to estimate the non-Newtonian effect of the fluid, we set $\lambda = 0.1$ ($\gamma \approx 2.6$).

To quantify the effect of viscosity over time, we will look at two metrics for the motion, the kinetic energy and the enstrophy. Both of these can be defined as

$$\text{KE} = \int \frac{1}{2}\left(u^2 + w^2\right) dA, \tag{5.17}$$

$$\text{Enst.} = \int \omega^2 dA \tag{5.18}$$

Case	**Fluid**	**n**	λ	γ
Boundary Layer	-	-	-	1
Elliptical Vortex	Shear Thinning	0.5	1	1.4
	Newtonian	1	1	1.4
	Shear Thickening	1.5	1	1.4
Shielded Dipole	Shear Thinning	0.5	0.1	2.6
	Newtonian	1	0.1	2.6
	Shear Thickening	1.5	0.1	2.6
Dipole-Wall Interaction	Shear Thinning	0.5	0.1	2.6
	Newtonian	1	0.1	2.6
	Shear Thickening	1.5	0.1	2.6

Table 5.1: Table of the various dynamical cases presented below.

where ω is the vorticity.

Finally, we allow the shielded dipole (equations (5.14-5.15)) to impact a solid wall. Here, we impose the no-slip boundary conditions at the wall

$$u\Big|_{z=-\frac{1}{2}} = 0, \qquad w\Big|_{z=-\frac{1}{2}} = 0. \tag{5.19}$$

In order to evaluate the effect of the interaction of the dipole with the wall, we examine the shear rate along the bottom boundary,

$$\text{Shear} = \frac{\partial u}{\partial z}\Big|_{z=-\frac{1}{2}}. \tag{5.20}$$

So as to provide consistency between different simulations, we normalize all simulation time scales to unity. Thus, all simulations run between $0 \leq t \leq 1$.

5.3 Boundary Layer

In the boundary layer it will be true that

$$U \gg W \ , \qquad L \gg H. \tag{5.21}$$

Assuming a Carreau fluid model, we can expand the second invariant to find that, to first order, in the boundary layer,

$$I_2 \sim u_z,\ 1 + (\gamma I_2)^2 \sim \gamma^2 u_z^2, \ \text{ where } \gamma u_z \gg 1 \tag{5.22}$$

or that the power law fluid constitutive law can be applied. Under the standard boundary layer scaling arguments [63], we can then write the boundary layer equations, with no pressure forcing, as

$$u_x + w_z = 0 \ , \tag{5.23}$$

$$u u_x + w u_z = \frac{1}{\mathrm{Re}_{BL}} \partial_z \left([u_z]^n \right) \ , \tag{5.24}$$

$$\frac{1}{\mathrm{Re}_{BL}} = \frac{\nu_{NN}}{LU} \frac{L^2}{H^2} \ , \tag{5.25}$$

$$\nu_{NN} = \nu_o \left(\frac{\gamma U}{H} \right)^{n-1} \ . \tag{5.26}$$

As a simple solution to the boundary layer problem, we assume that the external flow is constant, $U = U_e$. In addition, we will assume a similarity solution within the boundary layer so that

$$u = g(\eta) \ , \qquad \eta = \frac{z}{\delta(x)} \ . \tag{5.27}$$

Using a streamfunction (the existence of which is guaranteed by incompressibility), we can then write

$$u = \partial_z \psi \ , \qquad w = -\partial_x \psi \ , \qquad \psi = \delta(x) f(\eta) \ . \tag{5.28}$$

Substituting these relations into the boundary layer equations, we determine the boundary layer thickness to be

$$delta = \left(\frac{x\nu_0}{U_e^{2-n}} \lambda^{n-1} \right)^{\frac{1}{n+1}} . \tag{5.29}$$

Hence, the boundary layer equation becomes

$$f''(\eta)^{n-1} f'''(\eta) + \frac{1}{n(n+1)} f(\eta) f''(\eta) = 0, \tag{5.30}$$

$$\lim_{\eta \to \infty} f'(\eta) = 1, \tag{5.31}$$

$$f'(0) = 0, \tag{5.32}$$

$$f(0) = 0. \tag{5.33}$$

Evaluating the boundary layer problem at $x = 1$, we can compare the various profiles by rescaling the problem to form a consistent coordinate system. The rescaled boundary layer coordinate is defined as

$$\eta^* = \eta \frac{\delta(1)}{\delta_N(1)} = \eta \gamma^{\frac{n-1}{n+1}} \frac{\nu_0^{\frac{1}{n+1}}}{\nu_0^{\frac{1}{2}}} \tag{5.34}$$

where δ_N is the boundary layer thickness for the Newtonian case.

Figure 5.3 plots the resultant u profiles for shear thinning (n=0.5), Newtonian (n=1), and shear thickening (n = 1.5) cases. We give upper and lower bounds for the Newtonian case assuming that the viscosity increases and decreases by a factor of two. That is, the upper and lower bounds are given by $\nu = 2\nu_0$ and $\nu = 0.5\nu_0$ respectively.

We observe that the non-Newtonian nature of the flow yields a boundary layer with a qualitatively different structure. The shear thinning fluid is nearly identical to the Newtonian case for $\eta^* < 1$. However, for increasing η^*, the thickness of the shear thinning boundary layer decreases to that of a fluid with half the viscosity. Thus the shear thinning decreases the boundary layer thickness by about 30% from Newtonian. The structure of the boundary layer of the shear thickening fluid is substantially different from the Newtonian case, with a thickness nearly twice that of the Newtonian case. We also notice that the shear thickening and Newtonian upper bound curves cross at $\eta^* \approx 2.5$, indicating that Newtonian and non-Newtonian boundary-layers are geometrically different in nature. We discuss the potential implication of these profiles in the discussion section below.

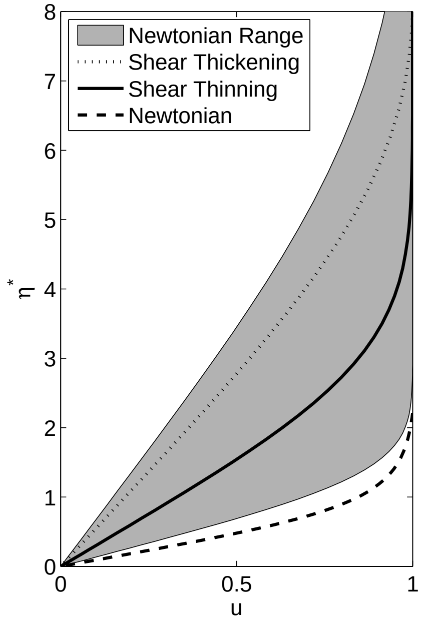

Figure 5.3: A comparison of shear thinning (n=0.5), Newtonian (n=1) and shear thickening (n=1.5) boundary layer velocity profiles. We also provide upper and lower bounds for the Newtonian case assuming the viscosity increases and decreases by a factor of 2. That is, the upper and lower bounds of the region are given by $\nu = 2\nu_0$ and $\nu = 0.5\nu_0$ respectively. Boundary layer coordinates have been rescaled to provide a standardized coordinate system.

5.4 Doubly Periodic Domain

5.4.1 Single Vortex

We initialize a single vortex, as described by equation (5.13), in a doubly periodic domain. Allowing this vortex to evolve, we plot the vorticity at various output times in figure 5.4. Here, the panels are plotted at $t = \{0.25, 0.5, 0.75\}$.

For the Newtonian vortex({b,e,h}), the vortex begins to spiral, inducing a galaxy-like tendril structure. For a more technical discussion, see McWilliams [73, Chapter 3]. The viscosity then diffuses the tendrils, resulting in a circular vortex which will itself slowly decay in time. In contrast, the shear thickening fluid ({c,f,h}) quickly diffuses any trace of these tendrils. We see that by t = 0.5, the tendrils are being quickly diffused, and by t = 0.75, the vortex has decayed significantly more than its Newtonian counterpart.

The shear thinning fluid conveys a very different story. Here we observe the opposite effect to the shear thickening case. At t = 0.5, we see that the vorticity of the shear thinning case is nearly identical to the Newtonian vortex. As time progresses, we see a clear differentiation occurring so that by t = 0.75, the vortex tendrils are still largely present. The shear thinning nature of the fluid preserves the small scale features of the vorticity. This effect will have a substantial impact when we consider the case of a vortex dipole colliding with a solid boundary below in section 5.5.

Figure 5.5 plots both the kinetic energy and enstrophy as a function of time. As expected, the shear thinning fluid preserves the kinetic energy and enstrophy over a longer period compared to the Newtonian fluid. A shear thickening fluid rapidly diffuses both the vorticity and momentum, and hence damps both the total kinetic energy and enstrophy.

5.4.2 Shielded Dipole

We can similarly observe non-Newtonian effects acting on a shielded dipole, as defined in equations (5.14, 5.15). The dipole's flow field causes it to propagate in space, in the negative z-direction. Figure 5.6 plots the vorticity of the shear thinning (a), Newtonian (b), and shear thickening (c) dipole along with the natural logarithm of the corresponding spectra of kinetic energy at t = 0.25. Each vorticity plot has been shifted in order to ensure that the dipole remains centered. The log of the spectra have been saturated to values between -2 and 8 and only a subset of wave numbers is shown, for optimal viewing. Looking at the spectra, it becomes very clear that the shear thinning fluid has significantly more energy in small length scales than the corresponding shear thickening case.

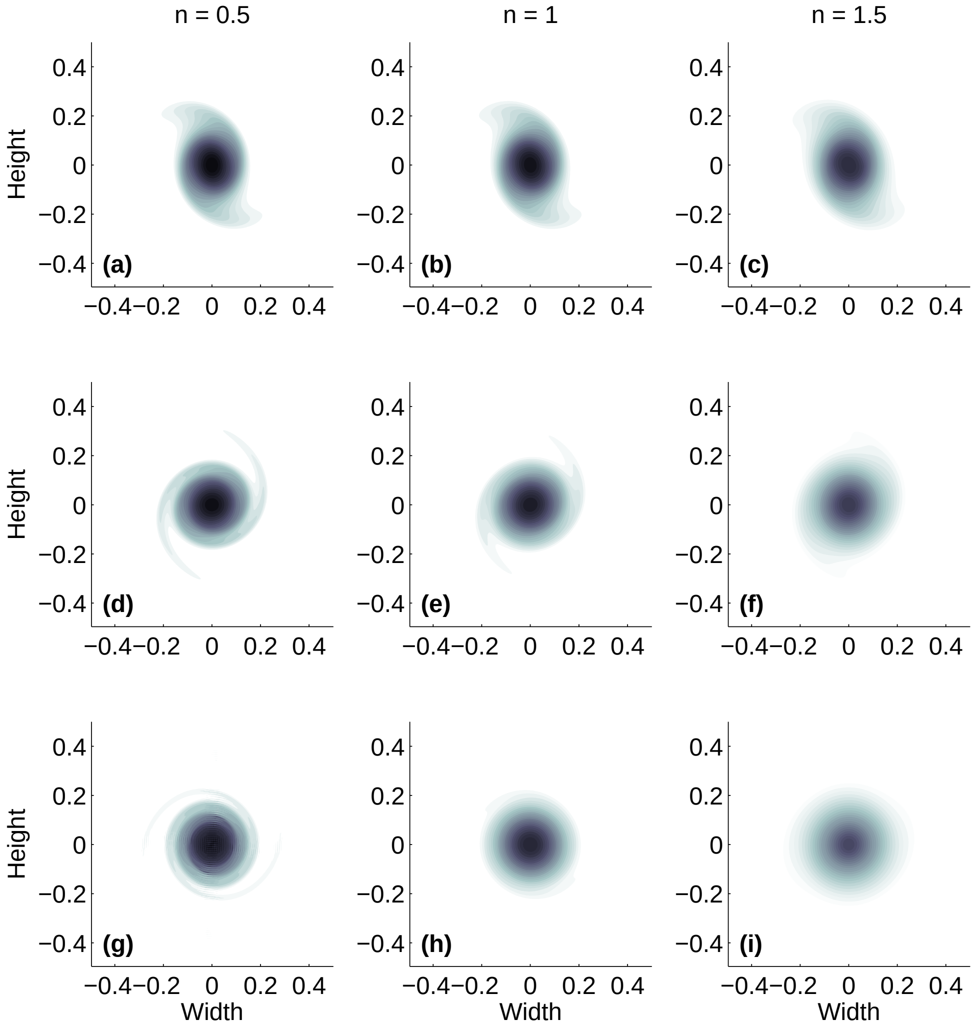

Figure 5.4: Plot of the evolution of a shear thinning (n=0.5), Newtonian (n=1) and shear thickening (n=1.5) vortex. Output times have been taken at t = 0.25 {(a),(b),(c)}, t = 0.5 {(d),(e),(f)} and t = 0.75 {(g),(h),(i)}. Notice that the shear thickening damps out almost all of the dynamics by t = 0.5, and the shear thinning fluid preserves its small scale features. In each panel, the vorticity has been scaled by the maximum value of the initial vorticity field.

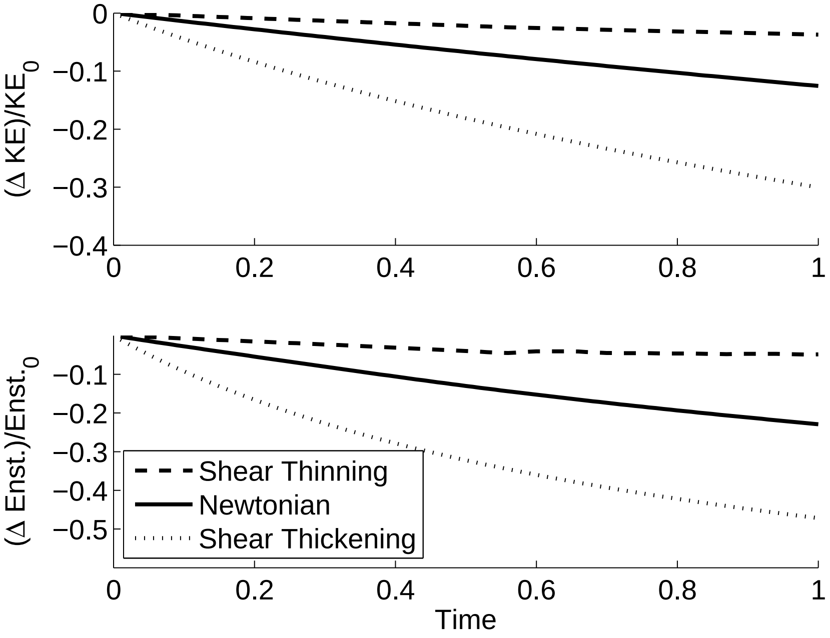

Figure 5.5: Plot of the percent decrease in kinetic energy (top) and enstrophy (bottom) of the initial vortex over time. As expected, the shear thinning fluid maintains its energy over a longer period of time than the other two examples. The shear thickening fluid rapidly loses both energy and enstrophy.

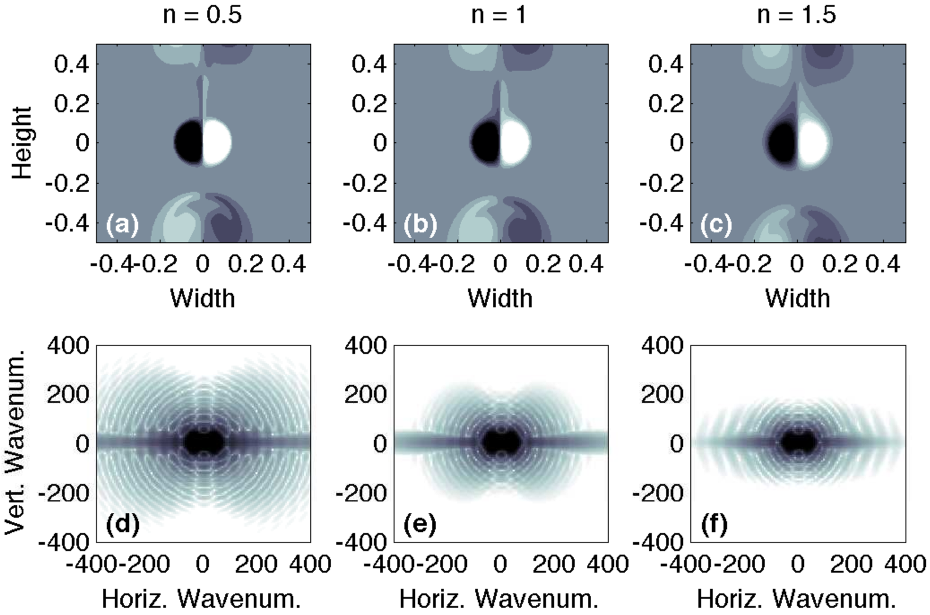

Figure 5.6: Plot of the shifted vorticity for the shear thinning (a), Newtonian (b) and shear thickening dipole (c) at t = 0.25. Here we also plot the natural logarithm of the corresponding spectra of the kinetic energy {(d),(e),(f)}. The log spectra was saturated between values of -2 and 8. Spectra has been windowed in order to provide clarity of the image. The dipole is moving in the negative z-direction.

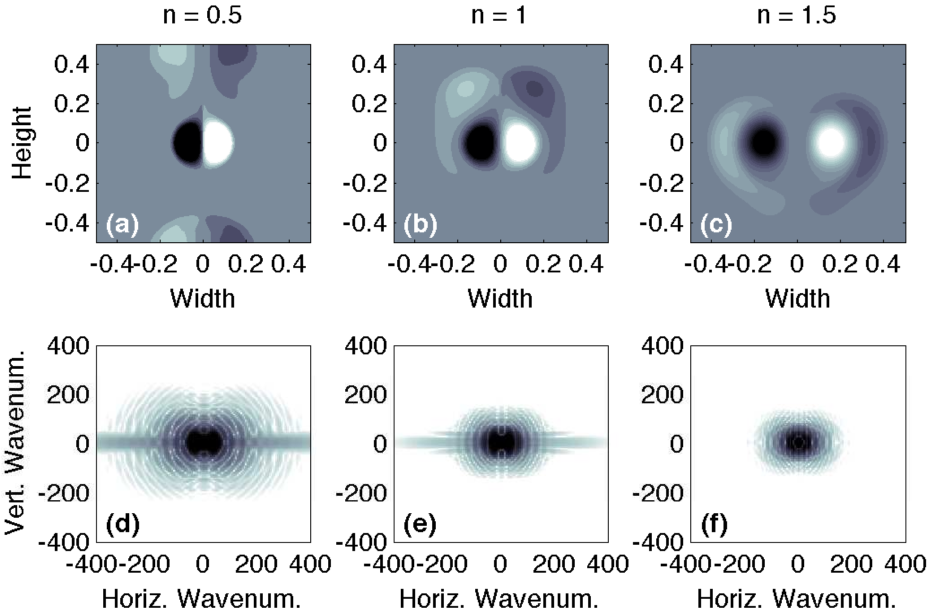

Figure 5.7: Plot of the shifted vorticity for the shear thinning (a), Newtonian (b) and shear thickening dipole (c) at t = 0.75. Here we also plot the natural logarithm of the corresponding spectra of the kinetic energy {(d),(e),(f)}. The log spectra was saturated between values of −2 and 8. Spectra has been windowed in order to provide clarity of the image.

Due to the periodicity of the domain, the propagating dipole will interact with the remnant of vorticity from the initialization. This interaction occurs at approximately t = 0.5 and acts to slow the dipoles. Figure 5.7 is the analogue of figure 5.6 for time t = 0.75. We can see here that the shear thickening dipole becomes trapped by the interaction while the shear thinning dipole continues to propagate along. The spectra further clarify the disparity in scales between the three cases. It is very clear that the spectra of the shear thinning case (d) have energy at shorter wavelengths, where the shear thickening case has virtually none. As we discuss below, these small scale features can have a significant effect on the global flow over a long time-scale.

Looking at the energy and enstrophy plotted in figure 5.8, we find that the results are similar to those found previously (in figure 5.5). We find that only about 20% of the kinetic energy has been lost for the shear thinning case, whereas over half of the kinetic energy of the shear thickening fluid has been removed by t=1.

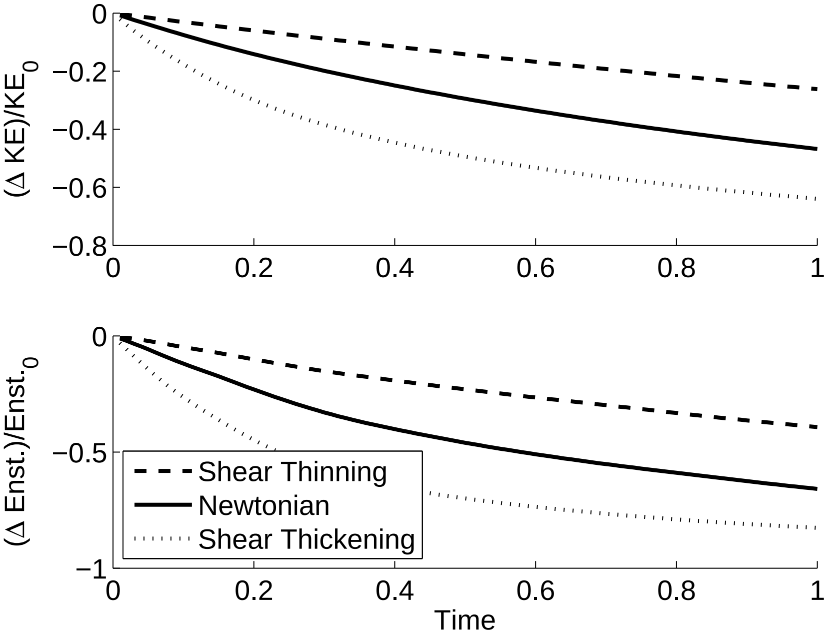

Figure 5.8: Plot of the percent decrease in kinetic energy of the initial vortex-pair over time. As expected, the shear thinning fluid maintains its energy over a longer period of time than the other two examples. The shear thickening fluid rapidly loses both energy and enstrophy.

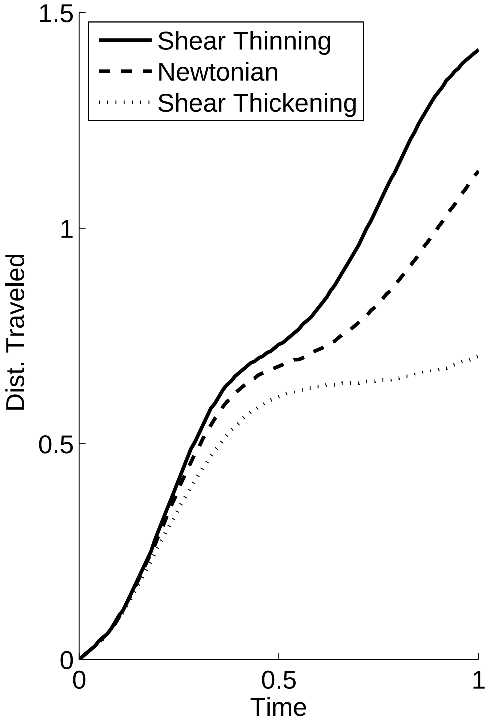

Figure 5.9: Plot of the position of the dipole over time. As a result of the decrease in viscosity, the shear thinning dipole travels significantly faster than the other two cases.

As the viscosity begins to diffuse the vorticity of the dipole, the self-induced currents begin to wane and the dipole begins to slow down. Figure 5.9 plots the location of the point of maximum vorticity as a function of time and thus tracks the dipole as it progresses. What we see is that the shear thinning fluid maintains its velocity over time. In all cases, we see a decay in the dipole velocity, which is especially true for the shear thickening dipole. What we see is that the shear thinning fluid velocity decreases at a much slower rate than the other cases. As time progresses, the difference in position increases. As mentioned before, the dipole interaction with the remnant vorticity amplifies the disparity in position.

5.5 Wall

As the vortices within the viscous mud layer impact the solid porous layer, they can induce significant ejection of particulate back into the main water column [11]. Sediment resuspension can be directly correlated to bottom shear stress (see Blanchette *et al.* [12] and the references therein). To model the vortex induced shear rate within a non-Newtonian fluid, we allow the shielded dipole discussed above to impact a solid no-slip wall and observe the result. Figure 5.10 shows the resultant structure of the dipole as it impacts the wall. Here, $t = \{0, 0.25, 0.5\}$. There exists a substantially different structure of vorticity in all three cases.

At t = 0.25 in Figure 5.10(d-f), we see that there is already a clear difference in the location of the dipole. Moreover, the choice of rheology has already altered the spatial distribution of vorticity and velocity, in a manner that is consistent with simulations presented in section 5.4.2.

Once this dipole impacts the solid wall, we see that in the shear thickening fluid case, the dipole has diffused significantly and largely lost its initial vorticity. The Newtonian case, in contrast, maintains some structure, with two rebounding dipoles visible, albeit much weaker than the initial dipole. The shear thinning fluid has an entirely different structure to the flow than the other two cases. Here, two asymmetric dipoles have been generated by the interaction of the initial dipole with the boundary. Each new dipole exhibits significant structure on small length scales.

Examining the kinetic energy and enstrophy in figure 5.11, we notice that again the shear thinning fluid maintains its kinetic energy significantly longer than the shear thickening fluid. Notice now, however, that in this case when the dipole impacts the wall at $t \approx 0.31$, there is sharp decrease in the kinetic energy. This is especially significant in the Newtonian case, but is observable in all cases. In addition, there is a substantial amount of vorticity generation during the interaction of the dipole with the boundary layer. In particular, we see that when the dipole impacts the wall, there is a seven-fold increase in enstrophy from the initial condition. This increase in vorticity is what results in the asymmetric dipole structures visible in figure 5.10(g).

We next consider the shear rate along the bottom wall. Figure 5.12 shows a waterfall plot of the normalized bottom shear rate (left) along with the maximum shear rate as a function of time (right), normalized by the absolute maximum shear rate of the Newtonian case. Here we see that the impact of the dipole on the wall induces a significant amount of shear along the bottom boundary. Indeed, the shear thinning case induces up to five times more shear rate at the bottom wall than the Newtonian case.

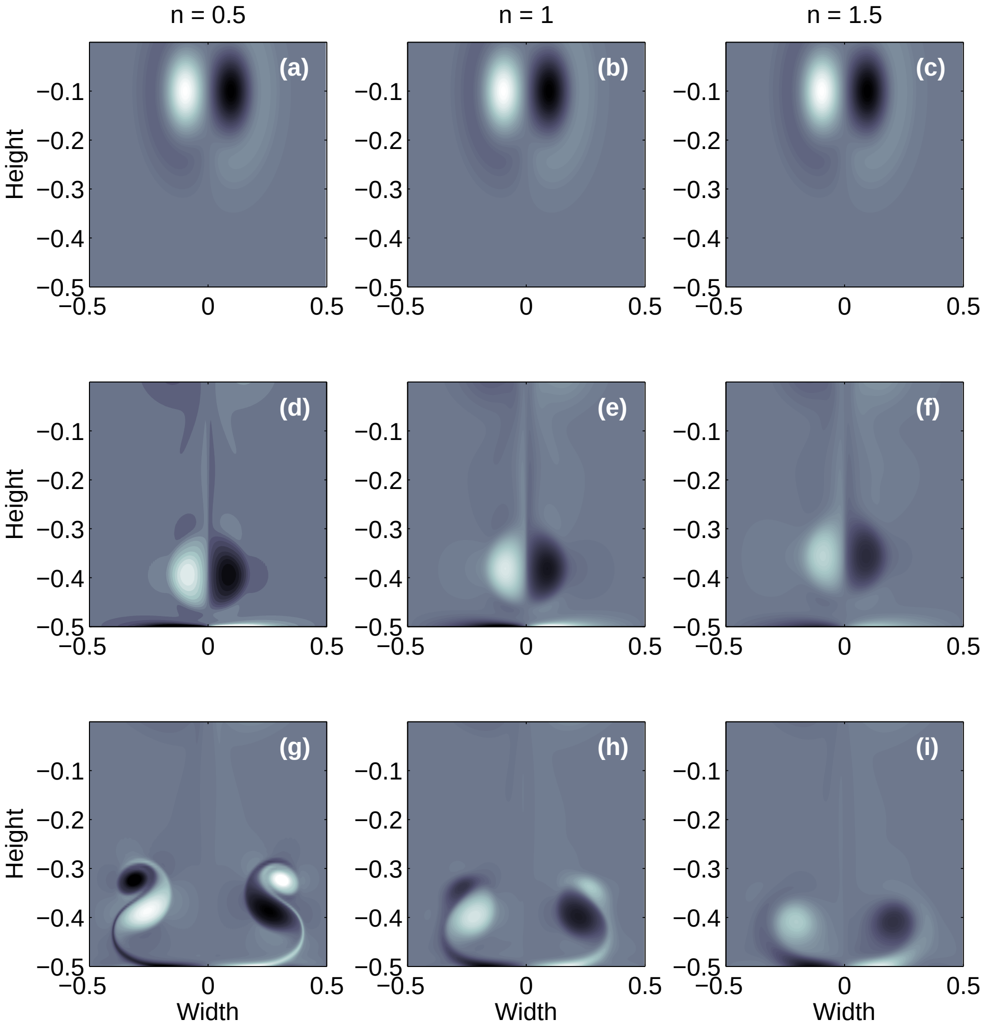

Figure 5.10: Plot of the evolution of vorticity for a shear thinning (n=0.5), Newtonian (n=1) and shear thickening (n=1.5) vortex. Output times have been taken at t = 0 {(a),(b),(c)}, t = 0.25 {(d),(e),(f)} and t = 0.5 {(g),(h),(i)}. Notice that here, unlike the previous examples, the structure of the flow has been significantly altered as a result of the change in viscosity. In each panel, the vorticity has been scaled by the maximum value of the initial vorticity field.

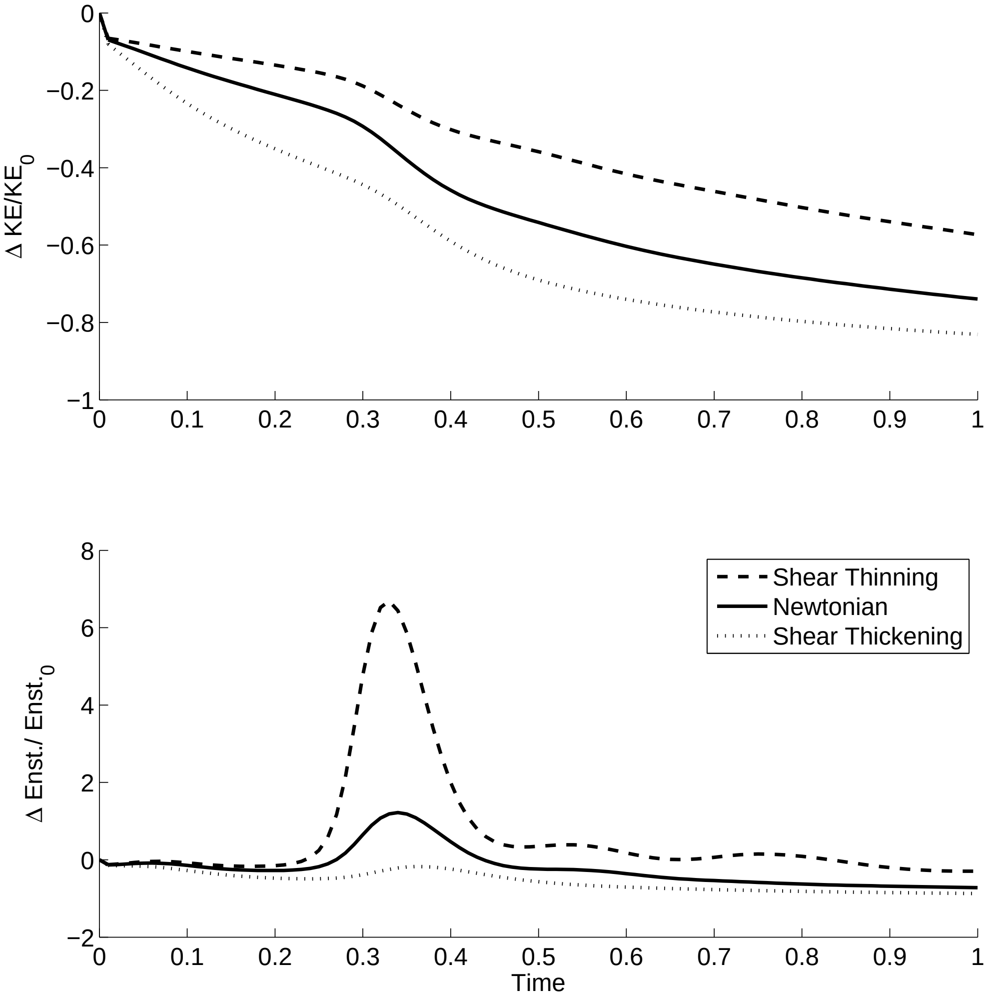

Figure 5.11: Plot of the decrease in kinetic energy of the initial vortex over time. Here the effect of the wall is clearly seen at t ≈ 0.31. The wall causes the kinetic energy to rapidly decrease with a rapid increase in enstrophy.

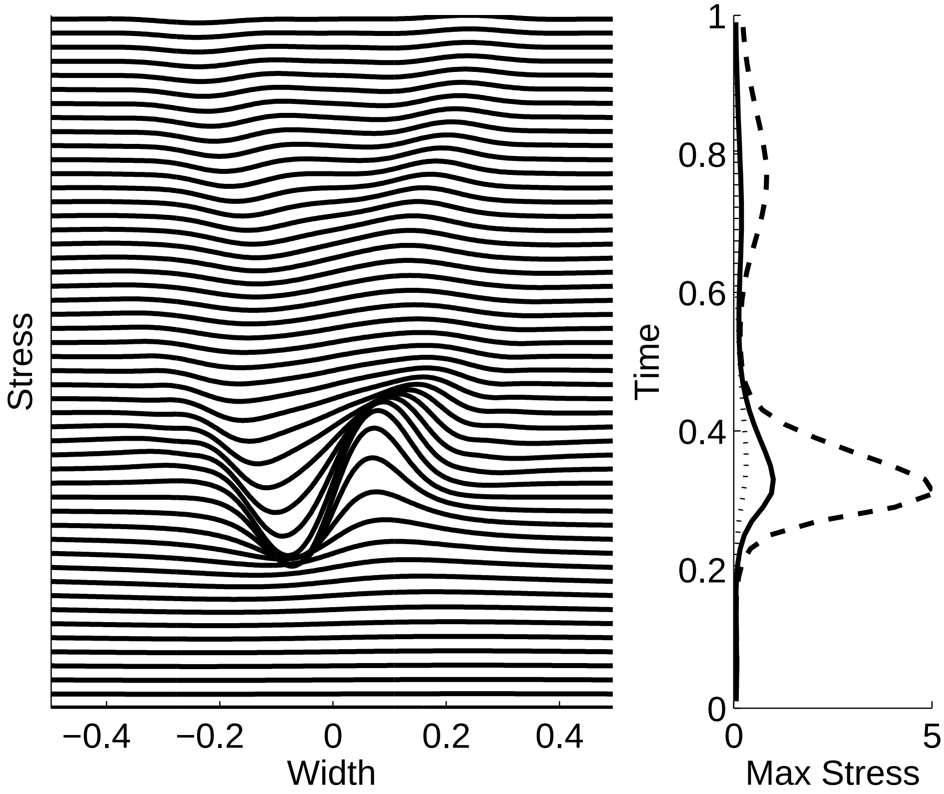

Figure 5.12: Waterfall plot (left) of the shear rate along the bottom boundary over time (Newtonian case shown). Notice that the impact of the dipole causes a significant amount of shear rate along the bottom. The maximum shear rate on the bottom boundary is plotted (right), normalized to the absolute maximum of the Newtonian case. Here we plot the shear thinning fluid (−−), the Newtonian fluid (−), and the shear thickening fluid (··).

A second point to note is that, near $t = 0.8$, we see that there is a second peak in shear rate for the shear thinning case as a result of the secondary impact of the dipole. Figure 5.13 shows the spatial distribution of vorticity during this secondary impact of the shear thinning dipole and compares it to the Newtonian. We see that the shear thinning dipole slams into the wall a second time where the Newtonian dipole has mostly diffused away. This secondary dipole impact induces as much shear along the bottom boundary as the Newtonian case. As the boundary layer is significantly larger for the shear thinning case, and since the shear thinning nature of the fluid preserves the small scale features of the flow, this has the potential to cause a cascade of subsequent lake bottom impacts not observed in the Newtonian case. Similar roll-ups have been observed for Newtonian fluids in various parameter regimes [77, 27] (typically associated with a higher Reynolds number).

5.5.1 Mud Layer

As particulate matter begins to settle out of suspension, the concentration of particulate will increase towards the bottom of the water column. As such, the value of density, viscosity and the fluid rheology will vary [60]. In order to simulate this effect, we reconsider the previous simulation and set the viscosity within our box of fluid to increase by a factor of two over the vertical extent of the domain, and similarly allow the non-Newtonian parameter n to decrease by a factor of two over the vertical extent of the domain.

$$n = 1 + (n_0 - 1)\exp\left[-\frac{z+\frac{1}{2}}{0.25}\right], \tag{5.35}$$

$$\nu = \nu_0\left(1 + \exp\left[-\frac{z+\frac{1}{2}}{0.25}\right]\right) \tag{5.36}$$

Clearly, for the Newtonian case ($n_0 = 1$) the value of n will be constant throughout the domain.

Figure 5.14 plots the observed vorticity structure at $t = 0.5$. The shear thinning fluid [$n_0 = 0.5$](a) maintains some of its structure from the previous example but it is clear that the increase in viscosity has significantly diffused the flow. Similarly, the Newtonian case [n_0=1] (b) has also diffused the flow, resulting in a structure similar to that found in the shear thickening case above in figure 5.10(i). Figure 5.14(c) plots the vorticity found in figure 5.10(g) for comparison.

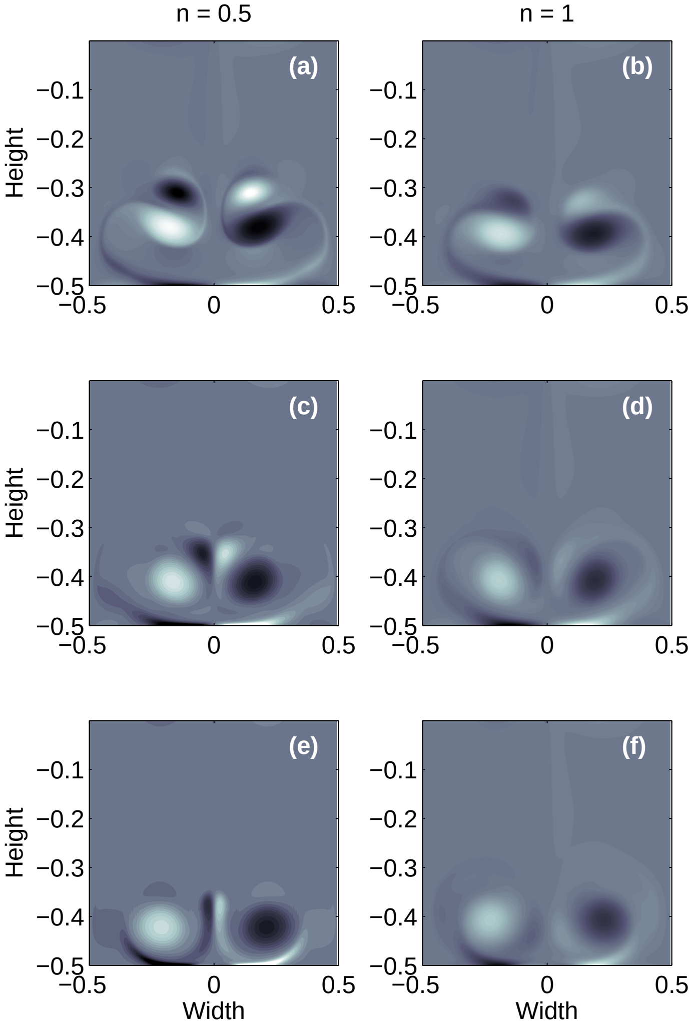

Figure 5.13: Plot of the evolution of vorticity for a shear thinning (n=0.5), and Newtonian (n=1) dipole. Output times have been taken at t = 0.6 {(a),(b)}, t = 0.7 {(c),(d)} and t = 0.8 {(e),(f)}. In each panel, the vorticity has been scaled by the maximum value of the initial vorticity field.

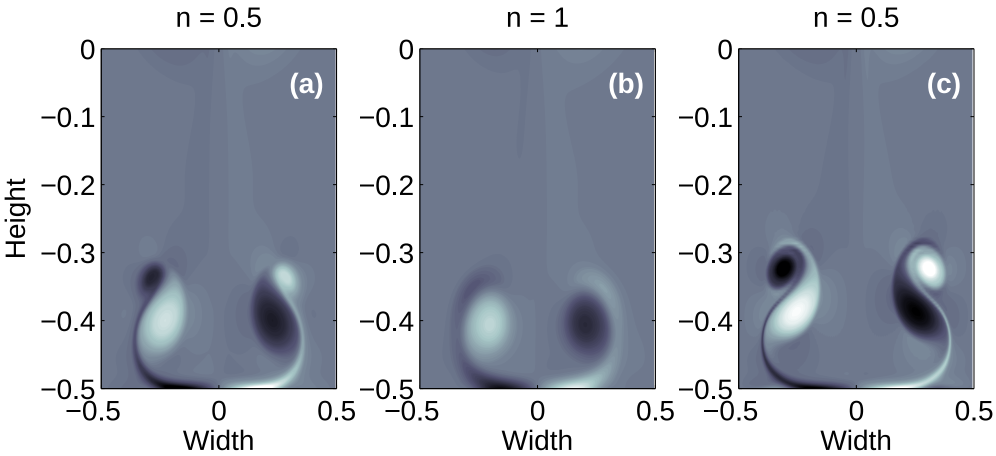

Figure 5.14: Plots of the vorticity at t = 0.5 for the shear thinning (a) and Newtonian (b) cases under a variance of viscosity and n. Panel (c) plots the vorticity found in figure 5.10(g) for comparison.

Figure 5.15 plots the shear rate along the bottom boundary. Here, there is significantly less shear along the wall upon impact than we observed previously. We extract the Newtonian profile from the previous example (figure 5.12), and compare it with the results found here, and observe that despite the viscosity doubling, the non-Newtonian nature of the flow is enough to compensate for the increased viscosity. As shown in figure 5.15, there is a twofold increase in shear rate along the bottom boundary layer from the constant viscosity Newtonian case. This result suggests that the increase in fluid viscosity will not necessarily overcome the non-Newtonian effects induced within the fluid mud layer.

5.6 Discussion and Conclusions

In this paper we have used pseudospectral methods to model the flow of vortices evolving within a Carreau fluid. While similar numerical methods for non-Newtonian fluids have been employed in other contexts [57, 56], we are unaware of any other publication that has used these methods to solve the full, incompressible non-Newtonian momentum equations to model the dynamics of non-Newtonian vortices. Pseudospectral methods offer a number of advantages over other numerical methods due to their excellent resolution characteristics and high-order accuracy[19]. The Fourier method is especially useful in problems with a

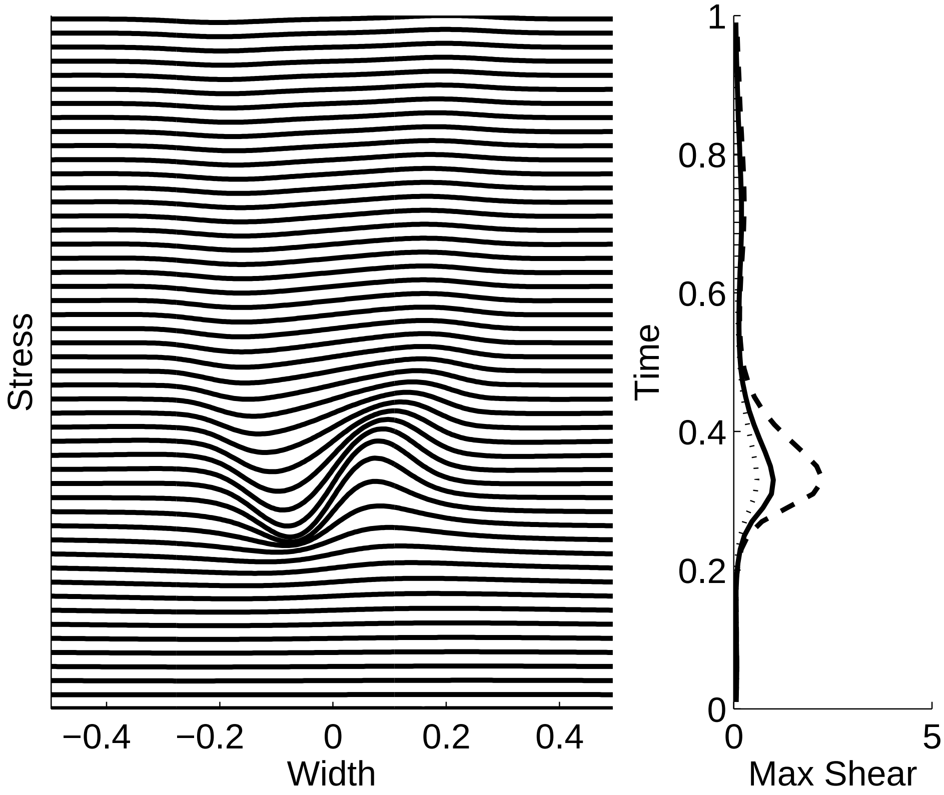

Figure 5.15: Waterfall and shear rate plot similar to figure 5.12. Notice that the shear rate is significantly less than that found previously. Upon comparison with the Newtonian case found in figure 5.12, we see that despite the increase in viscosity, the shear thinning nature still causes an increase in bottom shear rate, although diminished for the previous shear thinning case. Plotted are the shear thinning fluid (−−), the constant viscosity Newtonian fluid (−), and the viscosity varying Newtonian fluid (··).

periodic horizontal coordinate, and the Chebyshev method is ideal for resolving viscous boundary layers since it naturally clusters grid points near solid boundaries [103]. These methods are easily extended to three-dimensional problems [101] and this provides a clear avenue for future study.

The interaction of vortices with a boundary layer has been shown to be quite complex [29, 71]. Similarly, Ozdemir *et al.* [81] have considered the complex processes leading to the relaminarization of a mud laden boundary layer (or lutocline), using a Newtonian fluid. They however did not consider resuspension or non-Newtonian effects. As such, it is important to understand how the non-Newtonian nature of a fluid affects the structure of a boundary layer near a solid wall. In fact, the difference in structure of the boundary layer has important implications to resuspension. As we mentioned previously, the effect of viscosity is pronounced within the boundary layer, as this will be the region of largest shear rate. This shear rate is what will eventually induce the resuspension of sediment back into the water column. As we have discussed above, the shear thinning fluid generates a much smaller boundary layer when compared to the other cases. While the full implications of this effect are not fully known, we argue that it results in a significantly higher gradient near the boundary which can lead to significantly more pickup. Further study of these boundary layers and their impact on resuspension needs to be performed with a more complete model that accounts for buoyancy effects.

In an attempt to understand how vortices evolve within a non-Newtonain fluid, we simulated the evolution of an elliptical vortex and a shielded dipole. It was observed that the non-Newtonian nature of the fluid affected the small scale features of the flow. A shear thickening fluid diffuses the small scale features, whereas a shear thinning fluid will preserve them. This is one indication that the non-Newtonian nature of fluid mud must be included in models to correctly model lake bottoms. We observe a significant difference in the vorticity dynamics as a direct result of the non-constant viscosity.

Chapter 6

Fluid Circulation and Seepage in Lake Sediment due to Propagating and Trapped Internal Waves

The following discussion of internal wave induced seepage has been previously published in water resources research.

> Olsthoorn, J., M.Stastna, and N.Soontiens (2012), Fluid circulation and seepage in lake sediment due to propagating and trapped internal waves, Water Resour. Res., 48, W11520, doi:10.1029/2012WR012552.

Permission to use this work has been provided in Appendix 7.

I would like to thank Nancy Soontiens for her assistance with the present work.

In the following discussion, we demonstrate that internal waves can induce significant seepage through the porous lake and ocean bottom. This has important implications to the nutrient circulation system as internal waves may prove to the dominant seepage forcing mechanism in water columns of depths greater than a few meters. The following exposition demonstrates that internal waves can induce greater seepage than their surface water counterparts due to their large wavelength, slow evolution, and large pressure signature at the bottom of the water column.

6.1 Introduction

Flow through permeable lake, coastal, or river sediment has received significant attention in the literature [21, 34, 42, 50, 85]. The resultant flow in, and out, of the porous medium can have profound implications on bed-water column heat and chemical exchange [1, 50, 58, 76]. In turn, this exchange can have implications for food web dynamics, especially in nutrient limited situations such as those that occur in oligotrophic lakes. The primary means of generating flow through a porous lake bottom is through spatially varying pressure fluctuations at the sediment-water interface (henceforth SWI) [34]. Natural waters exhibit motions, and hence pressure fluctuations, on a wide variety of length scales ranging from variations in boundary layer turbulence due to bottom ripples on the scale of centimeters to basin scale motions on the scale of kilometers. A commonly observed cause of bottom pressure fluctuations in shallow water is surface waves. At depths greater than a few meters, the bottom pressure signature of these waves is weak. However, most lakes and coastal waters are stratified for at least some portion of the year and the resulting density stratification can serve as a wave guide for internal wave motion. Internal waves are typically longer than surface waves, are slow moving, and due to the small density differences across the thermocline, can reach large amplitude. Moreover, they are often long lived and hence can induce significant bottom currents and pressure fluctuations with a characteristic geometric pattern that differs from surface wave induced fluctuations.

The range of motions of a density stratified fluid including interaction with a wind driven surface wave field and bottom topography is truly bewildering. No numerical model we are aware of covers all these scales of interest, and even if one were available, the problem of isolating particular phenomena would be extremely difficult. In stratified lakes, a typical situation leading to the generation of large amplitude internal waves is schematized in Figure 1. In the upper panel a persistent wind has induced a downwind tilt of the lake surface and a corresponding larger upwind tilt of the thermocline. In the lower panel, after the wind slackens, the internal seiche steepens due to finite amplitude effects and leads to the formation of a train of finite amplitude internal waves. These waves are both nonlinear and non-hydrostatic, and thus present a challenge for many lake scale models. Measurements of this scenario have been reported in the literature for geography as varied as Lake Kinneret, Israel [14], Lake Constance, Germany [83], and Toolik Lake, Alaska, USA [72]. A significant body of literature is available on coherent aspects of internal wave motions. In particular, the fully nonlinear theory leading to the Dubreil-Jacotin-Long (DJL) equation which describes internal solitary waves (ISWs) and steady trapped waves (see the review [49] and [94] for recent discussions) provides an easy to use tool with which to address internal wave-induced motions in the porous bottom. Observations of supercritical internal waves have also been reported in [30].

Darcy's law is a classical, experimentally determined relationship which relates pore pressure gradients in a porous medium with the seepage rate (often also referred to as filtration, or filtration rate). Given a pressure distribution at the SWI, Darcy's law thus provides an effective way of determining the flow in the porous medium [79, ch.1]. Various refinements of Darcy's law have been proposed, including the Brinkman and Forchheimer terms. These attempt to partially account for shear stress and finite Reynolds number, respectively [76, 79]. However, neither modification comes with a firm range of applicability and, in the present context, the literature suggests neither is important [76]. Any modelling effort attempting to include these refinements would also need to consider a generalized boundary condition, as discussed in the classical paper by Beavers and Joseph [9] and in a more recent comparative work [70]. In the present work, we will use Darcy's law only, and hence we can supply all the necessary boundary conditions at the SWI by invoking continuity of pore pressure with the bottom pressure in the free fluid. We assume that the seepage through the porous medium is small, consistent with literature on the damping of linear and weakly nonlinear surface gravity waves by flow over a porous region [37, 82]. This assumption allows us to solve for the pressure at the SWI based purely on the physics in the free fluid. This pressure profile subsequently drives the seepage in the porous medium. The coupling across the SWI is thus one way, in the sense that the modification of the flow in the free fluid due to the porous medium is neglected. This one way coupling is justified by the vast separation of scales between ISW induced velocities and velocities within the porous medium.

Motivated by the findings of [106] who demonstrated that convection is insufficient to explain the seepage through the porous bottom of marine sand, the above described approach has been explored by a number of authors, generally in an attempt to study seepage due to surface wave induced flow over topography (e.g. ripples with centimeter scales), and has demonstrated noticeable seepage in the porous layer [93, 34, 89, 55, 20, 54]. We argue here that internal waves induce substantially more seepage through the porous domain than surface gravity waves in lakes deeper than a few meters. We note that the exact composition of a particular lake bottom may be different from that found in the coastal ocean, however for the following discussion ocean bottom and lake bottom will be used interchangeably. This may have to be revisited in any future work that compares the theory with field observations.

While we are concerned here mainly with the seepage through the porous layer, we note that Shum [93] has constructed a model to explicitly model the flow of solutes through the porous layer. Similarly, a recent study by Grant *et al.* [44] argued that the mass transport through the hyporheic zone may be significantly different than previously thought. We

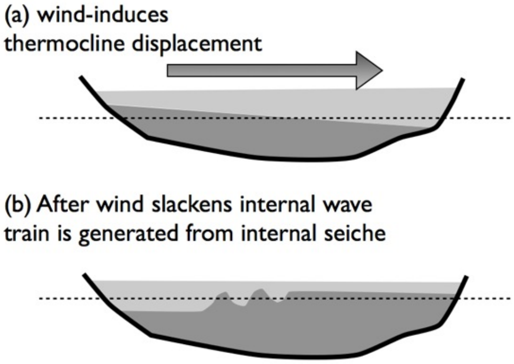

Figure 6.1: Diagram of the formation of an internal wave-train by the steepening of a lake scale seiche. In the upper panel, a persistent wind causes a downwind tilt of the lake surface and a corresponding larger upwind tilt of the thermocline. In the lower panel, after the wind slackens, the internal seiche steepens due to finite amplitude effects and leads to the formation of a train of finite amplitude, non-hydrostatic internal waves.

leave the coupling of such work with internal waves for future investigations.

The remainder of the article is organized as follows: We briefly discuss the comparison between surface gravity waves and internal waves and their generation. The governing equations for the free fluid and their various manipulations used to find finite amplitude internal waves are also briefly summarized. This is followed by a statement of the boundary value problem in the porous medium, and a brief discussion of numerical methods. The results are divided into three parts. First, we discuss the effect of the wavelength of the pressure profile at the SWI. Second, we analyze a single, propagating internal solitary wave and the seepage it induces. We discuss the effect of varying the depth of the porous layer and vertical variation in permeability (or permeability stratification). We subsequently move on to flows induced by trapped internal waves over topography. Finally, we propose a scenario during which the wave-induced boundary layer instabilities [32, 98] modify the permeability distributions beneath and downstream of the wave, and hence lead to increased seepage in the porous medium and transport across the SWI. The final section reviews the findings and discusses future directions.

6.2 Methods

6.2.1 Surface and Internal Waves

The linear wave theory for surface gravity waves (SGWs) has been studied extensively (See [31, 63] for a full derivation and exposition). The three key aspects of SGWs which we will focus on are that, in comparison to internal waves: 1) SGWs have relatively short wavelengths, 2) SGWs have comparatively fast propagation speeds, and 3) the amplitude of the pressure profile induced by SGWs decays exponentially with depth of the water column. In particular, if we consider a surface wave with a sinusoidal form, an angular frequency ω, and a wavenumber k, the phase and group speed of rightward propagating waves are given by

$$c_p = \sqrt{kg \tanh kH}$$

and

$$c_g = \frac{c_p}{2}\left[1 + \frac{2kH}{\sinh 2kH}\right],$$

while the pressure distribution at the bottom of a lake with uniform depth H is given by

$$P + \rho g H = \frac{\rho g a}{\cosh(kH)} \cos(kx - \omega t). \tag{6.1}$$

Here, a is the amplitude of the gravity wave, H is the depth of the lake and g is the acceleration due to gravity (see [63]).

For the theoretical description of ISWs, we consider an incompressible, inviscid fluid in a fixed reference frame under the Boussinesq and rigid lid approximations. The fluid motion is thus governed by the Euler equations, expressing the conservation of momentum,

$$\frac{\partial \vec{u}}{\partial t} + \vec{u} \cdot \vec{\nabla} \vec{u} = -\frac{1}{\rho_0} \vec{\nabla} p + \frac{\rho}{\rho_0} \vec{g} \tag{6.2}$$

the incompressibility condition, expressing conservation of mass,

$$\vec{\nabla} \cdot \vec{u} = 0 \tag{6.3}$$

and the density equation

$$\frac{\partial \rho}{\partial t} + \vec{u} \cdot \vec{\nabla} \rho = 0 \tag{6.4}$$

where $\vec{u} = (u, w)$ represents the fluid velocity, p the pressure, ρ the total density, ρ_0 a constant reference density, and $\vec{g}$ the acceleration due to gravity. As is customary, we assume that the density can be decomposed into a background profile $\bar{\rho}(z)$, which depends only on the vertical coordinate, and a perturbation. The total density can be written in terms of the far upstream profile, $\rho(x, z, t) = \bar{\rho}(z - \eta)$, where $\eta(x, z, t)$ defines the isopycnal displacement from its far upstream height. The buoyancy, or Brunt-Väisälä, frequency $N(z)$, which is defined via the relation

$$N^2(z) = -g \frac{1}{\rho_0} \frac{d\bar{\rho}}{dz} \tag{6.5}$$

gives the frequency of oscillations of a fluid particle infinitesimally displaced from its resting height z. In a lake, the density would be determined via an equation of state from the temperature.

While the above equations are suitable for a time dependent simulation, a far simpler description is possible for either a propagating internal solitary wave (ISW) or a steady internal wave trapped over topography. In both of these situations the Euler equations can be reduced, via a series of somewhat complicated algebraic manipulations (see [94, 96] for a detailed derivation), to a single, scalar equation for the isopycnal displacement $\eta(x, z, t)$. This is the well-known Dubreil-Jacotin-Long (DJL) equation,

$$\nabla^2 \eta + \frac{N^2(z - \eta)}{U_0^2} \eta = 0 \tag{6.6}$$

where U_0 is the wave propagation speed for ISW and the upstream velocity for trapped waves. The boundary conditions far upstream and downstream are that η tends to zero, while both the rigid lid at the top (at $z = H$) and variable bottom (at $z = h(x)$) are streamlines.

From a mathematical point of view, the DJL equation is formally elliptic and strongly nonlinear. Not surprisingly, no non-zero analytical solutions are known (except for the special situation when $N^2(z)$ is constant). However, numerical methods for the DJL equation are readily available, and have resulted in a great deal of insight into finite amplitude ISWs and trapped waves.

Briefly, both ISWs and trapped waves are "long waves" in the mathematical sense. The practical implication of this fact is that, unlike the exponential decay of the pressure

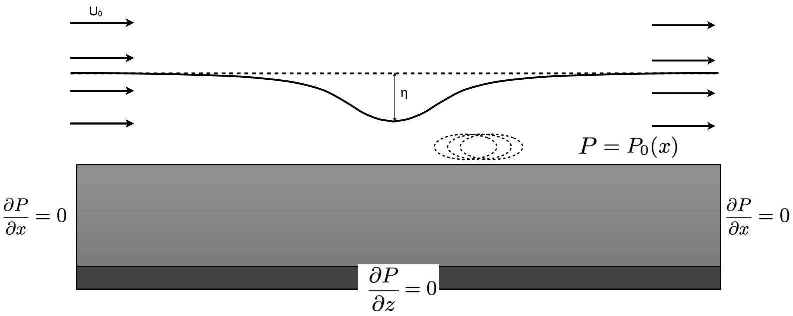

Figure 6.2: Diagram of the basic problem layout. Note the inflow and outflow conditions as we are in a frame of reference moving with the wave. The internal wave generates a pressure distribution used to solve for the seepage within the porous lake bed (grey). Note the impermeable layer under the bed (black). Behind the wave of depression, often a region of boundary layer instability will form and this is also depicted here as a superposition of three dotted ellipses.

perturbation induced by SGWs (see equation 6.1), the pressure perturbation at the lake bottom due to ISWs and internal trapped waves is large. Moreover, the pressure perturbation is steady in a frame of reference moving with the wave speed. This profile can be diagnostically determined from the solution of the DJL equation and used to drive a model of the porous layer. In practice, the solutions of the DJL equation can be computed up to some limiting amplitude. It has been shown [65] that three qualitative types of upper bounds on wave amplitude are possible. The first is the so-called breaking limit, beyond which waves would have closed streamlines. It can be thought of as the internal wave analogue of SGWs breaking on a beach. The second is the broadening limit in which waves tend to a limiting state consisting of a central region with flat isopycnals, and is sometimes referred to as the conjugate flow limit [67]. The third is the so-called stability limit, in which the gradient Richardson number of the wave induced flow dips below 0.25 and shear instability is possible in the wave [66]. In the following we will consider large ISWs and trapped waves, but well below the limiting amplitude. Oceanographic measurements of large amplitude internal waves are discussed in the recent review by [49], while in a lake context well resolved measurements of large amplitude internal waves have been reported for Lake Constance [83] throughout the stratified season. We briefly mention here that when the pycnocline is above the mid-depth, ISWs of depression will form. Similarly, when the pycnocline is below the mid-depth, ISWs of elevation form.

Trapped waves are a more recently reported phenomenon [99, 94] and can reach amplitudes larger than the limiting ISW amplitude. They require a forcing mechanism, namely a background current and topography. Mathematically, they are a steady solution and hence remain unchanged for all times. In a practical situation, their lifespan would depend on how long a suitable forcing persisted. As a rough estimate, a passing ISW could be expected to influence the pressure at the SWI for a period on the order of a half hour. In contrast, a trapped wave with an amplitude 150% of the ISW (a typical amplitude reported by [99, 94]) can persist for several hours, and would have the potential to increase across SWI transport by a factor of ten.

For trapped waves, we will assume an isolated topography, or in other words that $h(x) \to 0$ as $|x| \to \infty$. The functional form of the topography was selected to be a hyperbolic secant function (though this is largely a matter of mathematical convenience)

$$h(x) = A_o \text{ sech}\left(\frac{x}{\lambda}\right) \tag{6.7}$$

where A_0 is the height of the topography and λ specifying the width. The parameters were chosen to match those of a trapped internal wave as found in Figure 1 of [94]. A

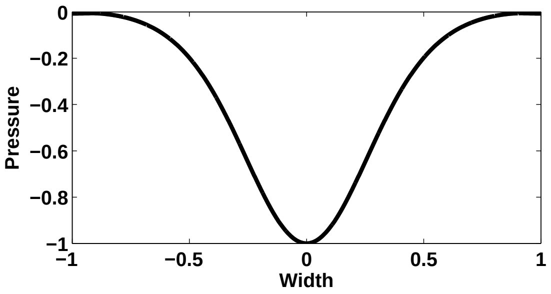

Figure 6.3: Normalized pressure profile induced by an ISW with a maximum dimensionless isopycnal displacement of 0.215 at the SWI extracted from the solution of the DJL equation in the free fluid.

number of exploratory simulations indicate that these results are generic for a broad range of parameter space. The solution of the DJL equation was found using publically available software developed in our group (see [94] and [33] for details).

We will report results in dimensionless form. Velocities will be scaled by the linear long wave speed of internal waves, spatial extent by the depth of the lake, with a second parameter for the depth of the porous lake bottom, and time by the advective time scale. Due to the linearity of the Darcy theory, the pore pressure forcing will be scaled by its maximum value.

The situation of an internal wave overlying a porous layer is schematized in Figure 6.2 (the mathematical formulation is discussed in detail below). A corresponding typical pore pressure perturbation at the SWI due to an ISW with a maximum dimensionless isopycnal displacement of 0.215 is shown in Figure 6.3 in a frame moving with the wave speed.

6.2.2 Equations and numerical methods for the porous medium

We assume throughout that the solid matrix of the porous medium is rigid. We further assume that the pore space is saturated. Under these assumptions, Darcy's law provides a relation between the pore pressure gradient within the porous medium and the seepage rate which is in good agreement with experiment [84, 87]

$$\vec{w} = -\frac{k}{\mu}\vec{\nabla}(P + \Pi) \tag{6.8}$$

where $\vec{w}$ is the seepage rate (in general defined as the relative velocity of the pore fluid with respect to the solid matrix multiplied by the pore fraction), k is the permeability (m^2), μ is the dynamic viscosity (Pa·s) (assumed constant for a given fluid), P is the pressure (Pa), and Π is the gravitational potential energy per unit volume ($\mathrm{kg/m/s^2}$). Note that k was previously used to denote the wavenumber, as is standard, though the use of k to denote permeability is standard as well and should be clear from context. We define

$$P' = P + \Pi$$

to be the gauge pressure. We drop the prime for the remainder of this paper for simplicity.

Darcy's law, in conjunction with the conservation of mass for an incompressible fluid yields the condition

$$-\vec{\nabla} \cdot \left(\frac{k}{\mu} \vec{\nabla} P \right) = 0. \tag{6.9}$$

If the permeability is constant throughout the porous medium, the problem reduces to a potential problem (i.e. a solution of Laplace's equation) for pressure. We can non-dimensionalize the problem by introducing characteristic scaling factors for pressure, length, height and permeability (P_0, L, δ, k_0) so that

$$\tilde{P} = \frac{P}{P_0} \qquad \tilde{x} = \frac{x}{L} \qquad \tilde{z} = \frac{z}{\delta} \qquad \tilde{k} = \frac{k}{k_0}$$

Using these dimensionless variables, we can rewrite the problem as

$$\alpha \left[\partial_{\tilde{x}} \left(\tilde{k} \partial_{\tilde{x}} \tilde{P} \right) + R^2 \partial_{\tilde{z}} \left(\tilde{k} \partial_{\tilde{z}} \tilde{P} \right) \right] = 0 \tag{6.10}$$

where

$$\alpha = \frac{P_0 k_0}{\mu L^2} \qquad R = \frac{L}{\delta}$$

Hence, the geometric distribution of seepage will only depend on the parameter R and the functional form of the permeability. R gives the ratio of the typical horizontal scale, set by the pressure perturbation at the SWI, to the depth of the porous layer. The exact value of R would be determined in practice from field observations. We will henceforth drop the tildes for simplicity. We estimate the value of α to be around 1×10^{-13} for lake scales, but this will vary significantly depending on the case. Note that the small value of α is largely controlled by the small value of permeability. See [89] for an example of parameter values.

The linear elliptic equation (6.10) for the pore pressure must be supplemented by appropriate boundary conditions. We assume no flow in the porous medium far upstream and downstream. We also assume that an impermeable layer (due to the presence of clay, for example) is found at a depth $z = -1$. Finally, we assume that the pore pressure at the SWI, $P_0(x)$, is continuous, and hence specified by the fluid pressure (which may be recovered *a posteriori* from the solution of the DJL). The assumption that the lake bottom is a streamline for the free fluid flow is justified since the speed of the flow into the porous medium will be many orders of magnitude lower than the typical speed in the free fluid, as discussed in the introduction. The complete boundary value problem is solved on the domain for which $-1 \leq x \leq 1$ and $-1 \leq z \leq h(x)$. Mathematically, the boundary conditions can be written as

$$\left.\frac{\partial P}{\partial x}\right|_{x=\pm 1} = 0 \qquad \left.P\right|_{z=h(x)} = P_0(x) \qquad \left.\frac{\partial P}{\partial z}\right|_{z=-1} = 0$$

and the situation is schematized in Figure 6.2.

In the case of unsteady flow in the porous medium the situation is more ambiguous. Many authors (see [22] and references therein) drop the acceleration terms in the momentum equations for the porous medium and hence assume that the instantaneous flow is governed by Darcy's law. This is done even in problems of convection in porous medium which can be expected to involve considerably more vigorous motion in the domain than those we discuss below. We thus follow [22] and assume that even in the unsteady case we can switch to a frame moving with the solitary wave and maintain an elliptic problem for pressure and Darcy's law for velocity, leaving a more critical examination of these assumptions to future work.

The numerical solutions presented in the following were found using a Fourier-Chebyshev pseudospectral method in x and z, as described by Trefethen [103]. This method achieves optimal order given a number of grid points. In practice, for smooth problems accuracy nearing machine precision can be achieved, even with a modest number of grid points. The non-rectangular geometry was handled via two methods: an embedding method based on a technique for mountain wave computations [69] in the atmosphere and a mapping method (as employed by [94] for the internal wave problem). Both methods were found to be accurate, but the embedding method yielded a discretized system whose linear algebra properties allowed for a much faster solution. The embedding method was thus used for all computations presented with the mapping method used to confirm the validity of the results.

6.2.3 Permeability Distributions

Lake bottoms are composed of a large variety of compounds, each with their own characteristic physical properties [61]. Often these settle into stratified layers, with each layer having its own characteristic permeability. We considered a variety of physically motivated situations. The first case, to which all others will be compared is the case where $R = 25$ (height is 4% of the width). Following this, we will provide a sensitivity analysis by varying the parameter R. Finally, we will consider the effect of the permeability stratification where the permeability sharply increases/decreases within the domain. Here the permeability function was taken to be a hyperbolic tangent function centered at 50% of the total depth of the porous layer with a transition region over 10% of the total depth. Mathematically this permeability profile can be written as,

$$k_{\text{Inc}} = 1 + \frac{1}{2}\left(1 + \tanh\left[\frac{z - 0.5}{0.1}\right]\right) \tag{6.11}$$

$$k_{\text{Dec}} = 2 - \frac{1}{2}\left(1 + \tanh\left[\frac{z - 0.5}{0.1}\right]\right) \tag{6.12}$$

for increasing and decreasing permeability respectively.

In addition to the work on internal wave driven seepage, we propose a mechanism by which the finite amplitude internal wave increases the near surface permeability. The basic idea is that an internal solitary wave, or trapped wave, can induce instabilities in the bottom boundary layer and thereby enhance benthic turbulence (see [32, 98] for detailed discussion of this phenomenon). This turbulence lifts the small pieces of detritus that clog the near surface pores. Based on this, a mathematical formula for the internal wave modified permeability is proposed,

$$k = 1 + \frac{10}{2}\left[1 + \tanh\left(\frac{x + 0.05}{0.1}\right)\right]\exp\left(\frac{z + 1}{0.3}\right). \tag{6.13}$$

While this permeability function might appear complex, Figure 6.12[a] shows its rather simple geometric form.

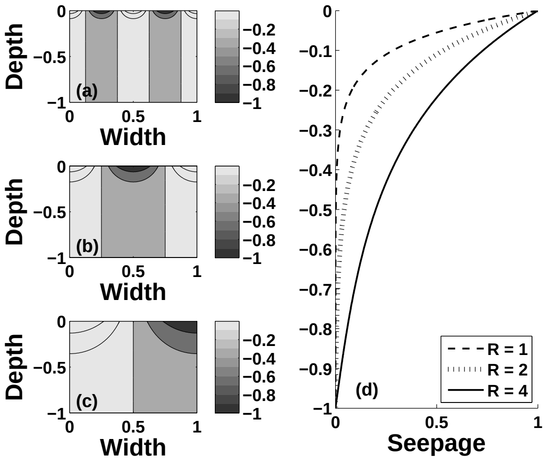

Figure 6.4: Normalized pressure distributions as a result of sinusoidal pressure waves of wavelengths (a) $R = 1$, (b) $R = 2$, and (c) $R = 4$ at the SWI. The seepage profiles at x=0 are plotted in (d). Note that longer wavelengths penetrate deeper into the porous medium.

6.3 Results

6.3.1 Exploratory cases

As mentioned in the Introduction, [106] have demonstrated that convection is insufficient to explain the observed seepage through the porous layer found at the bottom of lakes. It is thus sensible to argue, and indeed the Introduction discusses several examples from the literature, that this seepage is, at least in part, a result of gravity wave-induced flow through the lake bottom [106]. However, in lakes deeper than a few meters, the pressure profiles of surface waves are weak (see equation 6.1). As such, seepage in fresh water lakes that is induced by surface water waves is constrained to shallow regions near the coast [18]. Moreover, even when the depth is small enough so that they could influence the bottom pressure, surface waves have a short wavelength, move quickly and generally do not retain the identity of individual wave crests for long times. The importance of the horizontal scale of the pressure profile that forces flow in the porous medium is easy to see in the limiting case of a very deep, porous lake bed forced by a sinusoidal pressure profile. For this case, the pressure in the porous medium is given by

$$P = \exp\left[\ell z\right] \sin \ell x.$$

The pressure, and hence the seepage, decays exponentially within the porous layer at a rate given by the wavenumber, ℓ. Thus we see that disturbances induced by short wavelengths (large wavenumber) decay quickly. Since internal waves typically exhibit length scales that are in the tens of meters, we thus see that pressure fluctuations due to internal waves will be able to penetrate into thicker lake bottoms than their surface water counterparts. The vertical component of the seepage is given from Darcy's law as

$$W_z = \frac{k}{\mu} \ell \exp\left[\ell z\right] \sin \ell x.$$

and this implies that the magnitude of seepage at the SWI decreases with wavelength.

Figure 6.4 demonstrates the same effect for the more realistic case of an impermeable layer at the base of the porous layer. Panels (a), (b), (c) output the pressure distributions as a result of sinusoidal pressure profiles at the SWI with $R = 1$, 2, 4 respectively. In panel (d), the normalized seepage profiles taken along the line $x = 0$ are given. It can be seen that again, the seepage due to short wavelength perturbations does not penetrate deep into the porous layer while longer wavelengths drive significant seepage at greater depths.

Wörman *et al.* [107] argue that in their three dimensional simulation, seepage decays with wavelength even faster with depth than similar two dimensional simulations. However, as internal waves tend to maintain their across-lake structure (M. Preusse private communication) over very long length scales (certainly far longer than the wave length) three dimensional structure is presumed to play a rather weak role.

Figure 6.5 considers a sinusoidal perturbation with $R = 10$. The pressure perturbation is shown in panel (a), while the magnitude of the seepage with superimposed arrows indicating the direction of flow is shown in panel (b). It can be seen that the regions of large magnitude of seepage are concentrated near the maximum and minimum of the pressure profile gradient. Note that over the majority of the domain, the seepage is nearly horizontal.

Elliot and Brooks [34] have discussed a similar phenomenon, demonstrating that the mass transfer within the porous medium is proportional to the magnitude of the pressure perturbation and inversely proportional to the wavelength of the gravity wave. Their analysis is unchanged for internal waves. Both analyses thus suggest that the large wavelength

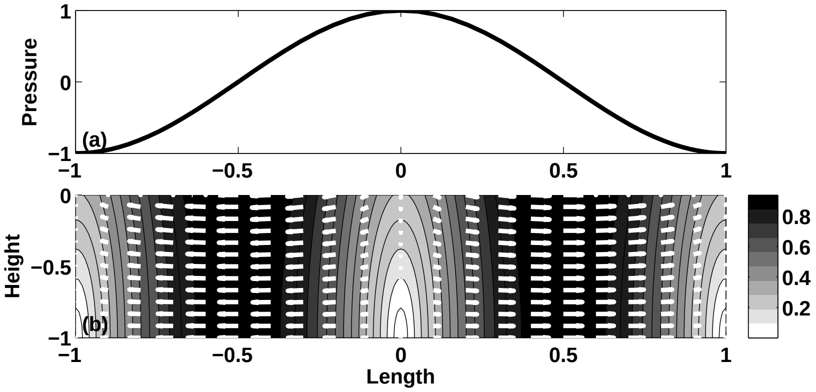

Figure 6.5: (a) Normalized pressure profile at the SWI, (b) Magnitude of the normalized seepage through the porous medium (shaded). Arrows denote the direction of the seepage. R = 10.

of an internal gravity wave will induce less seepage at the SWI than a shorter wavelength wave of equal magnitude. However, the induced seepage of large wavelength internal waves will penetrate deeper into the porous medium, thereby making available nutrients previously inaccessible to the main water column. Moreover, since in water depth greater than a few meters surface gravity wave-induced pressure perturbations are negligible, internal waves greatly expand the geographic area over which significant seepage can take place.

6.3.2 Internal Solitary Waves

In a frame of reference frame moving with a single solitary wave (or one wave in the wave-train schematized in Figure 1), we can use the DJL equation to compute a pressure profile at the SWI (see Figure 6.3) and thereby compute the seepage induced through the bottom porous layer. While both Salehin *et al.* [87] and Sawyer and Cardenas [89] have demonstrated that the distribution of small scale inhomogeneity induced by bed forms (e.g. ripples) can have a significant impact on the fluid residence time within the lake bed (at least on sub-meter scales), here we are interested primarily in motions induced by a long length scale internal solitary wave. We thus concentrate on a flat bottomed lake and three characteristic permeability distributions that vary with depth only. We discuss the constant permeability case first, follow this with a discussion of the influence of changing the porous layer thickness parameter R, and finally discuss the influence of permeability

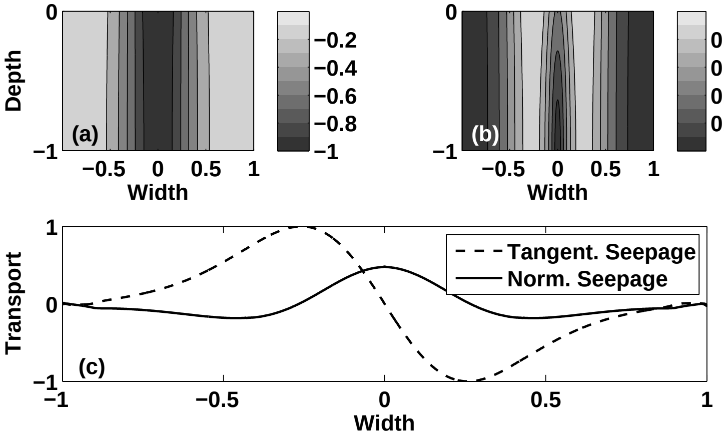

Figure 6.6: Computed pressure (a), seepage magnitude (b) and seepage profiles along the SWI (c) computed with a constant permeability throughout. Seepage profiles have been normalized by the maximum seepage within the domain and hence dimensionless values are presented here. R = 25. Here tangential seepage corresponds to along SWI transport and normal seepage corresponds to across SWI transport.

stratification within the domain.

Case 1 - Constant K

In Figure 6.6 we show the pore pressure (panel a), seepage rate magnitude (panel b), and transport across and along the SWI for the case of constant permeability within a porous layer with $R = 25$. Panels (a) and (b) show that both the pore pressure and seepage rate magnitude distributions are symmetric across the wave crest. From panel (c) we can see that the wave induces both along and across SWI transport. The across SWI transport is roughly three quarters of the magnitude of the along SWI transport and consists of a region of out-flux near the wave crest and a broader region of influx on the flanks of the wave.

We see that the ISW is acting essentially as a "vacuum cleaner", drawing fluid up through the SWI near the wave crest. As the porous layer in this case is shallow, we see that fluid is pulled right from the bottom of the porous layer, filtering through regions which pressure pulses due to surface gravity waves would not be able to penetrate.

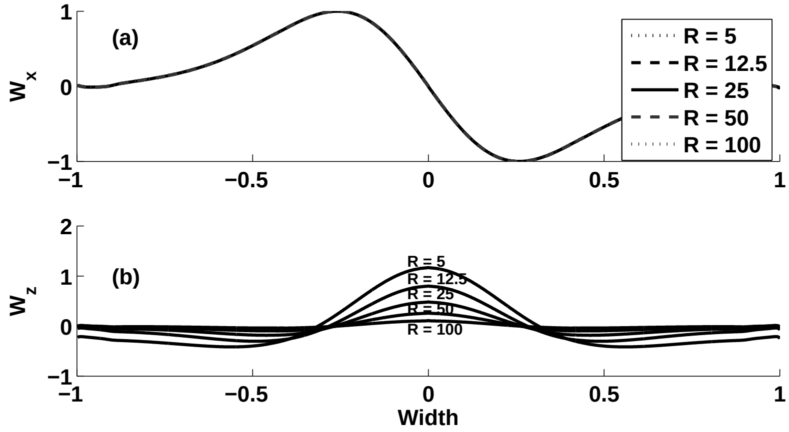

Figure 6.7: Computed tangential; note that the curves are essentially indistinguishable (a) and normal (b) seepage rates at the SWI for varying values of R. Profiles were normalized to the maximum value of seepage of R=25.

Case 2 - R Sensitivity

The seepage throughout the porous domain is controlled by the dimensionless parameter R. As previously defined, R denotes the ratio of width scale of the porous layer to the height. Figure 6.7 compares the tangential (a) and normal (b) fluid velocities at the SWI and its sensitivity to the parameter R, normalized by the maximum seepage when $R = 25$. Notice that the tangential velocity at the SWI is invariant under the value of R, while the normal seepage grows drastically as the depth of the domain is increased (while the profile of the pressure perturbation remains fixed). This result is perhaps the clearest indication that the long wavelengths characteristic of the ISW can penetrate deep into the domain and thereby boost the fluid exchange between the porous layer and the water column.

Further sensitivity analysis (not shown) demonstrates that with the same pressure perturbation used here, values of R lower than 2.5 yield essentially no further increase in normal seepage. Thus we see that the most substantial increase in seepage rates occurs when the R value is well below 1.

Case 3 - Permeability Stratification

The porous layers on lake bottoms are often stratified into layers, thereby varying permeability in the z direction. As defined above in equations (6.11) and (6.12), we allow the permeability to double or halve over the domain. Figure 6.8 plots the seepage throughout the domain as a result of the permeability stratification. Both the seepage distributions (a), (d) and profiles along the SWI (b), (e) are shown.

What we find is that the permeability stratification effectively constrains the thickness of the porous layer. When the permeability decreases (panels (a)-(c)) by a factor of two with depth, the seepage is constrained within the upper, more permeable portion of the porous domain, and hence R is effectively doubled. The opposite effect can be noticed when the permeability is doubled with depth (panels (d)-(f)). In this case the seepage is largely found within the bottom, more permeable half of the porous layer. Notice that there is a four-fold difference in seepage at the SWI between the two profiles, with the less permeable upper layer exhibiting lower values. The shape of the normal and tangential seepage profiles at the SWI, as well as their relative proportion, remain identical. These results are consistent with those found by Zlotnik *et al.* [108] who demonstrated that a decreasing permeability distribution resulted in a decrease in the SWI seepage but had an increase in the seepage at greater depths.

6.3.3 Trapped internal waves and bottom boundary layer interaction

The presence of a “trough” topography, for example due to a drowned creek bed, allows for a trapped wave to form. Using an isolated topography, with the mathematical form given by (6.7), and solving the DJL equation, we compute the pressure along the SWI and use this pressure profile to drive seepage in the porous medium. Note that the domain is non-rectangular and this requires some care in the construction of the numerical method, as described above. Figure 6.9 plots the resultant distributions of pressure (a), seepage (b) and the profiles of seepage along and across the SWI (c). Interestingly, the profile of the across SWI seepage has become bimodal about the origin, with the seepage reduced near the center of the domain. Moreover, as the topography effectively decreases the depth of the porous domain, the ratio between normal and tangential seepage decreases near the domain center. That is, the normal seepage appears to decrease in relation to tangential seepage. However, as trapped waves can reach amplitudes much greater than propagating waves, the total seepage will be significantly larger than that presented above for propagating waves.

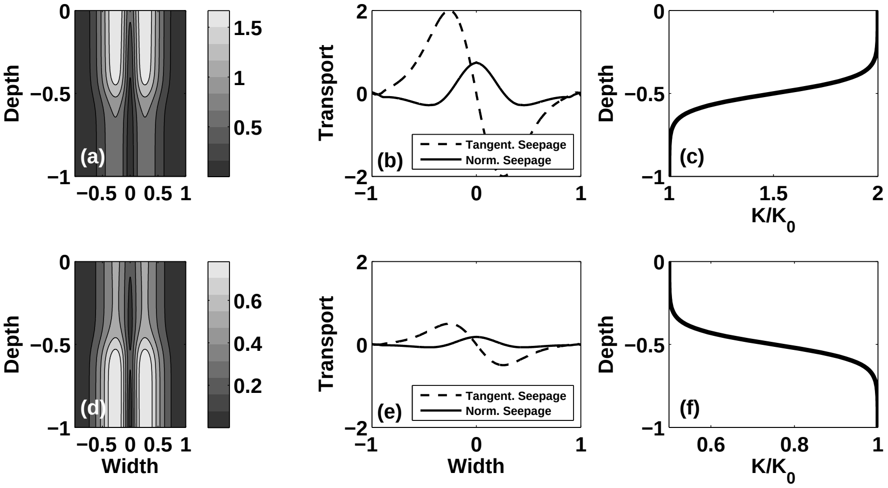

Figure 6.8: Computed seepage (a,d) and seepage profiles along the SWI (c,e) computed with a permeability stratification centered at fifty percent of the depth of the porous layer (c,f). Permeability decreases with depth (top) and increases (bottom) by a factor of two. Seepage profiles have been normalized by the maximum seepage within the constant permeability domain. R = 25.

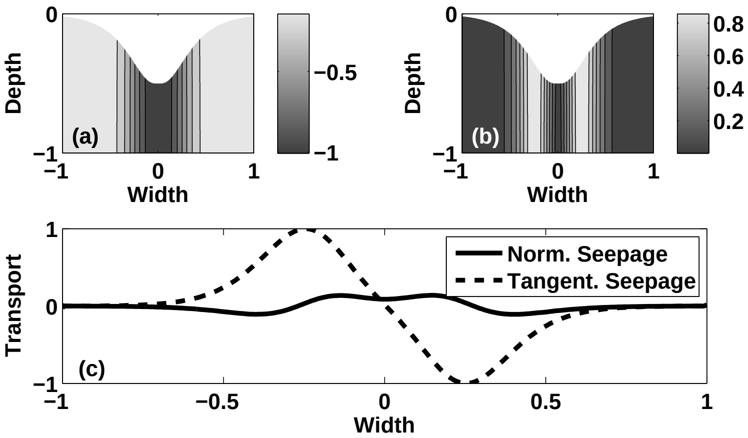

Figure 6.9: Computed pressure (a), seepage magnitude (b) and seepage profiles along the SWI (c) computed with a constant permeability throughout. Topography was chosen to be a sech function for simplicity. Seepage profiles have been normalized to the maximum seepage within the flat topography domain. Dimensionless values are presented here. R = 25.

The interaction of internal solitary waves (ISW) with the bottom boundary layer has been discussed extensively in the literature from numerical [98, 16, 32], experimental [23], and observational [15] points of view. The general picture that has emerged from these studies is that while waves of elevation require the presence of an upstream current (such as the barotropic tide, or lake-scale seiche) in order to yield a global instability and enhanced benthic turbulence in the bottom boundary layer, waves of depression can yield global instabilities in the boundary layer due to the adverse pressure gradient induced by the wave. However, the instabilities due to the waves of elevation are generally more vigorous. In the context of trapped waves this propensity for instability is strengthened by the curvature of the bottom boundary that can, in itself, induce separation and boundary layer instability [92].

The presence of turbulence in the boundary layer precludes the possibility of a steady state so we have performed several time-dependent simulations in order to demonstrate the development of a highly-turbulent boundary layer. The simulations were completed with a pseduo-spectral code [101]. The two dimensional simulations were performed at a Reynolds number based on upstream velocity, total depth, and the viscosity of water, of roughly 3×10^5, well into the transitional regime. In Figure 6.10, we show normalized

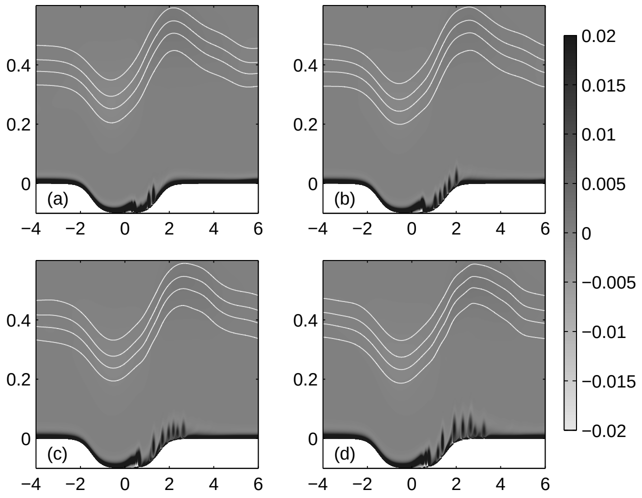

Figure 6.10: Evolution of the normalized vorticity within the water column as a result of the currents induced by the trapped wave. The four non-dimensional times are (a) 11.2, (b) 12.6, (c) 14, and (d) 15.4. Notice the generation of a turbulent region in the boundary layer in the downstream portion of the topography. Four isopycnal lines have been plotted to show the wave form.

vorticity at four non-dimensional times $t_* = 11.2, 12.6, 14, 15.4$. The time has been non-dimensionalized by the background flow and column depth so that $t_* = \frac{tU_0}{H}$. Within the bottom boundary layer, instability leading to turbulence develops in the downstream portion of the topography. This will, in turn, lead to pickup of the smaller particulate matter at the surface of the underlying porous layer. At later times the turbulent region has expanded well downstream of the topography. This process is elaborated further in plots of the bottom stress, Figure 6.11. The grey lines indicate values of ±500% of the stress induced by the current upstream. In a large portion of the downstream half of the domain, the bottom stress exceeds a factor of five times the upstream value for at least a portion of the time. The spikes in the bottom stress shown can thus lead to pickup of particulate matter, with vortex induced currents transporting material up into the water column and away from the SWI.

In order to model the effect of boundary layer instability and bottom stress induced pore unclogging, we reconsider the problem whose solution is shown in Figure 6.9, but with a modified permeability distribution with the form given above (equation 6.13). In Figure 6.12 we compare the results for the trapped internal wave modified permeability

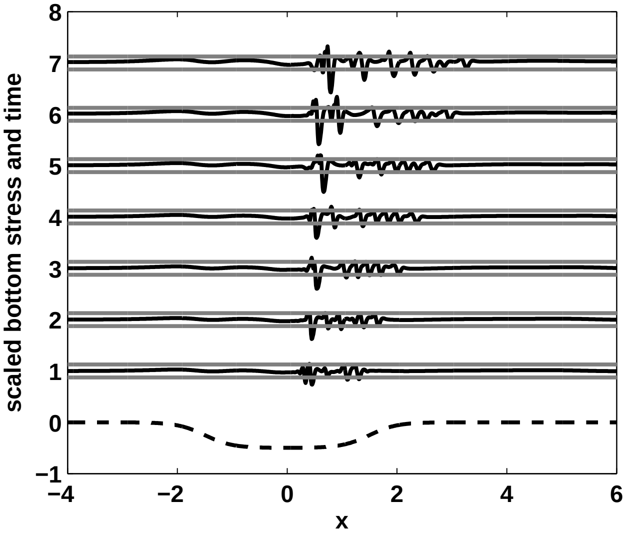

Figure 6.11: Evolution of the scaled bottom stress after onset of instability in the boundary layer. The vertical axis marks snapshots at different times. The curves at 1, 3, 5, and 7 correspond to panels (a), (b), (c), and (d) in Figure 6.10. The gray lines represent a deviation of ±500% from the stress induced by the current upstream of the wave. Bottom dashed curve plots the topography.

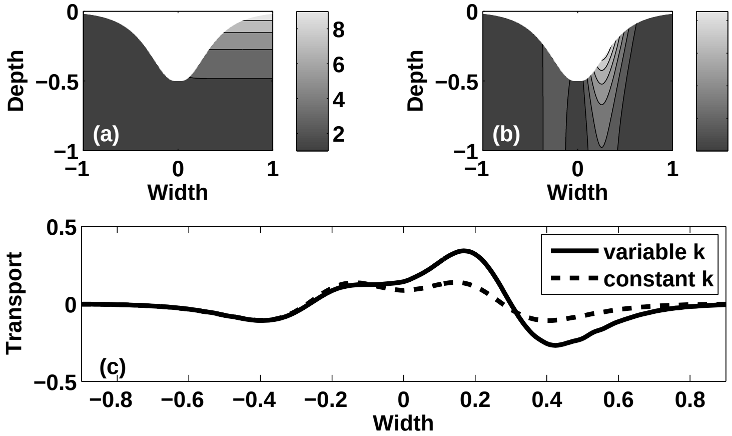

Figure 6.12: Comparison of turbulence modified permeability with the constant permeability case. (a) Six shaded equally spaced contours of the normalized permeability, (b) Six shaded equally spaced contours of the magnitude of the seepage rate, scaled by its largest value, (c) transport across the SWI for the wave modified permeability (solid) and constant permeability (dashed) cases. R = 25.

profile, with those of the constant permeability case (as shown in Figure 6.9). Panel (a) shows six contours of the permeability distribution, panel (b) shows six contours of the magnitude of the seepage rate and panel (c) compares across SWI transport between the modified and constant permeability cases (both are scaled by the maximum seepage rate of the constant case). It can be clearly seen that the wave induced boundary layer instability, as expressed by the modified permeability, substantially increases the seepage through the porous domain.

6.4 Discussion and Conclusion

The analysis of the nutrient circulation system in oligotrophic lakes is an area of continuing research [80]. At the same time, field experiments that identify the incidence of high frequency, large amplitude internal waves continue to be carried out and to provide insight into their wave structure, amplitude, and seasonality [83], [59, ch. 2]. The main point of the modelling work presented above was to demonstrate that there is a significant link between the nutrient circulation system and internal waves. To date, there exists very little work in the literature concerning this coupling.

In order to demonstrate the coupling between internal waves and seepage through a porous bottom layer, we have employed solutions of the Dubreil-Jacotin-Long equation to drive seepage in a porous medium. These waves are exact solutions of the full stratified Euler equations and thus provide the best possible representation of large amplitude internal waves. The porous medium was assumed to be governed by Darcy's law. Numerical solutions were obtained using highly accurate Fourier-Chebyshev pseudo-spectral methods. Unlike previous numerical results, [50, 76] these methods included both large scale (tens of meters) topography and inhomogeneous permeability. While the formation of internal waves from the steepening of internal seiches is a generic phenomenon that is largely independent of lake topography, this topography is crucial in allowing the formation of the trapped waves, and in modifying the wave-induced pressure perturbations that drive flow across the SWI. We briefly mention that the importance of topography has also been mentioned in the literature, where Shum [93] demonstrates how the concentration of nutrients within the lake bed can be substantially influenced by the bottom topography. Similarly, [107] also demonstrate how complex topography can lead to stagnant regions within the porous domain.

In terms of a simplified, or "cartoon" picture, the internal wave acts essentially as a vacuum cleaner, with fluid drawn out of the porous medium under the internal wave peak where wave induced pressure is lowest (for internal waves of depression) and returned in the broad regions found along the flanks of the solitary waves. While observed in a different context, this prediction is similar to the observations found in [58]. The extent of the seepage can be understood in terms of the parameter $R = L/\delta$, which gives the ratio between the horizontal scale of the pressure perturbation and the vertical extent of the porous layer. For $R > 1$, the typical wavelengths of the prescribed pressure profile are larger than the porous layer depth. In this parameter regime we found that the seepage through the porous domain increased with increasing R due to the fact that the long wavelengths associated with the internal waves penetrate deeper into the porous medium.

Finally, we proposed, and provided numerical evidence for a mechanism by which the finite amplitude wave increases the near surface permeability. The basic idea is that, in agreement with theoretical and experimental studies in the literature, the wave induces instabilities in the bottom boundary layer and thus enhances benthic turbulence. This turbulence lifts the small pieces of detritus that clog the near surface pores. An idealized permeability distribution was created to encapsulate this scenario and led to both an increase in across SWI transport and a shift of its maximum downstream of the wave crest. This suggests that in conjunction with the pressure perturbation induced by either traveling or trapped waves, instabilities in the bottom boundary layer can augment the seepage through the bottom porous layer and further enhance chemical exchange with the porous layer. A discussion of the effect of turbulence on the vertical solute transfer can be found in [51].

Future work should consider several extensions of the above work. First of all, multiscale simulations that couple the large scale pressure profiles due to internal solitary waves to the small scale bed forms discussed in past literature ([87, 89, 58]) should be carried out. Second of all, for cases in which a less permeable layer overlies a more permeable layer, the question of possible ducting by regions of lower permeability should be explored. Finally, more complete formulations of the equations governing the flow in the porous medium, e.g. Brinkman terms, should be explored.

The present paper presents the potential importance of internal waves on the nutrient circulation systems in lakes. Our hope is that this paper will encourage both experimentalists and theoreticians to consider the substantial impact that internal solitary waves can have on lake-bed dynamics and their impact on the biosphere.

Acknowledgements: This work was funded by the Natural Sciences and Engineering Research Council of Canada. Christopher Subich provided extensive help with the numerical methods used.

Chapter 7

Conclusion

This thesis discusses three mechanisms by which internal waves effect the nutrient circulation system. We have demonstrated that

- Internal waves can induce significant resuspension in lakes and oceans.
- Internal waves induced vortices found in fluid mud may amplify this resuspension.
- Internal waves induce significant seepage through porous layers found at the bottom of lakes and oceans.

While this is not a comprehensive list of the internal waves effects on lake and ocean dynamics, the above list does highlight that internal waves are significant in specific domains. In reference to figure 1 in Chapter 1, we see that this thesis has systematically analyzed each of the various domains presented.

One issue we have largely ignored in this model, however, is a coupling between the various parts of the water-mud-porous layer system, or more to the point coupling of the individual mathematical models. As mentioned in chapter 6, the coupling between such regions can be quite complex. This is a direct avenue for future research, with the ultimate goal of developing a complete model to simultaneously simulate the various domains of interest.

Internal waves have been observed in both lake and oceans settings[49, 41]. As they are so common, they should have some impact on how nutrients are distributed within the water column [2, 97]. Here we have demonstrated how internal waves can effect the fluid flow over large variations in scale. Internal waves themselves can be on the scale of tens of meters and they can effect change in the micrometer pore spacings found in lake bottoms. The influence of internal waves on such a large range of scales is indicative of their fundamental importance to lake and ocean nutrient modelling. This thesis is presented in support of this hypothesis.

Copyright Permission

JOHN WILEY AND SONS LICENSE
TERMS AND CONDITIONS

Apr 18, 2013

This is a License Agreement between Jason Olsthoorn ("You") and John Wiley and Sons ("John Wiley and Sons") provided by Copyright Clearance Center ("CCC"). The license consists of your order details, the terms and conditions provided by John Wiley and Sons, and the payment terms and conditions.

All payments must be made in full to CCC. For payment instructions, please see information listed at the bottom of this form.

License Number	3080231187557
License date	Feb 01, 2013
Licensed content publisher	John Wiley and Sons
Licensed content publication	Water Resources Research
Licensed content title	Fluid circulation and seepage in lake sediment due to propagating and trapped internal waves
Licensed copyright line	©2012. American Geophysical Union. All Rights Reserved.
Licensed content author	Jason Olsthoorn,Marek Stastna,Nancy Soontiens
Licensed content date	Nov 15, 2012
Start page	n/a
End page	n/a
Type of use	I don't see my intended use
Special requirements	Good Afternoon, My name is Jason Olsthoorn, and I recently published the above article in Water Resources Research. I would like to use the content of this article in my thesis which I am in the process of writing and would like to have permission to use this paper. Any information you can provide would be much appreciated. Thank you very much, Jason Olsthoorn Master's Student University of Waterloo, ON, Canada
Total	**0.00 USD**

Terms and Conditions

TERMS AND CONDITIONS

This copyrighted material is owned by or exclusively licensed to John Wiley & Sons, Inc. or one of its group companies (each a "Wiley Company") or a society for whom a Wiley Company has exclusive publishing rights in relation to a particular journal (collectively WILEY"). By clicking "accept" in connection with completing this licensing transaction, you agree that the following terms and conditions apply to this transaction (along with the billing and payment terms and conditions established by the Copyright Clearance Center Inc., ("CCC's Billing and Payment terms and conditions"), at the time that you opened your Rightslink account (these are available at any time at http://myaccount.copyright.com)

Terms and Conditions

1. The materials you have requested permission to reproduce (the "Materials") are protected by copyright.

2. You are hereby granted a personal, non-exclusive, non-sublicensable, non-transferable, worldwide, limited license to reproduce the Materials for the purpose specified in the licensing process. This license is for a one-time use only with a maximum distribution equal to the number that you identified in the licensing process. Any form of republication granted by this licence must be completed within two years of the date of the grant of this licence (although copies prepared before may be distributed thereafter). The Materials shall not be used in any other manner or for any other purpose.

Permission is granted subject to an appropriate acknowledgement given to the author, title of the material/book/journal and the publisher. You shall also duplicate the copyright notice that appears in the Wiley publication in your use of the Material. Permission is also granted on the understanding that nowhere in the text is a previously published source acknowledged for all or part of this Material. Any third party material is expressly excluded from this permission.

3. With respect to the Materials, all rights are reserved. Except as expressly granted by the terms of the license, no part of the Materials may be copied, modified, adapted (except for minor reformatting required by the new Publication), translated, reproduced, transferred or distributed, in any form or by any means, and no derivative works may be made based on the Materials without the prior permission of the respective copyright owner. You may not alter, remove or suppress in any manner any copyright, trademark or other notices displayed by the Materials. You may not license, rent, sell, loan, lease, pledge, offer as security, transfer or assign the Materials, or any of the rights granted to you hereunder to any other person.

4. The Materials and all of the intellectual property rights therein shall at all times remain the exclusive property of John Wiley & Sons Inc or one of its related companies (WILEY) or their respective licensors, and your interest therein is only that of having possession of and the right to reproduce the Materials pursuant to Section 2 herein during the continuance of this Agreement. You agree that you own no right, title or interest in or to the Materials or any of the intellectual property rights therein. You shall have no rights hereunder other than the license as provided for above in Section 2. No right, license or interest to any trademark, trade name, service mark or other branding ("Marks") of WILEY or its licensors is granted hereunder, and you agree that you shall not assert any such right, license or interest with respect thereto.

5. NEITHER WILEY NOR ITS LICENSORS MAKES ANY WARRANTY OR REPRESENTATION OF ANY KIND TO YOU OR ANY THIRD PARTY, EXPRESS, IMPLIED OR STATUTORY, WITH RESPECT TO THE MATERIALS OR THE ACCURACY OF ANY INFORMATION CONTAINED IN THE MATERIALS, INCLUDING, WITHOUT LIMITATION, ANY IMPLIED WARRANTY OF MERCHANTABILITY, ACCURACY, SATISFACTORY QUALITY, FITNESS FOR A PARTICULAR PURPOSE, USABILITY, INTEGRATION OR NON-INFRINGEMENT AND ALL SUCH WARRANTIES ARE HEREBY EXCLUDED BY WILEY AND ITS LICENSORS AND WAIVED BY YOU.

6. WILEY shall have the right to terminate this Agreement immediately upon breach of this Agreement by you.

7. You shall indemnify, defend and hold harmless WILEY, its Licensors and their respective directors, officers, agents and employees, from and against any actual or threatened claims, demands, causes of action or proceedings arising from any breach of this Agreement by you.

8. IN NO EVENT SHALL WILEY OR ITS LICENSORS BE LIABLE TO YOU OR ANY OTHER PARTY OR ANY OTHER PERSON OR ENTITY FOR ANY SPECIAL, CONSEQUENTIAL, INCIDENTAL, INDIRECT, EXEMPLARY OR PUNITIVE DAMAGES, HOWEVER CAUSED, ARISING OUT OF OR IN CONNECTION WITH THE DOWNLOADING, PROVISIONING, VIEWING OR USE OF THE MATERIALS REGARDLESS OF THE FORM OF ACTION, WHETHER FOR BREACH OF CONTRACT, BREACH OF WARRANTY, TORT, NEGLIGENCE, INFRINGEMENT OR OTHERWISE (INCLUDING, WITHOUT LIMITATION, DAMAGES BASED ON LOSS OF PROFITS, DATA, FILES, USE, BUSINESS OPPORTUNITY OR CLAIMS OF THIRD PARTIES), AND WHETHER OR NOT THE PARTY HAS BEEN ADVISED OF THE POSSIBILITY OF SUCH DAMAGES. THIS LIMITATION SHALL APPLY NOTWITHSTANDING ANY FAILURE OF ESSENTIAL PURPOSE OF ANY LIMITED REMEDY PROVIDED HEREIN.

9. Should any provision of this Agreement be held by a court of competent jurisdiction to be illegal, invalid, or unenforceable, that provision shall be deemed amended to achieve as nearly as possible the same economic effect as the original provision, and the legality, validity and enforceability of the remaining provisions of this Agreement shall not be affected or impaired thereby.

10. The failure of either party to enforce any term or condition of this Agreement shall not constitute a waiver of either party's right to enforce each and every term and condition of this Agreement. No breach under this agreement shall be deemed waived or excused by either party unless such waiver or consent is in writing signed by the party granting such waiver or consent. The waiver by or consent of a party to a breach of any provision of this Agreement shall not operate or be construed as a waiver of or consent to any other or subsequent breach by such other party.

11. This Agreement may not be assigned (including by operation of law or otherwise) by you without WILEY's prior written consent.

12. Any fee required for this permission shall be non-refundable after thirty (30) days from receipt.

13. These terms and conditions together with CCC's Billing and Payment terms and conditions (which are incorporated herein) form the entire agreement between you and WILEY concerning this licensing transaction and (in the absence of fraud) supersedes all prior agreements and representations of the parties, oral or written. This Agreement may not be amended except in writing signed by both parties. This Agreement shall be binding upon and inure to the benefit of the parties' successors, legal representatives, and authorized assigns.

14. In the event of any conflict between your obligations established by these terms and conditions and those established by CCC's Billing and Payment terms and conditions, these terms and conditions shall prevail.

15. WILEY expressly reserves all rights not specifically granted in the combination of (i) the license details provided by you and accepted in the course of this licensing transaction, (ii) these terms and conditions and (iii) CCC's Billing and Payment terms and conditions.

16. This Agreement will be void if the Type of Use, Format, Circulation, or Requestor Type was misrepresented during the licensing process.

17. This Agreement shall be governed by and construed in accordance with the laws of the State of New York, USA, without regards to such state's conflict of law rules. Any legal action, suit or proceeding arising out of or relating to these Terms and Conditions or the breach thereof shall be instituted in a court of competent jurisdiction in New York County in the State of New York in the United States of America and each party hereby consents and submits to the personal jurisdiction of such court, waives any objection to venue in such court and consents to service of process by registered or certified mail, return receipt requested, at the last known address of such party.

Wiley Open Access Terms and Conditions

All research articles published in Wiley Open Access journals are fully open access: immediately freely available to read, download and share. Articles are published under the terms of the Creative Commons Attribution Non Commercial License. which permits use, distribution and reproduction in any medium, provided the original work is properly cited and is not used for commercial purposes. The license is subject to the Wiley Open Access terms and conditions:
Wiley Open Access articles are protected by copyright and are posted to repositories and websites in accordance with the terms of the Creative Commons Attribution Non Commercial License. At the time of deposit, Wiley Open Access articles include all changes made during peer review, copyediting, and publishing. Repositories and websites that host the article are responsible for incorporating any publisher-supplied amendments or retractions issued subsequently.
Wiley Open Access articles are also available without charge on Wiley's publishing platform, **Wiley Online Library** or any successor sites.

Use by non-commercial users

For non-commercial and non-promotional purposes individual users may access, download, copy, display and redistribute to colleagues Wiley Open Access articles, as well as adapt, translate, text- and data-mine the content subject to the following conditions:

- The authors' moral rights are not compromised. These rights include the right of "paternity" (also known as "attribution" - the right for the author to be identified as such) and "integrity" (the right for the author not to have the work altered in such a way that the author's reputation or integrity may be impugned).
- Where content in the article is identified as belonging to a third party, it is the obligation of the user to ensure that any reuse complies with the copyright policies of the owner of that content.
- If article content is copied, downloaded or otherwise reused for non-commercial research and education purposes, a link to the appropriate bibliographic citation (authors, journal, article title, volume, issue, page numbers, DOI and the link to the definitive published version on Wiley Online Library) should be maintained. Copyright notices and disclaimers must not be deleted.
- Any translations, for which a prior translation agreement with Wiley has not been agreed, must prominently display the statement: "This is an unofficial translation of an article that appeared in a Wiley publication. The publisher has not endorsed this translation."

Use by commercial "for-profit" organisations

Use of Wiley Open Access articles for commercial, promotional, or marketing purposes requires further explicit permission from Wiley and will be subject to a fee. Commercial purposes include:

- Copying or downloading of articles, or linking to such articles for further redistribution, sale or licensing;
- Copying, downloading or posting by a site or service that incorporates advertising with such content;
- The inclusion or incorporation of article content in other works or services (other than normal quotations with an appropriate citation) that is then available for sale or licensing, for a fee (for example, a compilation produced for marketing purposes, inclusion in a sales pack)
- Use of article content (other than normal quotations with appropriate citation) by for-profit organisations for promotional purposes
- Linking to article content in e-mails redistributed for promotional, marketing or educational purposes;
- Use for the purposes of monetary reward by means of sale, resale, licence, loan, transfer or other form of commercial exploitation such as marketing products
- Print reprints of Wiley Open Access articles can be purchased from: corporatesales@wiley.com

Other Terms and Conditions:

BY CLICKING ON THE "I AGREE..." BOX, YOU ACKNOWLEDGE THAT YOU HAVE READ AND FULLY UNDERSTAND EACH OF THE SECTIONS OF AND PROVISIONS SET FORTH IN THIS AGREEMENT AND THAT YOU ARE IN AGREEMENT WITH AND ARE WILLING TO ACCEPT ALL OF YOUR OBLIGATIONS AS SET FORTH IN THIS AGREEMENT.

v1.7

If you would like to pay for this license now, please remit this license along with your payment made payable to "COPYRIGHT CLEARANCE CENTER" otherwise you will be invoiced within 48 hours of the license date. Payment should be in the form of a check or money order referencing your account number and this invoice number RLNK500947942. Once you receive your invoice for this order, you may pay your invoice by credit card. Please follow instructions provided at that time.

Make Payment To:
Copyright Clearance Center
Dept 001
P.O. Box 843006
Boston, MA 02284-3006

For suggestions or comments regarding this order, contact RightsLink Customer Support: customercare@copyright.com or +1-877-622-5543 (toll free in the US) or +1-978-646-2777.

Gratis licenses (referencing $0 in the Total field) are free. Please retain this printable license for your reference. No payment is required.

References

[1] Wind induced sediment resuspension: a lake-wide model. *Ecological Modelling*, 99(2-3):217 – 228, 1997.

[2] Payam Aghsaee, Leon Boegman, Peter J. Diamessis, and Kevin G. Lamb. Boundary-layer-separation-driven vortex shedding beneath internal solitary waves of depression. *Journal of Fluid Mechanics*, 690:321–344, 2012.

[3] Muhammad Alam and Neil D. Sandham. Direct numerical simulation of short laminar separation bubbles with turbulent reattachment. *Journal of Fluid Mechanics*, 410:1–28, 4 2000.

[4] Ann S. Almgren, John B. Bell, and William Y. Crutchfield. Approximate projection methods: Part I. inviscid analysis. *SIAM J. Sci. Comput.*, 22(4):1139–1159, 2000.

[5] Rutherford Aris. *Vectors, Tensors, and the Basic Equations of Fluid Mechanics*. Dover Books on Mathematics Series. Dover Publications, Incorporated, 1989.

[6] Neil J. Balmforth, Yoel Forterre, and Olivier Pouliquen. The viscoplastic stokes layer. *J. Non-Newtonian Fluid Mech.*, 158(1-3):46 – 53, 2009.

[7] Neil. J. Balmforth and John J. Liu. Roll waves in mud. *J. Fluid Mech.*, 519:33–54, 10 2004.

[8] George Keith Batchelor. *An Introduction to Fluid Dynamics*. Cambridge Mathematical Library. Cambridge University Press, 2000.

[9] Gordon S. Beavers and Daniel D. Joseph. Boundary conditions at a naturally permeable wall. *Journal of Fluid Mechanics*, 30(1):197–207, 1967.

[10] T. H. Bell. Topographically generated internal waves in the open ocean. *Journal of Geophysical Research*, 80(3).

[11] Nastja Bethke and Stuart B. Dalziel. Resuspension onset and crater erosion by a vortex ring interacting with a particle layer. *Phys. Fluids*, 24:063301, 2012.

[12] Francois Blanchette, Martin Strauss, Eckart Meiburg, Benjamin Kneller, and Michael E. Glinsky. High-resolution numerical simulations of resuspending gravity currents: Conditions for self-sustainment. *J. Geophys. Res.*, 110(C12):C12022, 2005.

[13] Jurg Bloesch. Mechanisms, measurement and importance of sediment resuspension in lakes. *Mar. Freshwater Res.*, 46(1):295–304, 1995.

[14] Leon Boegman, Jorg Imberger, Greg N. Ivey, and Jason P. Antenucci. High-frequency internal waves in large stratified lakes. *Limnology Oceanography*, 48(2):895–919, 2003.

[15] Derek Bogucki, Tommy Dickey, and Larry G. Redekopp. Sediment Resuspension and Mixing by Resonantly Generated Internal Solitary Waves. *Journal of Physical Oceanography*, 27:1181–1196, 1997.

[16] Derek J. Bogucki, Larry. G. Redekopp, and Jack Barth. Internal solitary waves in the Coastal Mixing and Optics 1996 experiment: Multimodal structure and resuspension. *Journal of Geophysical Research (Oceans)*, 110:C02024, February 2005.

[17] G. Bohme, L. Rubart, and M. Stenger. Vortex breakdown in shear-thinning liquids: experiment and numerical simulation. *J. Non-Newtonian Fluid Mech.*, 45(1):1 – 20, 1992.

[18] Henry J. Bokuniewicz. Analytical descriptions of subaqueous groundwater seepage. *Estuaries*, 15(4):458–464, 1992.

[19] John P. Boyd. *Chebyshev and Fourier Spectral Methods.* Dover Publications, 2nd edition, 2001.

[20] M. Bayani Cardenas and Houshuo Jiang. Wave-driven porewater and solute circulation through rippled elastic sediment under highly transient forcing. *Limnology and Oceanography: Fluids and Environment*, 2011.

[21] M. Bayani. Cardenas and John L. Wilson. Effects of current-bed form induced fluid flow on the thermal regime of sediments. *Water Resources Research*, 43:W08431, August 2007.

[22] Magda Carr. Penetrative convection in a superposed porous-medium fluid layer via internal heating. *Journal of Fluid Mechanics*, 509:305–329, 2004.

[23] Magda Carr, Peter A. Davies, and Pruthvi Shivaram. Experimental evidence of internal solitary wave-induced global instability in shallow water benthic boundary layers. *Physics of Fluids*, 20(6):066603, June 2008.

[24] Magda Carr, Peter A. Davies, and Pruthvi Shivaram. Experimental evidence of internal solitary wave-induced global instability in shallow water benthic boundary layers. *Physics of Fluids*, 20(6):066603, 2008.

[25] Pierre J. Carreau. *Rheological Equations From Molecular Network Theories*. PhD thesis, University of Wisconsin, 1968.

[26] Herman J. H. Clercx and Gert Jan F. van Heijst. Dissipation of kinetic energy in two-dimensional bounded flows. *Phys. Rev. E*, 65:066305, Jun 2002.

[27] Herman J.H. Clercx and Charles-Henri Bruneau. The normal and oblique collision of a dipole with a no-slip boundary. *Computers & Fluids*, 35(3):245 – 279, 2006.

[28] Philippe Coussot and Jean Michel Piau. On the behavior of fine mud suspensions. *Rheol. Acta*, 33:175–184, 1994.

[29] Andrew D. Cutler and Peter Bradshaw. Strong vortex/boundary layer interactions. *Exp. Fluids*, 14:393–401, 1993.

[30] Jose C. B. da Silva and Karl R. Helfrich. Synthetic aperture radar observations of resonantly generated internal solitary waves at race point channel (cape cod). *Journal of Geophysical Research*, 113:C11016, 2008.

[31] Lokenath Debnath. *Nonlinear water waves*. Academic Press, Boston, 1994.

[32] Peter J. Diamessis and Larry G. Redekopp. Numerical Investigation of Solitary Internal Wave-Induced Global Instability in Shallow Water Benthic Boundary Layers. *Journal of Physical Oceanography*, 36:784, 2006.

[33] Micheal Dunphy, Christopher Subich, and Marek Stastna. Spectral methods for internal waves: indistinguishable density profiles and double-humped solitary waves. *Nonlinear Processes in Geophysics*, 18(3):351–358, 2011.

[34] Alexander H. Elliot and Norman H. Brooks. Transfer of nonsorbing solutes to a streambed with bed forms: Theory. *Water Resources Research*, 33(1):123, 1997.

[35] Marcel. P. Escudier, I. W. Gouldson, and D. M. Jones. Taylor vortices in newtonian and shear-thinning liquids. *Proc. R. Soc. London*, 449(1935):pp. 155–176, 1995.

[36] R.Douglas Evans. Empirical evidence of the importance of sediment resuspension in lakes. *Hydrobiologia*, 284(1):5–12, 1994.

[37] Goril Flaten and Ole B. Rygg. Dispersive shallow water waves over a porous sea bed. *Coastal Engineering*, 15(4):347 – 369, 1991.

[38] Arnold Fredrickson and R. Byron Bird. Non-newtonian flow in annuli. *Ind. Eng. Chem.*, 50(3):347–352, 1958.

[39] Yuan-Cheng Fung. *A first course in continuum mechanics*. Prentice-Hall, 1969.

[40] Marcelo Garcia and Gary Parker. Experiments on the entrainment of sediment into suspension by a dense bottom current. *Journal of Geophysical Research: Oceans*, 98(C3):4793–4807, 1993.

[41] Christopher Garrett and Walter Munk. Internal waves in the ocean. *Annual Review of Fluid Mechanics*, 11(1):339–369, 1979.

[42] David Genereux and Indranil Bandopadhyay. Numerical investigation of lake bed seepage patterns: effects of porous medium and lake properties. *Journal of Hydrology*, 241(3-4):286 – 303, 2001.

[43] Georgios C. Georgiou. The time-dependent, compressible poiseuille and extrudate-swell flows of a carreau fluid with slip at the wall. *J. Non-Newtonian Fluid Mech.*, 109(2):93 – 114, 2003.

[44] Stanley B. Grant, Michael J. Stewardson, and Ivan Marusic. Effective diffusivity and mass flux across the sediment-water interface in streams. *Water Resources Research*, 48(5):286 – 303, 2012.

[45] Richard Haberman. *Applied Partial Differential Equations: With Fourier Series and Boundary Value Problems*. Pearson Prentice Hall, Pearson Education, Incorporated, 2004.

[46] Carl P. Haggmark, Andrey A. Bakchinov, and P. Henrik Alfredsson. Experiments on a twodimensional laminar separation bubble. *Philosophical Transactions of the Royal Society of London. Series A: Mathematical, Physical and Engineering Sciences*, 358(1777):3193–3205, 2000.

[47] David A. Hammond and Larry G. Redekopp. Local and global instability properties of separation bubbles. *European Journal of Mechanics - B/Fluids*, 17(2):145 – 164, 1998.

[48] Savvas G. Hatzikiriakos and John M. Dealy. Wall slip of molten high density polyethylenes. ii. capillary rheometer studies. *J. Rheol.*, 36(4):703–741, 1992.

[49] Karl R. Helfrich and W. Kendall Melville. Long nonlinear internal waves. *Annual Review of Fluid Mechanics*, 38(1):395–425, 2006.

[50] Makoto Higashino, Jeffery J. Clark, and Heinz G. Stefan. Pore water flow due to near-bed turbulence and associated solute transfer in a stream or lake sediment bed. *Water Resources Research*, 45:W12414, December 2009.

[51] Makoto Higashino and Heinz Stefan. Model of turbulence penetration into a suspension layer on a sediment bed and effect on vertical solute transfer. *Environmental Fluid Mechanics*, 12(5):451–469, 2012. 10.1007/s10652-012-9241-8.

[52] P. M. Holligan, R. D. Pingree, and G. T. Mardell. Oceanic solitons, nutrient pulses and phytoplankton growth. *Nature*, 314, 1985.

[53] Phil Hosegood and Hans van Haren. Near-bed solibores over the continental slope in the Faeroe-Shetland Channel. *Deep Sea Research Part II: Topical Studies in Oceanography*, 51:2943–2971, December 2004.

[54] Ping-Cheng Hsieh, Hsi heng Dai, and Liang hsiung Huang. Laminar water wave and current passing over porous bed. *Journal of Engineering Mechanics*, 129(6):655–664, 2003.

[55] Ching-Jer Huang, Chih-Hsin Chen, and Hsing-Han Chang. Propagation of water waves over permeable rippled beds. *Ocean Engineering*, 38(4):579 – 591, 2011.

[56] Lingyan Huang and Qin Chen. Spectral collocation model for solitary wave attenuation and mass transport over viscous mud. *J. Eng. Mech.*, 135(8):881–891, 2009.

[57] Lingyan Huang, Chui-On Ng, and Allen Chwang. A Fourier-Chebyshev collocation method for the mass transport in a layer of power-law fluid mud. *Comput. Methods Appl. Mech. Eng.*, 195:1136–1153, February 2006.

[58] Markus Huettel, Wiebke. Ziebis, and Stefan Forster. Flow-induced uptake of particulate matter in permeable sediments. *Limnology and Oceanography*, 41(2):pp. 309–322, 1996.

[59] Kolumban Hutter. *Nonlinear Internal Waves in Lakes.* Advances in Geophysical and Environmental Mechanics and Mathematics. Springer, 2011.

[60] Duncan James Jeffrey and Andreas Acrivos. The rheological properties of suspensions of rigid particles. *AIChE J.*, 22(3):417–432, 1976.

[61] Thomas C. Johnson. Sedimentation in large lakes. *Annual Review of Earth and Planetary Sciences*, 12:pp. 179–204, 1984.

[62] George E. Karniadakis, Moshe Israeli, and Steven A. Orszag. High-order splitting methods for the incompressible navier-stokes equations. *J. Comp. Phys.*, 97:414–443, 1991.

[63] Pijush Kundu. *Fluid mechanics.* Academic Press, San Diego, 1990.

[64] Kevin G. Lamb. Numerical experiments of internal wave generation by strong tidal flow across a finite amplitude bank edge. *Journal of Geophysical Research: Oceans*, 99(C1).

[65] Kevin G. Lamb. A numerical investigation of solitary internal waves with trapped cores formed via shoaling. *Journal of Fluid Mechanics*, 451:109–144, 2002.

[66] Kevin G. Lamb and David Farmer. Instabilities in an internal solitary-like wave on the oregon shelf. *Journal of Physical Oceanography*, 41:67–87, 2011.

[67] Kevin G. Lamb and Bangjun Wan. Conjugate flows and flat solitary waves for a continuously stratified fluid. *Physics of Fluids*, 10(8):2061–2079, 1998.

[68] Kevin G. Lamb and Liren Yan. The evolution of internal wave undular bores: Comparisons of a fully nonlinear numerical model with weakly nonlinear theory. *Journal of Physical Oceanography*, 26:2712–2734, 1996.

[69] Rene Laprise and W. Richard Peltier. On the structural characteristics of steady finite-amplitude mountain waves over bell-shaped topography. *Journal of Atmospheric Sciences*, 46:586–595, 1989.

[70] Michael Le Bars and M. Grae Worster. Solidification of a binary alloy: finite-element, single-domain simulation and new benchmark solutions. *J. Comput. Phys.*, 216:247–263, July 2006.

[71] Alan Luton, Saad Ragab, and Demetri Telionis. Interaction of spanwise vortices with a boundary layer. *Phys. Fluids*, 7(11):2757–2765, 1995.

[72] Sally MacIntyre, James O. Sickman, Sarah A. Goldthwait, and George W. Kling. Physical pathways of nutrient supply in a small, ultraoligotrophic arctic lake during summer stratification. *Limnology Oceanography*, 51(2):1107–1124, 2006.

[73] James C. McWilliams. *Fundamentals of Geophysical Fluid Dynamics*. Cambridge University Press, 2006.

[74] Ashish J. Mehta. Understanding fluid mud in a dynamic environment. *Geo-Mar. Lett.*, 11:113–118, 1991.

[75] Chiang C. Mei and Ko-Fei Liu. A bingham-plastic model for a muddy seabed under long waves. *J. Geophys. Res.*, 92:14581, 1987.

[76] Filip J. R. Meysman, Oleksiy S. Galaktionov, Perran L. M. Cook, FJJG Janssen, Markus Huettel, and Jack J. Middelburg. Quantifying biologically and physically induced flow and tracer dynamics in permeable sediments. *Biogeosciences*, 4(4):627–646, 2007.

[77] Robert J. Munro. The interaction of a vortex ring with a sloped sediment layer: Critical criteria for incipient grain motion. *Phys. Fluids*, 24:026604, 2012.

[78] Chui-On Ng and Chiang C. Mei. Roll waves on a shallow layer of mud modelled as a power-law fluid. *J. Fluid Mech.*, 263:151–183, 1994.

[79] Donald A. Nield and Adrian Bejan. *Convection in Porous Media*, volume XXIV. Springer, third edition, 2006.

[80] Daniela A. Oliveira Ommen, Jacob Kidmose, Sachin Karan, Mogens R. Flindt, Peter Engesgaard, Bertel Nilsson, and Frede Andersen. Importance of groundwater and macrophytes for the nutrient balance at oligotrophic lake hampen, denmark. *Ecohydrology*, pages 286–296, 2011.

[81] Celalettin E. Ozdemir, Tian-Jian Hsu, and Sivaramakrishnan Balachandar. A numerical investigation of lutocline dynamics and saturation of fine sediment in the oscillatory boundary layer. *J. Geophys. Res.*, 116(C9):C09012, 2011.

[82] Alan R. Packwood and D. Howell Peregrine. The propagation of solitary waves and bores over a porous bed. *Coastal Engineering*, 3:221 – 242, 1980.

[83] Martina Preusse, Heinrich Freistuhler, and Frank Peeters. Seasonal variation of solitary wave properties in lake constance. *Journal of Geophysical Research (Oceans)*, 117:C04026, 2012.

[84] Rupert J. Riedl, Natalia Huang, and Rudolf Machan. The subtidal pump: a mechanism of interstitial water exchange by wave action. *Marine Biology*, 13:210–221, 1972. 10.1007/BF00391379.

[85] Carlos Rocha. Density-driven convection during flooding of warm, permeable intertidal sediments: the ecological importance of the convective turnover pump. *Journal of Sea Research*, 43(1):1 – 14, 2000.

[86] Christian Ruyer-Quil, Symphony Chakraborty, and Bhabani S. Dandapat. Wavy regime of a power-law film flow. *J. Fluid Mech.*, 692:220–256, 2012.

[87] Mashfiqus Salehin, Aaron I. Packman, and Matthew Paradis. Hyporheic exchange with heterogeneous streambeds: Laboratory experiments and modeling. *Water Resources Reseach*, 40:W11504, 2004.

[88] H. Sandstrom and J. A. Elliott. Internal tide and solitons on the scotian shelf: A nutrient pump at work. *Journal of Geophysical Research: Oceans*, 89(C4):6415–6426, 1984.

[89] Audrey Hucks Sawyer and M. Bayani Cardenas. Hyporheic flow and residence time distributions in heterogeneous cross-bedded sediment. *Water Resources Reseach*, 45:W08406, 2009.

[90] Carlo Scalo, Ugo Piomelli, and Leon Boegman. High-schmidt-number mass transport mechanisms from a turbulent flow to absorbing sediments. *Physics of Fluids*, 24(8):085103, 2012.

[91] Carlo Scalo, Ugo Piomelli, and Leon Boegman. Large-eddy simulation of oxygen transfer to organic sediment beds. *Journal of Geophysical Research: Oceans*, 117(C6), 2012.

[92] Hermann Schlichting and Klaus Gersten. *Boundary Layer Theory.* McGraw-Hill Book Company, USA, 1979.

[93] Kwock Tai Shum. The effects of wave-induced pore water circulation on the transport of reactive solutes below a rippled sediment bed. *Journal of Geophysical Research*, 98(C6):10,289–10,301, 1993.

[94] Nancy Soontiens, Christopher Subich, and Marek Stastna. Numerical simulation of supercritical trapped internal waves over topography. *Physics of Fluids*, 22(11):116605, 2010.

[95] Marek Stastna and Kevin G. Lamb. Large fully nonlinear internal solitary waves: The effect of background current. *Physics of Fluids*, 14(9):2987–2999, 2002.

[96] Marek Stastna and Kevin G. Lamb. Vortex shedding and sediment resuspension associated with the interaction of an internal solitary wave and the bottom boundary layer. *Geophysical Research Letters*, 29:1512, 2002.

[97] Marek Stastna and Kevin G. Lamb. Sediment resuspension mechanisms associated with internal waves in coastal waters. *Journal of Geophysical Research: Oceans*, 113(C10):C10016, 2008.

[98] Marek Stastna and Kevin G. Lamb. Sediment resuspension mechanisms associated with internal waves in coastal waters. *Journal of Geophysical Research (Oceans)*, 113:C10016, October 2008.

[99] Marek Stastna and W. Richard Peltier. On the resonant generation of large-amplitude internal solitary and solitary-like waves. *Journal of Fluid Mechanics*, 543:267–292, 2005.

[100] Terri L. Stewart and H. Scott Fogler. Pore-scale investigation of biomass plug development and propagation in porous media. *Biotechnology and Bioengineering*, 77:577 – 588, 2002.

[101] Christopher Subich. *Simulation of the Navier-Stokes Equations in Three Dimensions with a Spectral Collocation Method*. PhD thesis, University of Waterloo, 2011.

[102] Mark C. Thompson and Kerry Hourigan. The sensitivity of steady vortex breakdown bubbles in conned cylinder ows to rotating lid misalignment. *J. Fluid Mech.*, 496:129–138, 2003.

[103] Lloyd N. Trefethen. *Spectral methods in MatLab*. Society for Industrial and Applied Mathematics, Philadelphia, PA, USA, 2000.

[104] A. Turkington, B. Eydeland and S. Wang. A computational method for solitary internal waves in a continuously stratified fluid. *Stud. Appl. Math.*, 85:93–127, 1991.

[105] Jamal Uddin, Jeremy O. Marston, and Sigurdur T. Thoroddsen. Squeeze flow of a carreau fluid during sphere impact. *Phys. Fluids*, 24:073104, 2012.

[106] Joseph E. Webb and Jessica Theodor. Irrigation of submerged marine sands through wave action. *Letters to Nature*, 220:682–683, 1968.

[107] Anders Wörman, Aaron I. Packman, Lars Marklund, Judson W. Harved, and Susa H. Stone. Exact three-dimensional spectral solution to surface-groundwater interactions with arbitrary surface topography. *Geophysical Research Letters*, 33:L07402, 2006.

[108] Vitaly A. Zlotnik, M. Bayani Cardenas, and Daniel Toundykov. Effects of multiscale anisotropy on basin and hyporheic groundwater flow. *Ground Water*, 49(4):576–583, 2011.